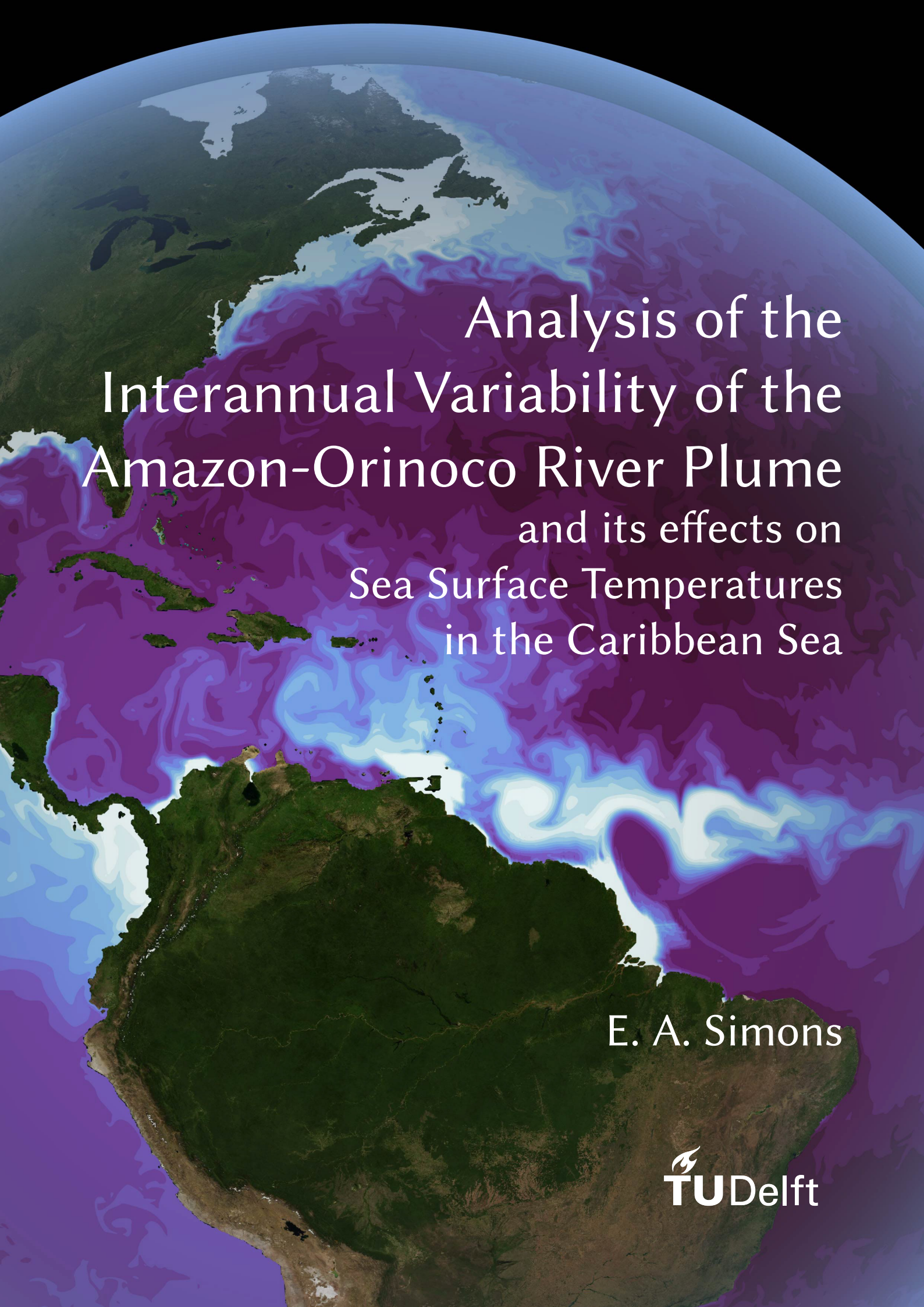

Analysis of the Interannual Variability of the Amazon-Orinoco River Plume and its effects on Sea Surface Temperatures in the Caribbean Sea

E. A. Simons

TU Delft

Interannual Variability of the Amazon-Orinoco River Plume

and its Effects on Sea Surface Temperature in the Caribbean Sea

by

E. A. (Ascha) Simons

in partial fulfilment of the requirements for the degree of

Master of Science

in

Hydraulic Engineering
Faculty of Civil Engineering and Geosciences
Department of Hydraulic Engineering
Section of Environmental Fluid Mechanics

at the Delft University of Technology,

to be defended publicly on Friday October 30, 2020 at 13:00.

Student number:	4248457	
Thesis committee:	Prof. dr. J. D. Pietrzak,	Delft University of Technology
	Prof. dr. P. M. J. Herman,	Delft University of Technology
	Dr. R. E. M. Riva,	Delft University of Technology
	ir. C. van der Boog,	Delft University of Technology

An electronic version of this thesis is available at http://repository.tudelft.nl/.

(Cover image made using E.U. Copernicus Marine Service Information)

TU Delft

Preface

Before you lies the master thesis that concludes my studies at Delft University of Technology. When I first set foot in the Civil Engineering building eight years ago, I would never have thought that I would write my graduation thesis from home, in the turbulent year of 2020. I had also not expected that my report about coral, marking the end to my primary education in 2006, would be so relevant to the subject of my MSc thesis fourteen years later, yet here we are.

I would like to thank the members of my graduation committee for their guidance and constructive criticism during this project. I want to thank ir. Carine van der Boog, for the extensive feedback, the helpful conversations and support, and for putting things in perspective. I want to thank prof. dr. Peter Herman and dr. Riccardo Riva for their valuable feedback and their views on the project. Lastly, I want to thank prof. dr. Julie Pietrzak for chairing my graduation committee, the inspiring conversation on my research topic and the unwavering support during this project.

Lastly, my expressions of gratitude go out to my family and friends for encouraging me and cheering me on, and for the necessary distractions. Especially Rosa, you boosted my confidence by a lot in the strenuous final period. Finally, I want to thank you, Daan, for always being there for me during this roller-coaster ride, for your patience and for guarding my sanity.

I hope you enjoy your reading.

E.A. Simons
Leiden, October 2020

Contents

Abstract

The Amazon-Orinoco river plume is a buoyant freshwater lens of 1.2×10^6 km^2, which has been traced over 2000 km from the Amazon river mouth into the Caribbean Sea and along the Lesser Antilles. The river plume is warmer than the surrounding open-ocean waters, with temperature differences up to 1.5 ˚C caused by a stratification-induced barrier layer inhibiting vertical mixing and coloured matter increasing solar energy absorption. Due to its magnitude, the river plume affects the hydrodynamics and the oceanic conditions in the Western Tropical North Atlantic (WTNA) substantially, but its variations on interannual time scales and the corresponding relation to local sea-surface temperature (SST) are not well understood.

The Caribbean Sea is a region of high ecological value as it is home to extensive coral reefs, which are especially sensitive to persistent high SST. Therefore, this study investigates the interannual variability of the Amazon-Orinoco river plume and its relationship to SSTs in the Caribbean Sea and the WTNA. It is hypothesised that fresh anomalies of the river plume salinity pattern are indicative of a more extensive transportation of the heat contained in the river plume. As a result, it is expected that interannual variations of dominant river plume pathways affect the magnitude and location of anomalous SSTs.

To test this hypothesis, model reanalysis fields of oceanic conditions from 1993 to 2017 are used to conduct statistical analysis. In this context, the river plume variability is determined using specific regions of freshwater influence established using Empirical Orthogonal Function (EOF) analysis of anomalous sea-surface salinity (SSS).

Cross-correlations analysis relating these EOF modes of with atmospheric processes show that the interannual variability of the river plume is dominated by wind-induced advective transport and -mixing. Strong winds along the Brazilian shelf are related locally increased SSS, while a weak southward component makes for extensive spreading of the low-salinity plume waters. Additionally, we show that high river discharge affects SSS east of the Lesser Antilles after a lag of three months.

Through its modulation of these atmospheric processes, there is a strong indication that the El Niño-Southern Oscillation affects SSS variability in the main along-shelf northwest plume pathway, with low SSS 1–9 months after a La Niña event. Decreased SSS are found in phases 2 and 3 of the Madden-Julian Oscillation, while increased SSS was observed in phases 6 and 7. However, the evidence for this relation is weak and should be further investigated in further research.

The results show that, opposed to the hypothesis, a more extensive river plume is not associated with higher SSTs in the Caribbean Sea. However, strong correlations are found between river plume surface area and SSTs at a lag of 1 year. Based upon results of previous studies, we argue that the river plume has the ability to pre-heat the mixed layer in the WTNA leading to extreme temperatures in the following year. It is wise to conduct a Lagrangian parcel back-tracking experiment to verify this mechanism.

1

Introduction

In 2005, a massive bleaching event caused enormous damage to Caribbean corals, with losses of up to 51.5% in some regions (Wilkinson & Souter, 2008). As it had been the hottest year for the Northern Hemisphere on record (Kennedy, Dunn, McCarthy, Titchner & Morice, 2017), it seems unsurprising that the heat stress in the Caribbean was unprecedented and caused extensive coral bleaching and mortality. However, eight more years with similar or even higher annual temperatures have since followed, while not all of them have seen such destructive effects in the Caribbean region. For example, the year 2016 was the second hottest year on record and was declared the Third Global Coral Bleaching event on record by NOAA Coral Reef Watch (2019). However, the heat stress in the Caribbean was measured to be relatively mild. As a result, Caribbean corals were not affected as much as would be expected. While global temperatures are thus a partial predictor of heat stress in the Caribbean, there are more factors at play. One possible cause is the Amazon river plume. As the Amazon river plume is associated with high sea-surface temperatures (SSTs) in the Caribbean Sea (e.g. Hu, Montgomery, Schmitt & Muller-Karger, 2004), it is hypothesised that the river plume affects the occurrence of coral bleaching events.

With its annual average discharge of 210 000 m^3/s, the Amazon river discharges more freshwater than the subsequent seven largest rivers combined (calculated from Dai, 2017). It accounts for approximately 15 % of the estimated global river discharge on an annual basis (Baumgartner & Reichel, 1975). This discharged freshwater flows into the tropical Atlantic Ocean, where it mixes with saline waters and forms a buoyant freshwater lens called a river plume. Initially, the river plume flows northwestward over the Brazilian shelf, after which it splits into two general directions (see Fig. 1.1). Approximately 35 % of the plume water is carried in the direction of the African continent by the North Equatorial Counter Current (NECC), while the rest of the plume flows towards the Caribbean Sea (V. J. Coles et al., 2013).

At about 62°W, 1500 km from the mouth of the Amazon River, the northwest part of the plume is joined by the Orinoco river discharge. Although the Orinoco river is the third largest river in the world, its annual discharge is still only a fifth of the Amazon River discharge. Additionally, estimates made when distinguishing the combined plume by the influence of the individual rivers reveal that the horizontal area of the Amazon river plume is seven times larger than that of the Orinoco (Hu et al., 2004). Despite the fact that the Orinoco river influence is smaller, its effects cannot be ignored. Because of the distance travelled, the Amazon river plume has been subject to mixing and subsequent salinity increase by the time it reaches the Caribbean Sea, where it merges with the Orinoco river plume. Since the Orinoco river injects freshwater into the combined Amazon-Orinoco plume, it reduces the overall salinity. Afterwards, the resulting combined Amazon-Orinoco river plume flows into the Caribbean Sea and along the Caribbean Islands.

River waters have been traced over 2000 km from the river mouth, into the Caribbean Sea and along the Caribbean Islands (V. J. Coles et al., 2013; Hu et al., 2004). Therefore, the plume can affect hydrodynamic processes in the whole Western Tropical North Atlantic (WTNA) and the Caribbean Sea. The horizontal extent of the river plume is 1.2×10^6 km^2 (Hu et al., 2004),

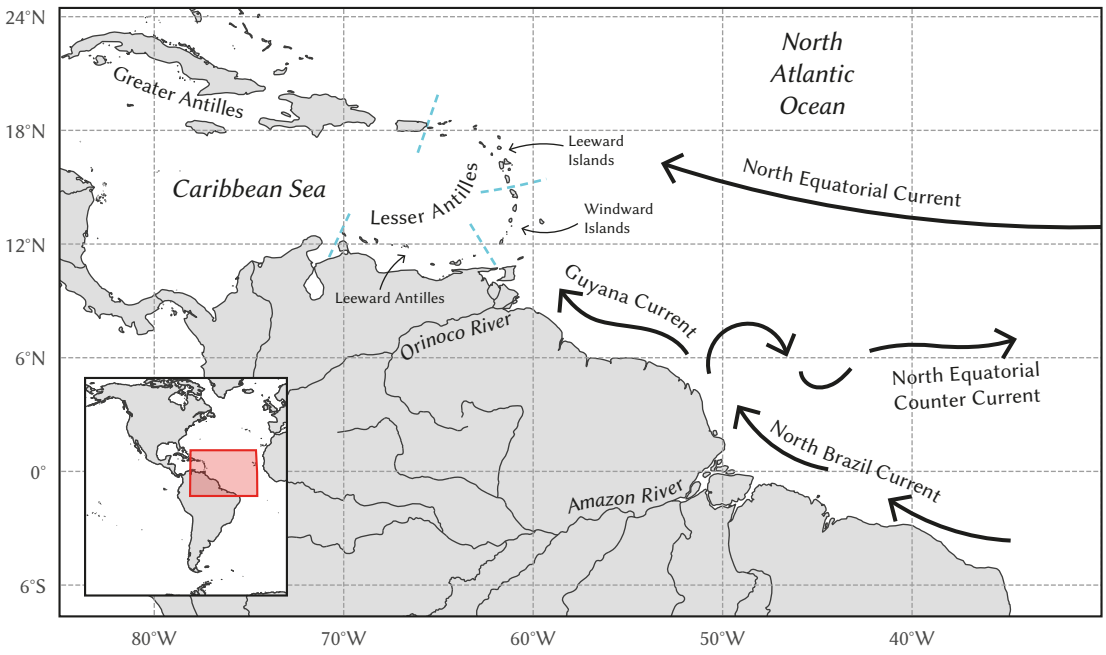

Figure 1.1: Overview of the area of interest, showing the Amazon and Orinoco Rivers, island ranges and dominant mean currents (adapted from V. J. Coles et al., 2013).

which is exceptionally large due to the magnitude of the Amazon discharge.

The river plume has distinctive characteristics that influence physical and ecological processes in the Caribbean Sea. Firstly, the plume acts as a transport mechanism for nutrients as well as organic matter (colored dissolved organic matter (CDOM) and dissolved organic matter (DOM)) originating from the Amazon and Orinoco rivers. As a result, the plume is associated with an increase of Sargassum weeds on Caribbean shores (Johns et al., 2020; Putman et al., 2018; Wang & Hu, 2017). Furthermore, since the riverine waters contain more CDOM than the open-ocean waters, they absorb more solar radiation which results in an increase of surface temperature (Fig. 1.2).

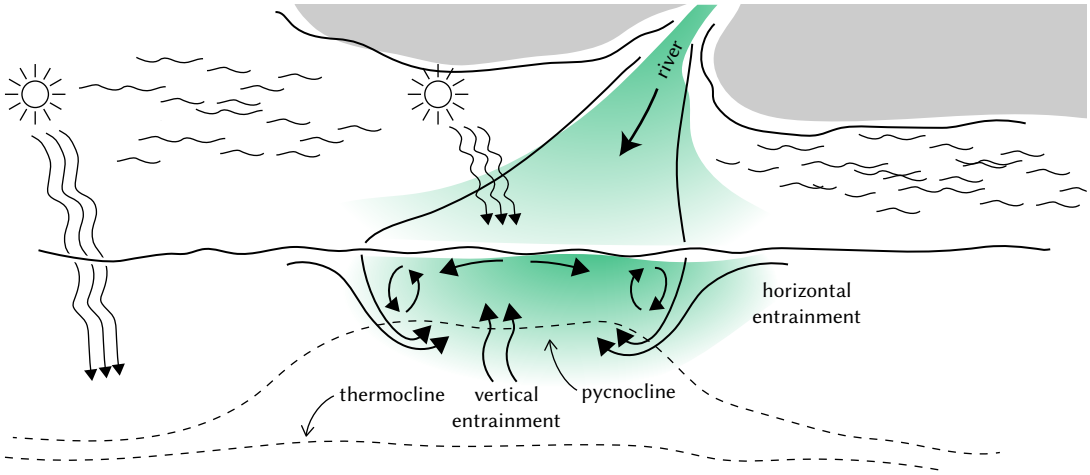

Figure 1.2: Schematic representation of a laterally expanding river plume (adapted from Wiseman Jr, Rabalais, Dagg & Whitledge, 1999). Green shading indicates increased concentration of CDOM.

Secondly, the relatively thin buoyant freshwater layer induces a shallow pycnocline, while the deep isothermal layer remains relatively constant (Fig. 1.2). This produces a barrier layer separating the shallow, warm waters from the deeper, cooler waters (Pailler, Bourlès & Gouriou,

1999). This barrier layer inhibits vertical mixing, leading to the trapping of solar radiation in the surface layer which further increases its temperature (Ffield, 2005; Foltz & McPhaden, 2009). As a result, SSTs in the river plume are found to be higher than those of surrounding open-ocean waters at the same latitude (Hu et al., 2004; Pailler et al., 1999). This is, in turn, associated with the promotion of tropical cyclogenesis and increased storm intensity (Balaguru et al., 2012).

The complex hydrodynamics in the region are influenced by a large number of processes, which cause large interannual variations of oceanic conditions. Because of the high SST associated with the river plume, which at times lead to coral bleaching and -mortality, it is important to better understand what causes this interannual variability.

1.1. Problem statement

The far-reaching effects of the river plume reassert the importance of its influence on the Eastern Caribbean Sea. To understand its variability on interannual time scales, it is important to shed light on the processes which cause the variability of the river plume. Prior research has been conducted on the variations of the river plume dynamics on a seasonal scale (V. J. Coles et al., 2013), allowing for a better understanding of the variations on these time scales. However, considerable variations arise when one examines the processes on a interannual scale. This interannual variability of the Amazon-Orinoco river plume and its effects on the SSTs in the area are not well understood. A better understanding of the interannual river plume variability may help explain why SSTs rise to destructive levels in some years.

1.2. Objectives and research questions

The aim of this study is to understand under what circumstances persistent high SSTs occur in the WTNA and the Caribbean Sea, by investigating their connection to interannual Amazon-Orinoco river plume variability.

To achieve this objective, the main research question is stated as follows:

> *What are the consequences of the interannual variability of the Amazon-Orinoco river plume on SSTs in the Caribbean Sea and the WTNA?*

To answer this research question, the following subquestions are formulated, together with their respective research objectives:

1. What are the defining characteristics of the Amazon-Orinoco river plume?
   (a) Establish what characteristics are used to define the Amazon-Orinoco river plume in existing literature;
   (b) Use model reanalysis results to determine a concrete definition of the river plume.
2. How does the Amazon-Orinoco river plume vary interannually?
   (a) Use the seasonal variability to determine the start and end of one plume cycle;
   (b) Gain insight into the behaviour of the river plume on interannual time scales;
   (c) Determine dominant modes of interannual variability of the river plume.
3. What processes affect the interannual variability of the Amazon-Orinoco river plume?
   (a) Determine what processes modulate the Amazon-Orinoco river plume based on existing literature;
   (b) Quantitatively assess the relation between these modulators and the previously defined dominant modes of interannual variability of the river plume.

1.3. Thesis outline

The overall structure of this thesis takes the form of 9 chapters (see Fig. 1.3), including this introductory chapter defining the problem statement, research objective and research questions.

Chapter 2 contains the theoretical framework, in which a description can be found of the Amazon-Orinoco river plume signature and -hydrodynamics can be found. Furthermore, causes of coral bleaching are discussed so that possible river plume-induced processes can be identified. A description of used data can be found in Chapter 3, including a validation of sea-surface salinity- and temperature data.

Hereafter, four chapters are found in which methods, results and subconclusions are presented. These chapters relate to the three research subquestions and the main research question, respectively. First of all, the sea-surface salinitys (SSSs) threshold that will be used to identify the river plume is validated in Chapter 4. Hereafter, the variability of the river plume is investigated in Chapter 5. In Chapter 6, the processes affecting the river plume are examined. Lastly, the relation of the interannual variability of the river plume to sea surface temperatures is assessed in Chapter 7.

In Chapters 8 and 9, the discussion, conclusions and recommendations can be found.

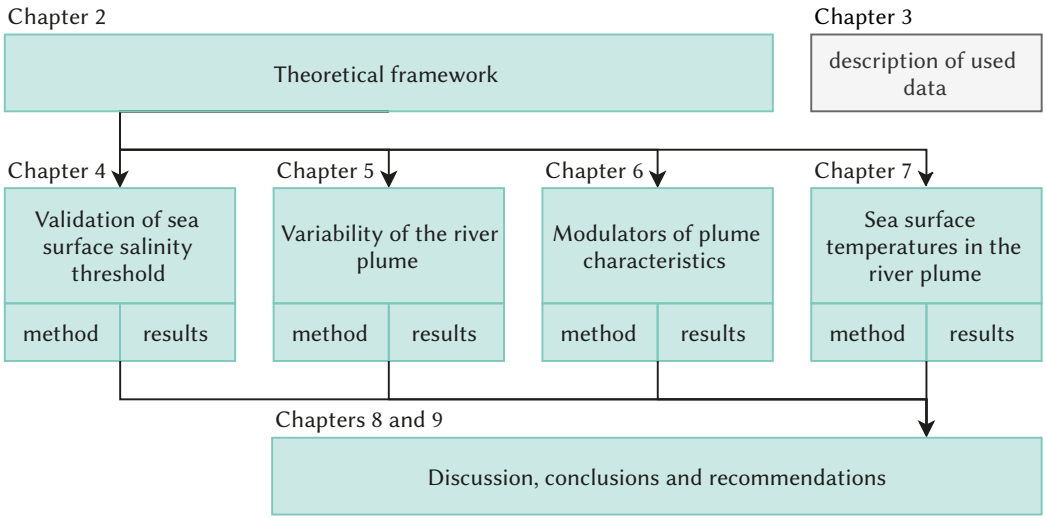

Figure 1.3: Outline of thesis

2

Theoretical framework

This chapter presents the theoretical framework of this thesis. The development and dynamics of the river plume are explained, after which an account is given on the processes affecting its variability. The last section discusses causes of coral bleaching in the Caribbean, so that possible river plume-induced processes can be identified.

2.1. The Amazon-Orinoco river plume

In this section, a description of the generation and dynamics of the Amazon and Orinoco plume is given, together with an analysis of how the plume is defined in prior research.

2.1.1. The Amazon and Orinoco Rivers

The annual discharge of the Amazon River is the highest in the world, with 15 % to 20 % of the global freshwater discharge released into the Atlantic Ocean (Baumgartner & Reichel, 1975; V. J. Coles et al., 2013). The annual discharge of 210 000 m^3/s (calculated from Dai, 2017) has a strong seasonal variation with a minimum discharge of 105 000 m^3/s in October-November and a maximum discharge of approximately 235 000 m^3/s in May-June (Fig. 2.2). This annual freshwater discharge is as much as the next seven largest rivers in the world combined (calculated from Dai, 2017).

The third largest river in the world in terms of annual discharge is the Orinoco River, with its river mouth located only 1500 km northwest of the Amazon River mouth (see Fig. 2.1). The maximum discharge follows that of the Amazon River by about three months, as can be seen in Fig. 2.2. Even though it is the third largest river in the world, the seasonal maximum discharge of the Orinoco river is still smaller than the seasonal minimum of the Amazon River discharge. Therefore, interannual discharge variations are much smaller than those of the Amazon river as well.

As the distinction between the Amazon and Orinoco river plumes is outside the scope of this thesis, the combined river plume will be referred to as 'the river plume'.

2.1.2. Observed spreading of the river plume

Upon reaching the Atlantic Ocean, the fresh Amazon river water enhances surface stratification and forms a river plume. It is first observed three to four months after the wet season in northeastern South America, which takes place from August to November (Chérubin & Richardson, 2007; Hu et al., 2004). Initially, the plume travels northwestward along the South-American continent by the North Brazil Current (NBC) in early spring (V. J. Coles et al., 2013; Ffield, 2005), until it reaches 51°W and spreads in northward direction. From there, part of the plume deflects to the east with the North Equatorial Counter Current (NECC) (Lentz, 1995; Muller-Karger, McClain & Richardson, 1988). The remainder of the plume flows to the northwest with the Guyana current and NBC rings (V. J. Coles et al., 2013).

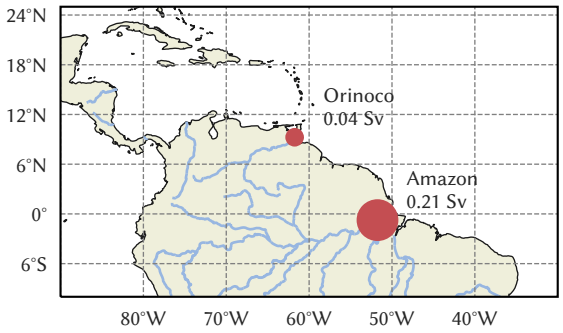

Figure 2.1: Locations of the Amazon and Orinoco river mouths. The size of the marker represents the average annual discharge, as given by Dai (2017). 1 Sv = 10^6 m^3/s.

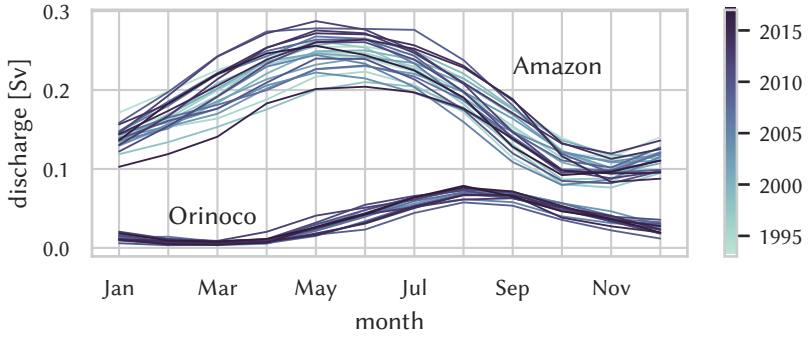

Figure 2.2: Monthly discharges of the Amazon (1993–2018, from Dai, 2017) and Orinoco (2003–2018, from SO-HYBAM, 2019) rivers from 1993–2018. 1 Sv = 10^6 m^3/s.

The northwest part of the river plume is joined by the Orinoco River plume and has been traced northwestward along the Windward- and Leeward Islands and into the Caribbean sea (V. J. Coles et al., 2013; Hu et al., 2004). Although the maximum flow of river water into the Caribbean Sea occurs in summer, older and saltier plume water inflow occurs in winter as well (V. J. Coles et al., 2013).

Remote sensing estimates have revealed a mean plume translation speed of 0.35 m/s (Hu et al., 2004). This means that the river plume takes about 2.5 months to travel the 2000 km from the Amazon river mouth to the Caribbean Sea. This is in line with V. J. Coles et al. (2013), who define a direct and an indirect northwest pathway with time scales of 2–3 months and 5–6 months, respectively.

2.1.3. River plume signature

In this section, the salinity-, buoyancy- and temperature signature of the river plume are discussed.

Salinity

To distinguish the river plume from surrounding waters, a salinity threshold is used with values varying from 34 psu to 35.5 psu throughout literature (V. J. Coles et al., 2013; Ffield, 2007; Lentz & Limeburner, 1995; Molleri, Novo & Kampel, 2010; Zeng et al., 2008). The typical open-ocean salinity in the region is 36.0 psu, from which Ffield (2007) concludes that the anomalous plume salinity signature which is dynamically significant is 35.4 psu.

The thickness of the plume varies between 10 m to 60 m, averaging 33 m during the summer, when identified using a maximum salinity threshold of 35.8 psu at depth and 35.4 psu at the sea

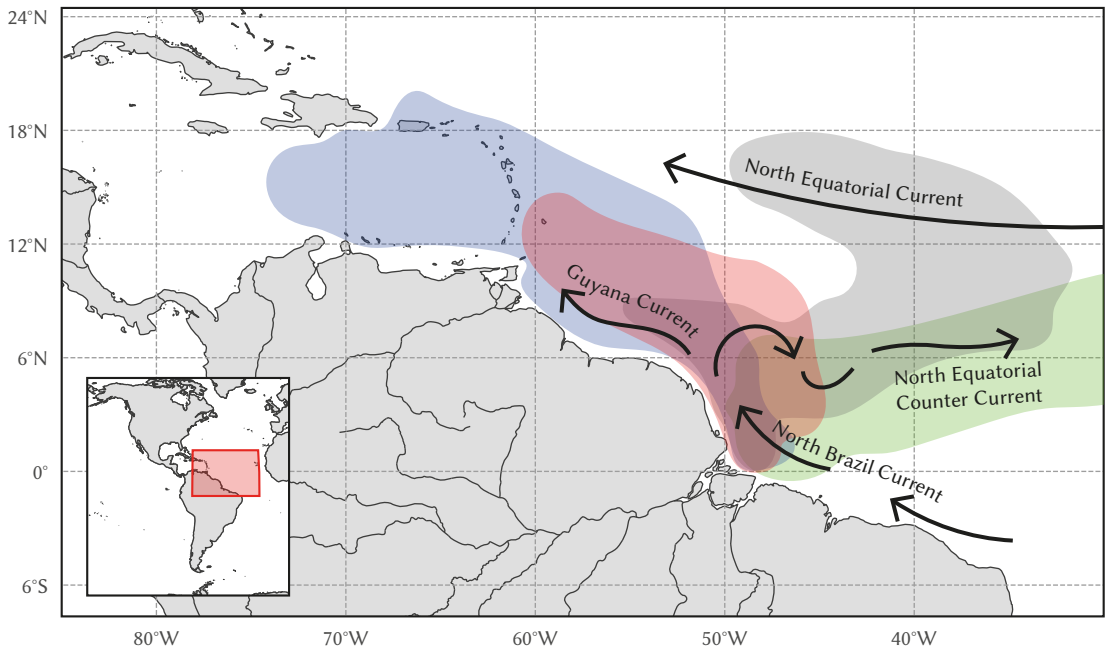

Figure 2.3: Dominant mean currents and main plume transport pathways as determined through float trajectory analysis: direct (blue) and indirect (red) northwest pathways and two eastward pathways (green and gray) (adapted from V. J. Coles et al., 2013).

surface (Ffield, 2007). The maximum plume extent is from 1 June to 30 November, coinciding with the hurricane season.

Buoyancy and barrier layer

The thin river plume flows into the Atlantic ocean into a thicker isothermal surface layer. The salinity difference introduces a buoyant layer, separated from the deeper, more saline water by a pyncocline. The salinity-induced pycnocline in the Western Tropical North Atlantic (WTNA) is found in the 3–30m depth range (V. J. Coles et al., 2013).

As a result of increased stratification stability caused by the plume's buoyancy pool, the plume is less affected by deep-reaching wind mixing and stays a distinguishable surface layer. This increased stability is of special importance in decreasing vertical mixing in the event of strong Tropical Cyclones (TCs) (Balaguru et al., 2012).

Since the isothermal layer is only mildly affected by the riverine inflow, the locally enhanced surface stratification leads to a relatively large distance between the thermocline and the pycnocline. This induces a barrier layer (Godfrey & Lindstrom, 1989; Lukas & Lindstrom, 1991). As its name suggests, this barrier layer inhibits mixing of the buoyant surface layer with the deep, cool waters.

Temperature

The low-salinity plume waters are associated with elevated sea-surface temperature (SST), with temperatures differing from open-ocean waters by up to 1.5 °C to 2 °C (Hu et al., 2004; Pailler et al., 1999).

This temperature difference results from the colored dissolved organic matter (CDOM)-richness of the riverine outflow, causing the fresh water to absorb more light and heat up more than higher-salinity waters at the same latitude (Hu et al., 2004). Additionally, the buoyant fresh water layer is isolated from the cool deep water through the barrier layer described previously. This barrier layer influences the temperature of the river plume in two ways. Firstly, it enhances the trapping of solar radiation in the surface layer (Ffield, 2005; Foltz & McPhaden, 2009). Secondly, the barrier layer has been argued to inhibit tropical cyclone-induced mixing

(Semyon A Grodsky et al., 2012). However, Hernandez, Jouanno and Durand (2016) show that only 10 % of the observed cooling inhibition can be explained by barrier layers and salinity stratification attributed to the river plume.

Although this SST difference is commonly attributed to the river plume, there is a correlation between SST variations and the location of the Intertropical Convergence Zone (ITCZ). Therefore, the high SSTs associated with low salinities could also be caused by decreased evaporation (Pailler et al., 1999).

2.2. Processes affecting the river plume

The initial (<500 km from the river mouth) structure of the Amazon River plume is mainly influenced by a variety of processes over the north Brazilian shelf (Geyer et al., 1991), such as strong tides (Curtin & Legeckis, 1986; Gibbs, 1982) and the NBC (Flagg, Gordon & McDowell, 1986; Nikiema, Devenon & Baklouti, 2007; Richardson & McKee, 1984). Once the plume spreads beyond the north Brazilian shelf, river discharge, trade winds, tropical cyclones and precipitation modulate the river plume on large time- and spatial scales (several months and hundreds of km). These processes that act on the larger scales are discussed in this section.

2.2.1. River discharge

On interannual time scales, the influence of river discharge fluctuations on the characteristics of the river plume is debated. For instance, Zeng et al. (2008) finds a strong correlation between plume size and Amazon River discharge. However, Semyon A. Grodsky, Johnson, Carton and Bryan (2015) showed that the magnitude of anomalous sea-surface salinity (SSS) variability, simulated without interannual variations of river discharge but with variable atmospheric forcing, is comparable to observations. Additionally, Fournier et al. (2017) use records from 2010–2014 to conclude that August SSSs in the Northern plume pathway are not controlled by Amazon River discharge variations.

2.2.2. Wind

The moderate and persistent northeast trade winds are found in the northern part of the plume, the subtropics (10°–30°N), and play an important role in the river plume's characteristics (Hellerman, 1980). Strong winds increase horizontal advection of the river plume, through Ekman transport perpendicular to the wind direction (deflection to the right in the Northern Hemisphere), modulating the overall flow direction of the plume.

The wind direction and -strength are dominated by the seasonal migration of the ITCZ, which is located over the southern part of the plume (10°N–10°S). Winds are directed slightly northwards from April to October and southwards throughout the rest of the year. However, the north-and southward components of the wind are small relative to the westward component. The variability of both the wind direction and -magnitude is smallest in the summer months. A strong cross-shore wind component is associated with decreased northward spreading of the river plume (Fournier et al., 2017).

2.2.3. Tropical cyclones

Tropical Cyclones (TCs) influence the river plume through additional local mixing. In years in which multiple (strong) cyclones cross the path of the river plume, the river plume undergoes increased mixing, which in turn decreases the stratification stability (Bender & Ginis, 2000). TCs are found north of 10°N and travel westward from June to November. From 1960–2000, 79 hurricanes passed directly over the river plume (Ffield, 2007).

Intensification of TCs occurs when the vertical wind shear throughout the whole troposphere (~800 mbar to 200 mbar) is less than 10 m/s (Gray, 1968). Stronger vertical wind shears disrupt the formation of tropical cyclones or decrease their strength, sometimes eliminating a present cyclone entirely. Additionally, high ocean surface temperatures decrease vertical wind shear, increasing the prevalence ofTCs. It follows that the river plume causes an enhancing effect on TCs. The warm coloured river plume blocks sunlight from penetrating beyond the mixed

layer (ML), leading to cooler subsurface waters. This intensifies TCs through their interaction with the subsurface (Newinger & Toumi, 2015).

All in all, this shows that SSTs play an important role in the the extent to which the river plume experiences mixing.

2.2.4. Precipitation

Thirdly, precipitation plays a role in the river plume's characteristics as it provides an additional source of freshwater in the WTNA. It has the potential to contribute to the buoyancy of the river plume, thereby intensifying the salinity stratification (Boutin, Martin, Reverdin, Yin & Gaillard, 2013).

V. J. Coles et al. (2013) examined numerical simulations with no-precipitation and no-river runs to conclude that west of 40°W, the riverine influence dominates over precipitation in modulating sea surface salinity. The precipitation volume in the region of interest (5°S–25°N and 70°W–25°W, Fig. 2.4) is approximately 520×10^9 m^3/y (calculated from Copernicus Climate Change Service (C3S), 2017). Considering that the combined Amazon and Orinoco river discharge is 14 times as high at 7300×10^9 m^3/y, precipitation is likely a much less important source of buoyant freshwater even though it is more widespread. However, in September, the ITCZ is at its northernmost position and precipitation-induced salinity anomalies approach river-induced salinity anomalies (V. J. Coles et al., 2013). The monthly spatial pattern, showing the meridional migration of the ITCZ, can be found in **??**.

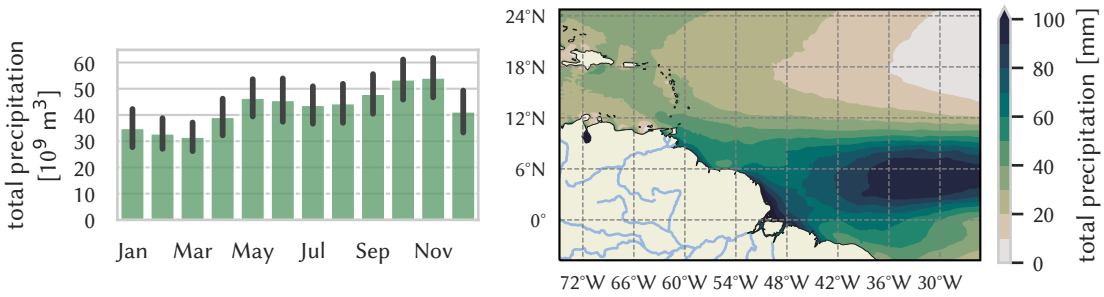

Figure 2.4: (a) Monthly mean volume of total precipitation ± standard deviation computed over over 5°S–25°N and 70°W–25°W, and (b) mean annual precipitation (calculated from Copernicus Climate Change Service (C3S), 2017).

2.2.5. El Niño–Southern Oscillation

The El Niño-Southern Oscillation (ENSO) may impact the river plume. The ENSO is a climate pattern which is characterised by irregular periodic variations of about two to seven years in global winds and SST over the tropical latitudes of the Pacific Ocean. The ENSO has been shown to influence climatic phenomena such as storms, droughts and floods around the world through the interaction of atmospheric and oceanic circulation known as teleconnections (Dai, Trenberth & Karl, 1998).

An El Niño event is associated with decreased precipitation in the Amazon River basin (Marengo & Espinoza, 2016). Furthermore, in the Caribbean region it is linked to higher average temperatures throughout the year (Malmgren, Winter & Chen, 1998), and milder dry and wet seasons (NOAA National Weather Services, 2016). A La Niña event is associated with more intense tropical storms (Klotzbach, 2011; NOAA National Weather Services, 2016) and more extreme dry and wet seasons in the northeast Caribbean (NOAA National Weather Services, 2016).

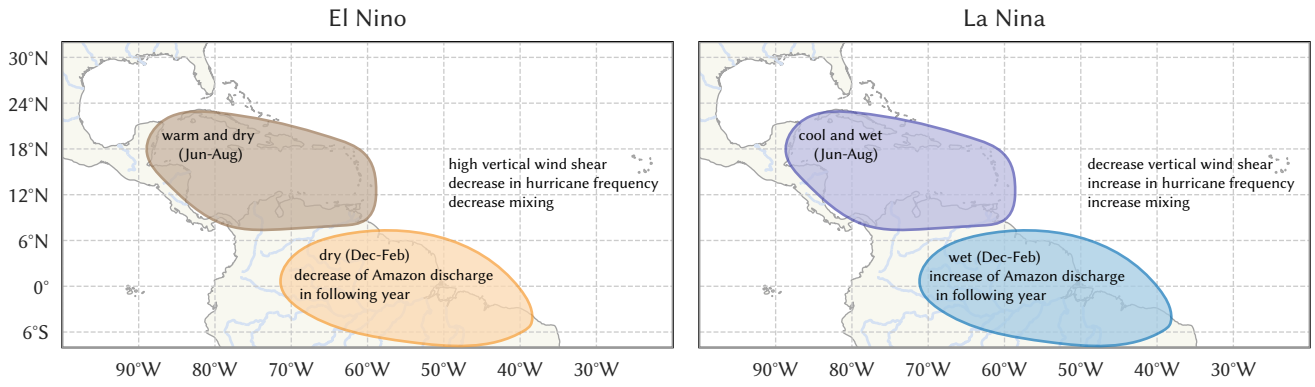

Figure 2.5: Effects of (a) El Niño and (b) La Niña on the Caribbean region (NOAA National Weather Services, 2016).

2.2.6. Madden-Julian Oscillation

The Madden-Julian Oscillation (MJO) is a convective oscillation in the tropical atmosphere, propagating eastward at about 5 m/s. It is the principal component of the 30 to 90 day atmospheric variability (Zhang, 2005). The cyclonic phase adds moisture to the atmosphere and is characterised as being wet, whereas the anticyclonic phase reduces convection and results in drier weather.

The MJO affects multiple atmospheric processes, such as the rainfall variability in South America (Liebmann et al., 2004; Paegle, Byerle & Mo, 2000) and over the Caribbean Sea (Martin & Schumacher, 2011), the generation of tropical cyclones in the Caribbean Sea (Ferreira, Schubert & Hack, 1996; Maloney & Hartmann, 2000) and the equatorial surface winds in the Atlantic Ocean (Foltz & McPhaden, 2004). Therefore, it is important to take the effects of the MJO on the river plume characteristics into account.

The Wheeler and Hendon (2004) index quantifies the MJO using a phase space to denote location (phase) and strength (amplitude) of enhanced convection (see Fig. 3.5 and Section 3.4.2. Using this index, Martin and Schumacher (2011) found precipitation anomalies up to 50 % above the annual mean in phases 1 and 2 of the MJO, decreased strength of the prevailing easterly trade winds. Opposite results were found for phase 5 and 6. TCs are four times more likely to be generated when the trade winds are weakened by the MJO than when they are strengthened (Maloney & Hartmann, 2000).

2.3. Coral bleaching in the Caribbean

Coral bleaching and -mortality has long been a threat to Caribbean ecosystems. Mass coral bleaching events in the Caribbean have been recorded in 1998, 2005 and 2010 (NOAA Coral Reef Watch, 2019). Corals that are under stress from a multitude of environmental phenomena may expel their symbiotic algae (Wilkinson & Souter, 2008). As the coral animal is coloured by the presence of these algae, their absence causes the familiar sight of the white coral skeleton. Accordingly, this phenomenon is called coral bleaching. Furthermore, these algae are the primary source of energy for growth and reproduction of corals and coral reefs. When they are expelled, the coral is susceptible to starvation and disease. The reefs often recover from these stress events if conditions become more favourable, with their colour returning within months while full physiological recovery can take over a year (Fitt & Warner, 1995; Porter, Fitt, Spero, Rogers & White, 1989). However, reduced growth is often seen and the coral may skip reproduction for a season (Porter et al., 1989). Ultimately, coral death may occur of which the chance increases when repeated bleaching events take place in a short period of time.

Since the coral animal is very sensitive, relatively small changes in environmental phenomena cause damage. Stressors that are potentially linked to the Amazon-Orinoco river plume are discussed in this section.

2.3.1. Thermal stress

The most significant cause of recent coral bleaching has been an increase in thermal stress, since the maximum sea water temperature that Caribbean reef corals can tolerate is 29 °C (Wilkinson & Souter, 2008). If the temperature rises above this threshold for an extended period of time, it will stress corals and induce bleaching. The magnitude of the temperature increase and its duration are linked to the severity of the bleaching event.

To quantify and predict the severity of a thermal stress event, some concepts have been developed. Two commonly used concepts, HotSpots and degree heating weeks (DHWs), are both indices of coral bleaching-related thermal stress (Liu, Strong & Skirving, 2003; Skirving et al., 2006).

HotSpot

A HotSpot is an anomalous temperature based on the maximum of the monthly mean SST (i.e. the average SST of the hottest month of the year) (Wellington et al., 2001). It is therefore not a typically defined SST anomaly, which is based on the year-averaged SSTs.

Degree Heating Weeks

Biological systems such as coral reefs are not only affected by the intensity of an SST anomaly, which is indicated through HotSpot values, but also by the cumulative effects of such an anomaly. To include the cumulative effects, the thermal stress index DHW represents the accumulation of HotSpots for a given location, over a rolling 12-week time period (Liu et al., 2003). Because HotSpot values of less than 1 °C do not induce visible effects on corals, these are not included in the calculation of the DHW. One DHW is equivalent to one week of a 1 °C HotSpot value, or half a week of a 2 °C HotSpot value.

In general, bleaching occurs when DHW values exceed a threshold of 4, while widespread bleaching and mortality is likely with DHW values over 8 (Skirving et al., 2006).

2.3.2. Hurricanes and cyclonic storms

Hurricanes and cyclonic storms suspend sediments and increase turbidity, temporarily reducing the amount of UV radiation reaching the corals (Wilkinson & Souter, 2008). Furthermore, they can cause damage to coral through excessive wave impact (Wilkinson & Souter, 2008). However, storms on open oceans have the ability to cool water through mixing of hot surface waters with cooler, deeper waters (Wilkinson & Souter, 2008). This reduces thermal stress on the corals.

2.3.3. Salinity sensitivity

The salinity range of 25 psu to 40 psu in which coral reef communities do well is quite wide, but rapid loss occurs at higher salinities (Smith & Buddemeier, 1992). Coral mortality also occurs when salinities are under 20 psu for longer than 24 hours, with less extreme salinity depressions causing bleaching and altered metabolic rates (S. L. Coles & Jokiel, 1978; Muthiga & Szmant, 1987). These extreme salinities are very unlikely to be found in the Caribbean region. Therefore, it is unlikely that river plume-induced reduced salinity poses a risk for coral reefs in this region.

3

Data

In this chapter, the data sets used in this study are described and validated.

3.1. Ocean salinity, temperature, density and currents

Copernicus Marine Environment Monitoring Service's (CMEMS) Global Ocean Physical Reanalysis Product (GLORYS12V1) product is an eddy-resolving reanalysis based on the NEMO3.1 platform, using the ECMWF ERA-Interim reanalysis as atmospheric forcing (E. U. Copernicus Marine Environment Monitoring Service [CMEMS], 2018). River runoff in the model is sourced from Dai (2017). The reanalysis spans 25 years, from 1993 to 2018, with a horizontal grid size of 1/12° × 1/12° and 50 vertical levels from 0 m to 5500 m depth and layer thickness increasing from 1 m at surface to 500 m at depth. Because of the 25-year time span of the GLORYS12V1 product, it is sufficient for investigating El Niño-Southern Oscillation (ENSO)-induced plume variability as it is more than three times the ENSO time scale (see Section 2.2). Satellite altimetry and sea-surface temperature (SST) observations, as well as in-situ depth measurements of temperature and salinity are assimilated. in the simulation

3.1.1. Validation of the data set

The complex hydrodynamics of a river plume region are susceptible to model error. To ensure correct representation of the river plume, we compare sea-surface salinity (SSS) and SST to satellite data. In addition, HotSpots and degree heating weeks (DHWs) are calculated from the SSTs in order to verify that the GLORYS12V1 dataset is useable for predicting coral bleaching.

The difference between the model results and satellite observations are calculated in terms of mean difference and root mean square difference (RMSD). To this end, the surface layer of the GLORYS12V1 data is used, which is given at 0.49 m depth. Hereafter, the applicability of the model simulation is assessed.

Sea surface salinity

Satellite-derived SSS data are not assimilated in the GLORYS12V1 model, since these measurements are relatively recent and their accuracy is poor compared to in-situ measurements. However, spatial and temporal coverage of satellite measurements is considerably higher compared to that of in-situ measurements, which makes them highly effective in resolving SSS structures.

The Soil Moisture and Ocean Salinity (SMOS) L3v4 product is used for validation of SSS in GLORYS12V1. These are processed (level 3) SMOS satellite measurements with a 9-day timestep and a spatial resolution of 25 × 25 km^2. This product is available from June 2010 to December 2016 (Boutin, Vergely & Khvorostyanov, 2018).

SSSs from the surface layer of the GLORYS12V1 product are averaged over 9 days to match the temporal resolution of the SMOS data. Hereafter, mean differences and RMSDs are calculated

spatially and temporally, as shown in Fig. 3.1.

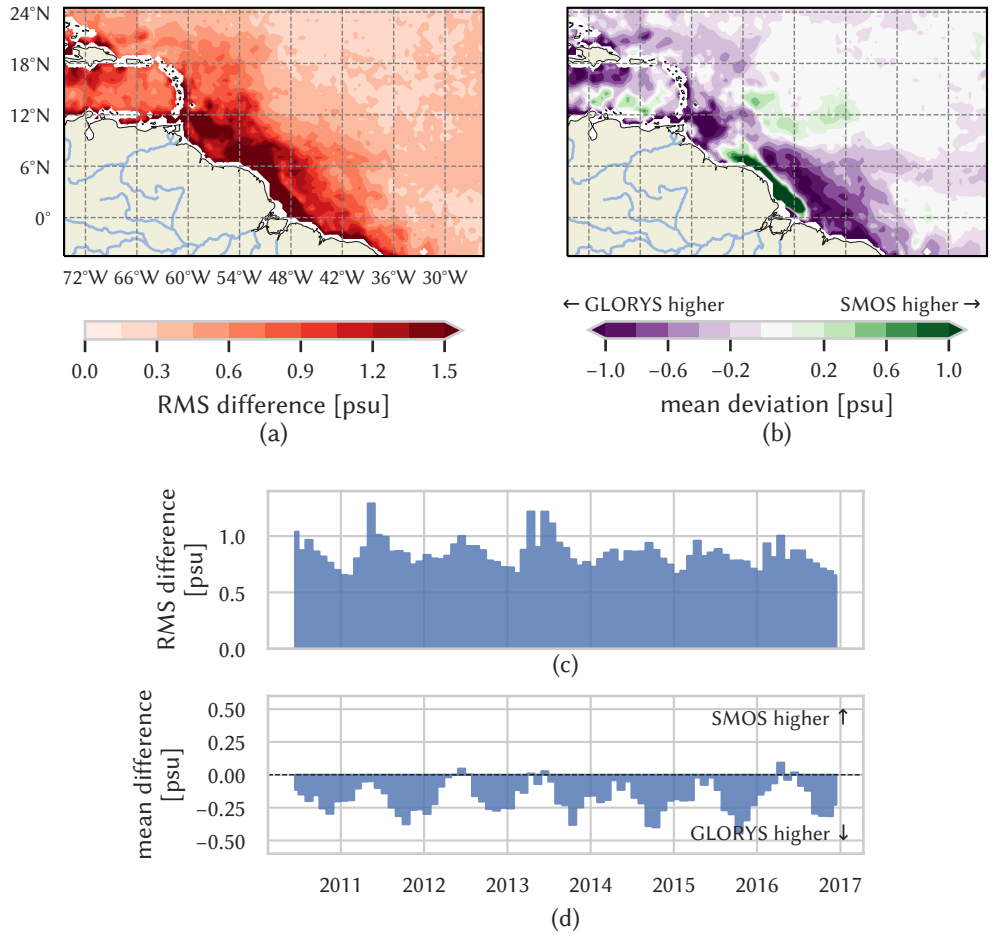

Figure 3.1: Comparison SMOS – GLORYS12V1 sea surface salinities. (a) RMSD and (b) mean difference from 2010-2016; (c) RMSD and (d) mean difference over 5°S–25°N and 75°–25°W.

GLORYS12V1 salinities are lower than those measured by SMOS in the area close to (<1000 km from) the river mouth. The model thus seems to overestimate the freshness of the water on and near the Brazilian shelf. This effect is not seen at the Orinoco river mouth. Upon spreading in the direction of the Lesser Antilles, GLORYS12V1 has a saline bias compared to SMOS measurements (Fig. 3.1b) with RMSD over 1.5 psu. This is especially the case in September and October, when the river plume is largest (Fig. 3.1d). It is possible that the river plume is in fact consistently fresher and more stable than it seems to be in the model.

Sea surface temperature

Although both in-situ and satellite SST measurements are assimilated in the GLORYS12V1 model, it is useful to know the extent of the remaining error. Therefore, satellite measurements of SST are compared to the surface layer model output. Furthermore, the model's ability to predict coral bleaching in this region is assessed, by means of comparison of HotSpot and DHW data.

The SST product by NOAA Coral Reef Watch (2018) is used for this comparison. This product is developed using two related reanalysis SST products and a near-real-time SST product. The HotSpot and DHW products are derived from these SSTs. The daily SSTs are given on a 5×5 km grid, starting from January 1985.

As the NOAA Coral Reef Watch (NOAA CRW) grid is finer than that of GLORYS12V1, it is regridded to match the GLORYS12V1 grid using linear interpolation. Hereafter, mean differences and RMSDs are calculated spatially and temporally, as shown in Fig. 3.2.

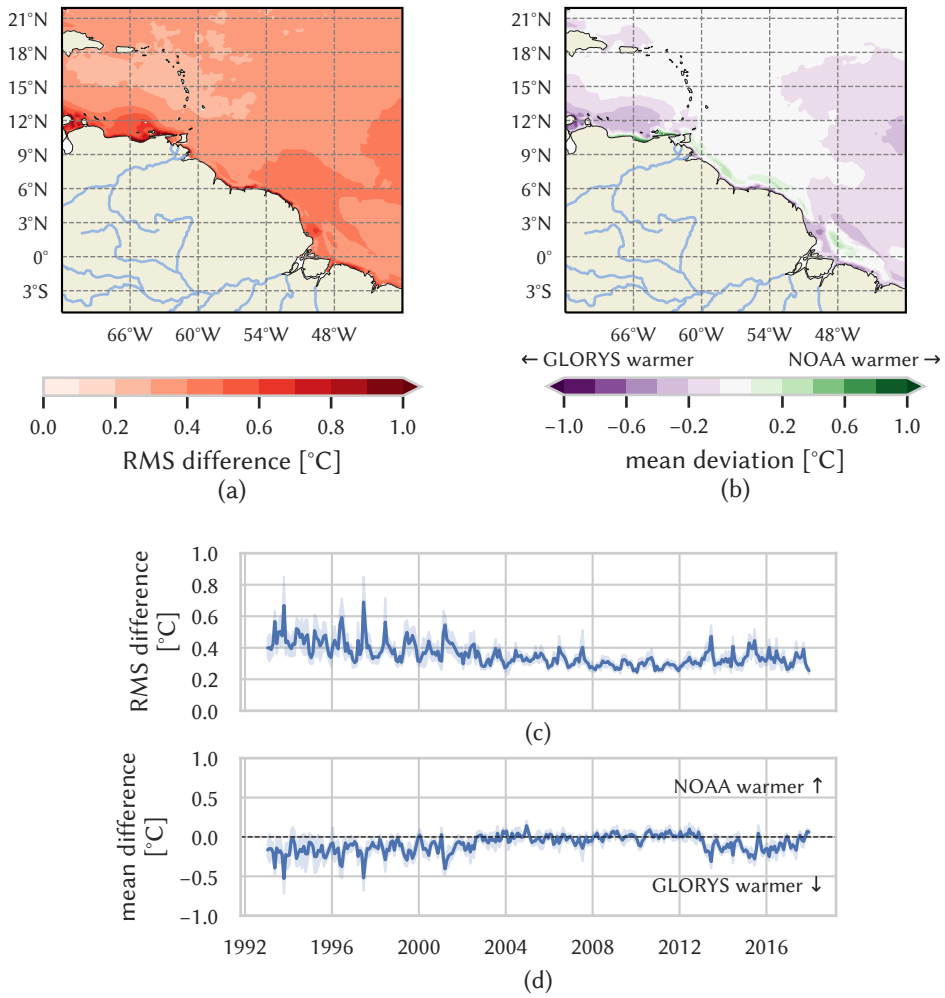

Figure 3.2: Comparison NOAA CRW – GLORYS12V1 SST: mean and RMS differences in space and time.

RMSDs between NOAA CRW and GLORYS12V1 SSTs are largest (up to 0.8 °C) along the Venezuelan shelf, while those in the Caribbean sea rarely exceed 0.5 °C (Fig. 3.2a). Mean differences between the two data sets are small as well, with GLORYS12V1 slightly overestimating the SST compared to NOAA CRW in the upwelling region along the Venezuelan coast. Averaged over the whole region, RMSDs are also generally small, with the largest differences seen in the summer months (Fig. 3.2c). From 2002 onwards, quality improvement of GLORYS12V1 model results due to deployed ARGO floats is observed in Fig. 3.2c.

For validation of the HotSpot and DHW values, see Appendix A. As any quantifying method, these threshold approaches come with some drawbacks. Firstly, when using different datasets, thresholds may not be comparable (Mumby, Chisholm, Clark, Hedley & Jaubert, 2001). Secondly, when locations have differing coral species compositions which react differently to thermal stress, the thresholds may not be comparable (Baird & Marshall, 2002; Hoegh-Guldberg & Salvat, 1995). Furthermore, the threshold methods disregard other climatological variables that may induce bleaching, such as the influence of clouds on radiation stress (Mumby et al., 2001). Additionally, the used thresholds are invariable and make no distinction between countries or reefs within countries, while the onset of bleaching may differ (McWilliams, Côté, Gill, Sutherland & Watkinson, 2005). Lastly, threshold methods may predict the onset of bleaching, but present no quantification of intensity or geographic extent of a bleaching event (McWilliams et al., 2005).

3.2. River discharge

The Amazon river discharge is obtained from the National Center for Atmospheric Research (NCAR) Research Data Archive (Dai, 2017). The discharge is generally measured using water level measurements combined with a calibrated rating curve that links water levels to discharges.

Orinoco discharge data from SO-HYBAM (2019) are used, which provides monthly discharges from 2003–2018. These 15 years of values overlap with GLORYS12V1, which is 8 years more than provided by (Dai, 2017) (see Fig. 3.3).

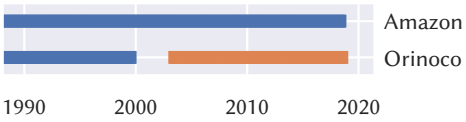

Figure 3.3: Availability of discharge data in GLORYS12V1 (blue) and SO-HYBAM (2019) (orange).

3.3. Wind speed and -direction, vertical wind shear and precipitation

The ECMWF ERA5 data set is a reanalysis combining forecast models and data assimilation with archived observations, resulting in a global data set of atmospheric parameters. The ERA5 data set has a temporal coverage from 1979 to present (as of March 2020) on a spatial grid of 0.25° × 0.25°. The data is available on 37 pressure levels from 1 hPa to 1000 hPa, as well as on single levels for specific parameters. For this study, ERA5 monthly averaged data are used. Single-level parameters are 10 m u- and v-components of wind, 2 m temperature and total precipitation. Furthermore, u- and v-components of wind at 200 mbar and 850 mbar pressure levels are used to calculate wind shear.

3.4. Teleconnection indices

In this section, the used climatic indices are discussed.

3.4.1. El Niño-Southern Oscillation

The index used in this study to quantify the ENSO is the Multivariate ENSO Index (MEI) (NOAA Physical Sciences Laboratory, 2019). This is a bi-monthly index, meaning that it is calculated on 12 overlapping 2-month periods per year (Dec–Jan, Jan–Feb, etc.). It is based on the leading Empirical Orthogonal Functions (EOFs) of five variables, being sea level pressure (SLP), SST, zonal and meridional components of surface wind and outgoing longwave radiation over the tropical Pacific basin. Thresholds of 0.5 are used for El Niño and −0.5 for La Niña conditions. Each phase results in predictable changes in SST, air temperature, precipitation, and winds (see Section 2.2.5). Values from 1993 to 2017 are given in Fig. 3.4.

3.4.2. Madden-Julian Oscillation

The Madden-Julian Oscillation (MJO) index proposed by Wheeler and Hendon (2004) is used in this study. This MJO index is formed by two Principal Components (PCs) of combined lower- and upper-level winds and outgoing longwave rediation, called Real-time Multivariate MJO series (RMM series). Combining these two RMM series results in phase and amplitude values describing the MJO (Fig. 3.5). The index is seasonally independent and uses all longitudes, making it able to describe the propagation of the oscillation around the world, with its location described by the eight phases. The strength of the oscillation is represented by the amplitude of the index, with amplitudes over 1 considered to be strong MJO events.

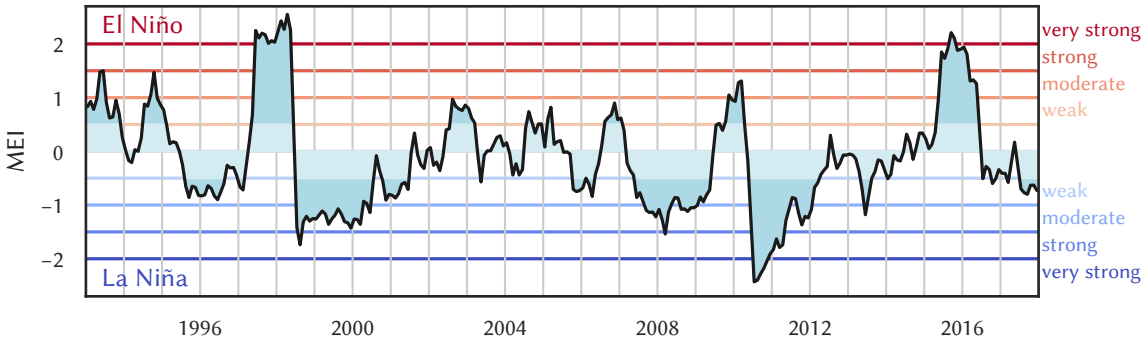

Figure 3.4: Multivariate ENSO Index (MEI) from 1993 to 2017 (NOAA Physical Sciences Laboratory, 2019). Blue shading is used to clarify the threshold of +/ − 0.5 for ENSO events.

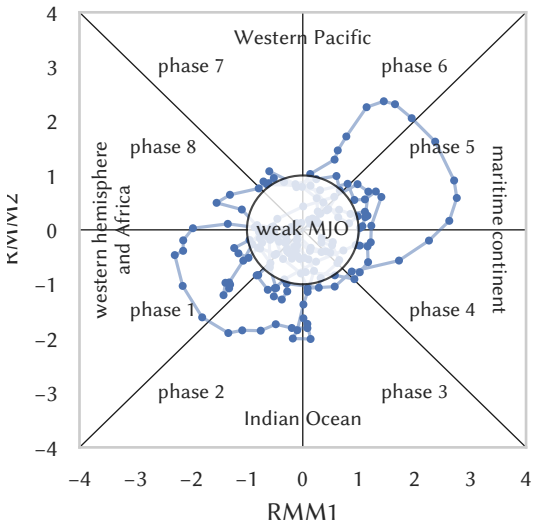

Figure 3.5: Phase-amplitude diagram of the Wheeler and Hendon (2004) MJO index. For illustrative purposes, each marker represents a day in Jul–Dec 2010 and connected markers are consecutive days. Approximate locations of enhanced convection are given around the diagram perimeter. Strong MJO activity is outside the middle circle (amplitude >1).

4

Validation of Sea Surface Salinity Threshold

In this chapter, we will show that plume waters can be distinguished from the surrounding waters using a sea-surface salinity (SSS) threshold, answering the first research subquestion. First, the threshold is determined and subsequently validated, under the assumption that plume waters have several characteristics that are distinctly different from open-ocean waters. These characteristics, SSS, sea-surface temperature (SST) and barrier layer thickness (BLT), are assessed using estimations of joint probability of occurrence.

4.1. Method

First, the relevant sampling region and -period are determined. Afterwards, the joint probability of occurrence of daily SSS and SST is estimated using kernel density estimates (KDEs), from which we can determine a SSS threshold. This threshold is then validated using the joint probability of occurrence of SST and BLT.

Concluding from the information presented in Section 2.1, the following is expected:

1. plume waters have lower SSS than open-ocean waters;
2. plume waters have higher SST than open-ocean waters;
3. plume waters have a thicker barrier layer (BL) than open-ocean waters.

4.1.1. Sample period

Months are identified in which the highest SSTs and the lowest SSS are found, indicating the presence of the river plume. Average monthly mean SST and SSS in the area of interest (5°S–20°N, 70°–40°W) are calculated over the years 1993–2017. The months in which the lowest average salinities are found are May to September (Fig. 4.1b). However, the months in which the river plume is largest are June to November (Ffield, 2007). The hottest months are also found from June to November, with peak temperatures in September and October (Fig. 4.1a). Because of the effects on coral bleaching, we are interested in the highest SSTs so the period of June to November is used as the sample period.

4.1.2. Sample region

A sample region is defined using the average plume extent in June to November (shaded contours in Fig. 4.2), the months in which the plume is largest (Ffield, 2007). To distinguish plume waters from open-ocean waters, we identify a region in which sample points include similar amounts of both. The longitudinal range of 70–42°W is large enough such that both low- and high-salinity waters are included, while the latitudinal range of 14–16°N is small enough to

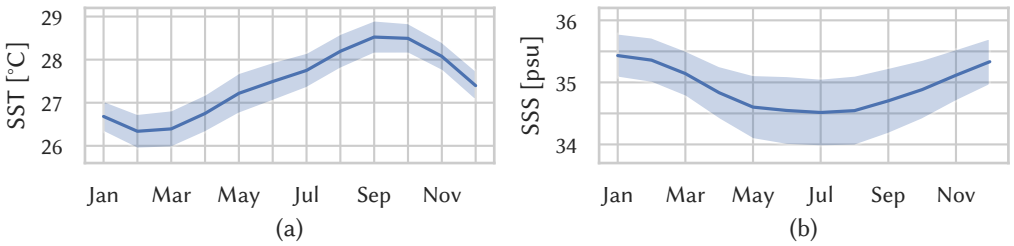

Figure 4.1: Monthly evolution of SST and SSS (mean ± one standard deviation) in the 5°S–20°N, 70°–40°W region. The hottest months are from June to November, with maximum temperatures from August to October. The minimum SSS are found from May to September.

minimize latitudinal differences in solar radiation. The sample grid is 0.5 × 0.5°, shown as blue dots in Fig. 4.2.

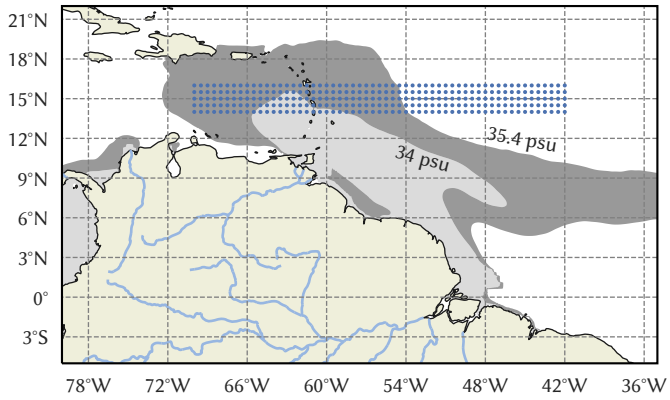

Figure 4.2: Sample points used for constructing the KDEs (blue markers). Light gray and gray shading are <34 psu and <35.4 psu contours of the average June–November SSS, respectively.

4.1.3. Kernel density estimation

The relation between parameters is investigated using KDEs. Kernel density estimation is a non-parametric method to estimate the probability density function (pdf) of a random variable. Being a smooth function, it is a useful alternative to a histogram. For joint pdfs, bivariate KDE are used.

The KDEs in this chapter are constructed using either daily or monthly sample data. A KDE is heavily dependent on the chosen bandwidth. Scott's rule, a rule-of-thumb method for determining the bandwidth, is used in all plots for consistency (Scott, 2015). Furthermore, a Gaussian kernel is used. The estimate is cut off at three times the bandwidth from the extreme data points.

4.1.4. Calculation of parameters

Because a thick barrier layer is expected as a result of the presence of the river plume, the BLT is used to validate the SSS threshold. To calculate the BLT, the isothermal layer depth (ILD) and mixed layer depth (MLD) must first be determined. The MLD is a function of σ_t, which is calculated using S and T from the Global Ocean Physical Reanalysis Product (GLORYS12V1) dataset. See Fig. 4.3 for an illustration of these layers.

Sigma-t

Sigma-t (σ_t) is the density as a function of local Absolute Salinity, Conservative Temperature and atmospheric pressure:

$$\sigma_t = \rho\left(S_A, T_C, p_0\right) - 1000\,\mathrm{kg/m^3} \tag{4.1}$$

To calculate σ_t, the Practical Salinity S_P given in the GLORYS12V1 product is converted to Absolute Salinity S_A, using the Thermodynamic Equation Of Seawater - 2010 (TEOS-10) standard (Roquet, Madec, McDougall & Barker, 2015). The Conservative Temperature is converted from the Potential Temperature at $p_0 = 0$.

ILD, MLD and BLT

The isothermal layer is the upper layer in which the temperature is approximately constant. The definition of the ILD is the depth at which the temperature deviates a prescribed amount of 0.2 °C from the surface temperature (de Boyer Montégut, Mignot, Lazar & Cravatte, 2007). While a reference depth of 10 m was originally prescribed to avoid density stratification, a reference depth of $z_{\mathrm{ref}} = 0.49$ m is used in this thesis because the salinity-induced pycnocline in the region of interest is in the 3 m to 30 m depth range (V. J. Coles et al., 2013). This reference depth corresponds to the surface layer in GLORYS12V1 simulations.

The ILD is calculated by determining the depth at which $T(z) = T_0 + \Delta T$, see Fig. 4.3b.

The mixed layer is the upper layer in which σ_t is approximately constant. It is defined as the depth at which the density increases from the surface value by an amount corresponding to the prescribed temperature decrease of 0.2 °C, while maintaining sea surface salinity and -pressure (de Boyer Montégut et al., 2007), shown in Fig. 4.3c.

$$\Delta T = -0.2 \tag{4.2}$$

$$\Delta\sigma_t = \sigma_t\left(T_0 + \Delta T, S_0, P_0\right) - \sigma\left(T_0, S_0, P_0\right) \tag{4.3}$$

$$\mathrm{MLD} = z\left(\sigma_{t,0} + \Delta\sigma_t\right) \tag{4.4}$$

The BLT is defined as the distance between the mixed- and isothermal layer depths (de Boyer Montégut et al., 2007), shown between Fig. 4.3b and c.

$$\mathrm{BLT} = \mathrm{ILD} - \mathrm{MLD} \tag{4.5}$$

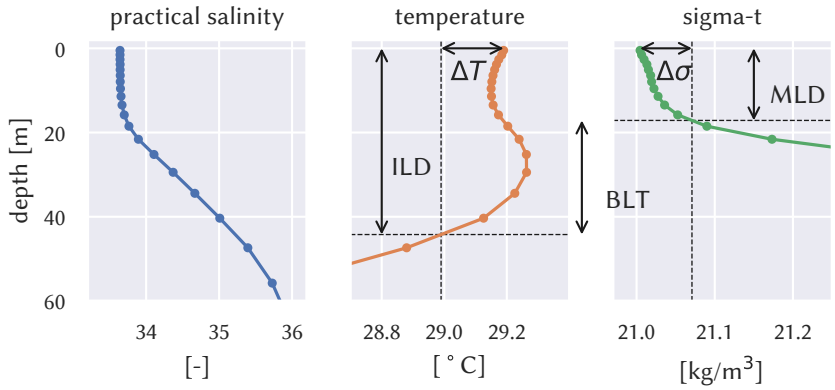

Figure 4.3: Illustration of ILD, MLD and resulting BLT.

4.2. Results

4.2.1. Relation between sea surface salinity and -temperature

To investigate the relation between SSS and SST, the KDE of daily SSS and SST is shown in Fig. 4.4. Values are taken from the months of June–November in the sampling grid of Fig. 4.2.

The dotted line shows the S = 35.4 psu threshold.

Two maxima are visible in the KDE in this figure. Firstly, this indicates that there is a compelling distinction between low- and high-salinity waters, roughly between 35 and 36 psu, confirming that these waters have distinctive characteristics. This is similar to the dynamically significant salinity threshold of 35.4 psu used by Ffield (2007), and will be used further in this study, meaning that waters with salinities below and above that threshold are referred to as 'plume waters' and 'open-ocean waters', respectively.

Secondly, it shows that the plume waters are warmer than the open-ocean waters in the same latitude band. The average SST difference is 0.93 °C in June–November. Extreme days (n = 68, or 1.5% of days) are found on which plume waters are >1.5 °C warmer than open-ocean waters.

Lastly, the spread in salinities is large in the plume waters, whereas the spread is only a narrow band between 36 psu and 37 psu in the open-ocean waters. Two explanations for this larger spread are: 1) spatial differences in the amount of entrainment of saline water, as river water has already travelled more than 1500 km by the time it reaches the latitudes used for this KDE; and 2) interannual variability of the river plume salinity.

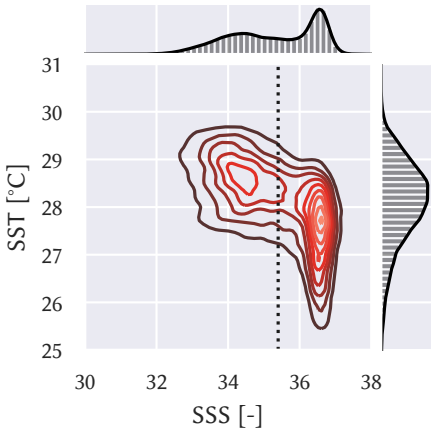

Figure 4.4: KDE of joint distribution of daily SST versus SSS in June–November using the sample grid given in Fig. 4.2. The dotted line gives S = 35.4 psu, as suggested by Ffield (2007).

4.2.2. Validation of SSS threshold using BLT differences

To validate the SSS threshold found in Section 4.2.1, the BLT is compared to SST using the threshold to distinguish plume- and open-ocean waters (Fig. 4.5).

The SSS threshold distinguishes between the waters in a way that two distinctly different maxima (expected values) are seen in the KDE. The plume waters are characterised by their 15.5 m to 26.5 m thick barrier layer, while the barrier layer in the open ocean is 3.7 m to 15.2 m (Fig. 4.5b). Although the two KDEs in Fig. 4.5a do overlap, it is clear that the plume waters are much more likely to have a thick barrier layer.

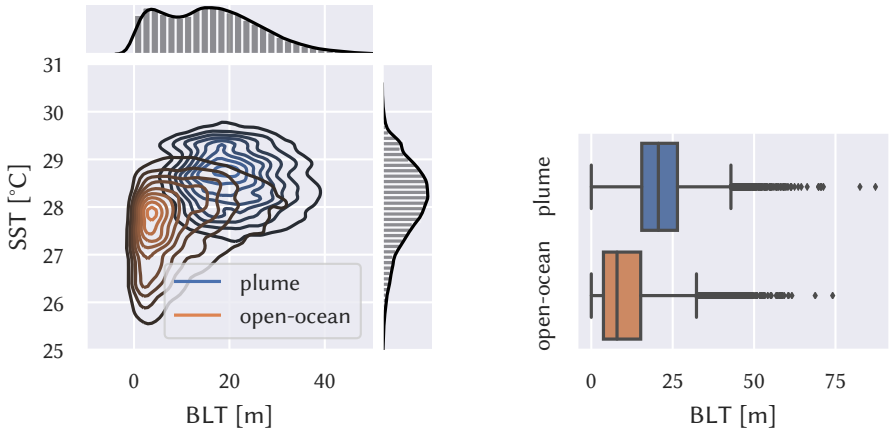

(a) (b)

Figure 4.5: (a) KDE of joint distribution of monthly mean BLT versus SST in June–November, in the sample region shown in Fig. 4.2. (b) Box plot of the BLT in plume- and open-ocean waters in June–November, showing the median, quartiles (box) and 1.5 times the interquartile range (IQR) (whiskers), including points outside the IQR (markers). The distinction between plume- and open-ocean waters is made at SSS = 35.4 psu.

4.3. Conclusion

In the sample region shown in Fig. 4.2, a salinity threshold S = 35.4 psu of was used to separate low- and high-salinity waters and investigate their characteristic SST and BLT. Using this threshold, an average SST difference of 0.93 °C is found in June–November. On 1.5% of days, this SST difference exceeds 1.5 °C. The results are in accordance with those found by Hu et al. (2004), with temperature differences of up to 1.5 °C. Furthermore, the monthly average BLT within the river plume is 11.2 m higher than in open-ocean waters.

The distinctly different characteristic SST and BLT in plume- and open-ocean waters confirm that their distinction can be made using the threshold. Accordingly, this threshold is used in Chapter 5 to investigate the variability of the river plume.

5

Variability of the river plume

The area, volume and thickness of the plume are determined using the sea-surface salinity (SSS) threshold that was defined in the previous chapter. To answer the second research question, these parameters are used to quantify the interannual and seasonal variability of the river plume. Furthermore, an Empirical Orthogonal Function (EOF) analysis is performed to uncover the modes of variability of SSS that best describe the river plume.

5.1. Method

The monthly mean surface area, volume and thickness of the river plume are calculated to quantify its seasonal and interannual variability. To separate data of plume-related parameters into uncorrelated orthogonal Principal Components (PCs), Empirical Orthogonal Function (EOF) analysis is used.

5.1.1. Calculation of plume area, volume and thickness

To calculate the plume area, the monthly average sea-surface salinity (SSS) of Global Ocean Physical Reanalysis Product (GLORYS12V1) is used. The plume area is defined as the sum of all grid cell areas within 0°–22°N and 72°W–42°W (Fig. 5.1) for which S < 35.4 psu.

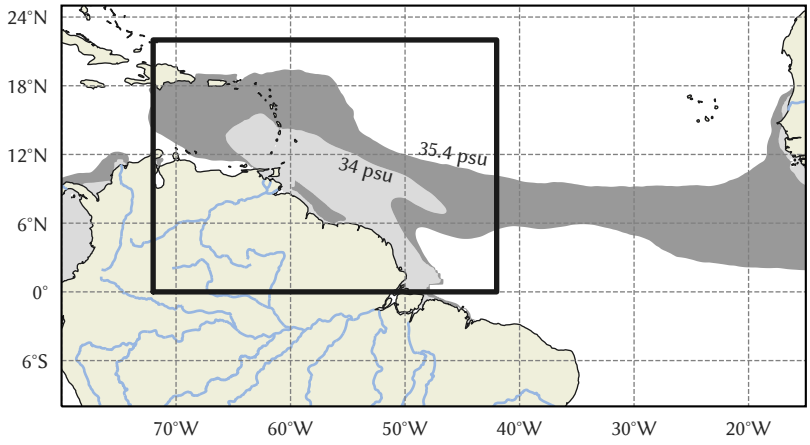

Figure 5.1: The black box shows the region over which the plume area, volume and thickness are calculated. Light gray and gray shading are <34 psu and <35.4 psu contours of the average June–November SSS, respectively.

The local plume thickness is defined as the depth at which S = 35.4 psu. The plume volume is calculated by multiplying each grid cell area where SSS <35.4 psu with local plume thickness.

5.1.2. Empirical Orthogonal Function analysis

Empirical Orthogonal Function (EOF) analysis is a tool widely used in oceanography and atmospheric science with the aim to reduce data dimensionality. A transformation is used to turn the input spatio-temporal data set into a set of uncorrelated maps (called Empirical Orthogonal Functions), and pricipal component time series (called Principal Components) corresponding to those maps. The EOFs represent patterns of variance and the PCs determine the contribution of every map to the original data set at each time. The Python library `eofs` was used for implementation the EOF analysis (Dawson, 2016).

The first EOFs generally contain a large portion of the total variance contained in the data set. Therefore, the subset of the first EOFs that are of interest can be singled out while the higher order EOFs are discarded. This greatly reduces the data dimensionality while still maintaining the essential variance present in the original data.

In the EOF analysis of SSS, the goal is to determine what PCs describe the variability of the river plume. Therefore, the influence of precipitation, which is present over the whole region but has a concentrated band in the Intertropical Convergence Zone (ITCZ) between 10°S–10°N, should be excluded as much as possible. However, the Amazon River mouth is located at 0° and is permanently directed in north-west direction. To include the whole river plume but exclude part of the precipitation response, the latitudinal extent is spatially restricted to 0°N–22°N. Furthermore, the focus is on the westward pathway of the river plume, thus the eastward pathway can be cut off. Therefore, the data used in the EOF analysis of SSS is longitudinally restricted to 72°W–42°W.

The physical parameters that are related to the river plume are SSS, sea-surface temperature (SST) and barrier layer thickness (BLT) (see Sections 4.2.1 and 4.2.2). EOFs and corresponding PCs of these parameters are calculated using detrended anomalies from the seasonal cycle. The temporal and spatial variability of the data set are investigated based on the leading five PCs and EOFs. The PCs that may relate to the river plume are identified through comparing their EOFs to the region that is generally affected by the river plume. PCs that are unlikely to have anything to do with the river plume can then be neglected, even if they contain a large fraction of the total variance.

To verify the relation between the river plume and a PC, the correlation coefficient between the PC and the river plume area is calculated.

5.2. Results

5.2.1. Seasonal variability of plume area, volume and thickness

The river plume has a strong seasonality, where the plume area ranges from a minimum of $0.99 \pm 0.30 \times 10^6$ km^2 in February–March to a maximum of $3.15 \pm 0.25 \times 10^6$ km^2 in August–October (Fig. 5.2a).

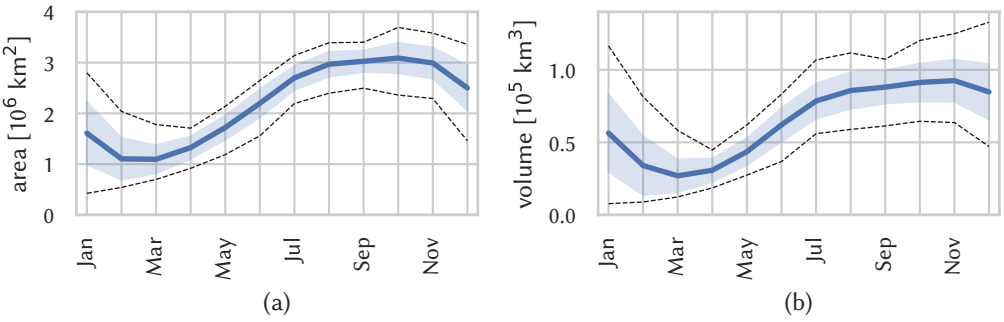

Figure 5.2: Monthly mean ± one standard deviation (shaded) of the (a) area and (b) volume of the plume, defined as $S < 35.4$ psu, from 1993–2017. Dashed lines show the monthly min-max range.

The river plume has a thickness of 24.5 ± 11.6 m in March–April–May (*mam*) (see also Fig. 5.3a).

Thereafter, it spreads further into the Atlantic Ocean, vertically entraining saline waters along the way. In this process, the 35.4 psu contour deepens and the river plume thickness increases to a maximum of 33.7 ± 15.1 m in December–January–February (*djf*).

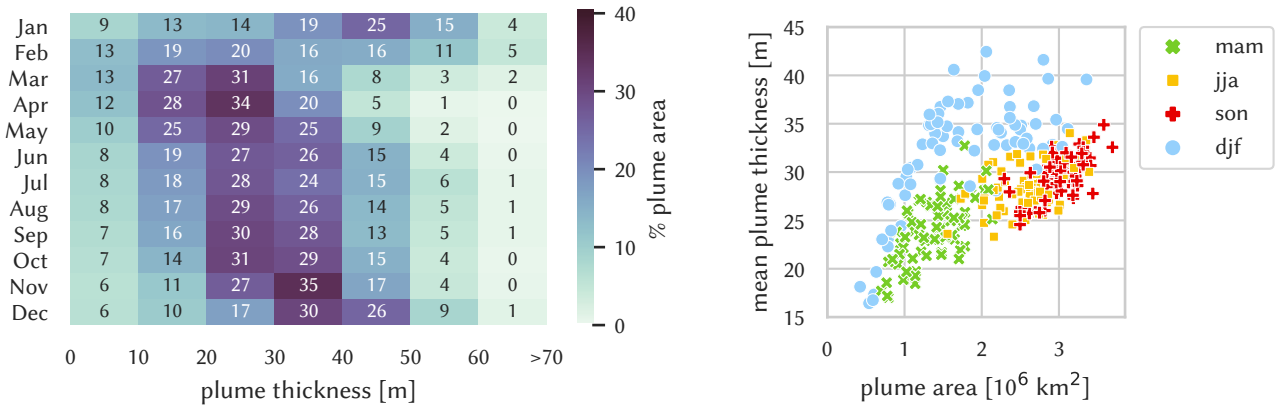

(a) (b)

Figure 5.3: (a) Distribution of the plume thickness (defined as $S < 35.4$ psu) as percentage of total plume area. (b) Scatter plot of monthly mean plume area and thickness, categorised by season: March–April–May (*mam*), June–July–August (*jja*), September–October–November (*son*) and December–January–February (*djf*).

The strong seasonality of the river plume can be seen in Fig. 5.3b, with the scatter points categorized by their respective 3-month season. Furthermore, we observe a moderately strong, positive relation between plume surface area and mean plume thickness.

The dissipation of the river plume in *djf* causes the large spread of plume thickness and -area in this season (Figs. 5.3a and 5.3b). In December of each year, the area and thickness of the plume are relatively consistent throughout the years. However, much more variability exists in January and February. This indicates that in some years, the plume persists for a longer period of time than in others. In *mam*, the variability is small, shown as a limited spread of markers in Fig. 5.3b, so that it can be concluded that the plume generally disintegrates before March/April.

5.2.2. Interannual variability of plume area, volume and thickness

The variations of river plume area and -thickness are shown in Fig. 5.4. Minima and maxima are shown for each plume cycle using red and green markers to highlight the interannual variability. A large annual maximum plume area correlates with large annual maximum thickness ($r = 0.78$, $p < 0.001$), which is in accordance with the positive relationship found in Fig. 5.3b.

The annual maximum plume area is most likely to be found in October (48 % of 25 years), but can also take place in August, September and November (20 %, 12 % and 20 %, respectively) with values of $3.15 \pm 0.25 \times 10^6$ km^2. The largest maximum plume area, found in 2009, is 1.5 times larger than the smallest one in 2016 with a difference of 1.20×10^6 km^2, demonstrating the immense interannual variability of the river plume. Furthermore, the annual *minimum* plume area varies greatly as well, with values of 0.42×10^6 km^2 and 1.53×10^6 km^2 in the years of largest contrast; a difference of more than one million km^2. The possible causes of this variability are discussed in Chapter 6.

The annual maximum plume thickness is 35.6 ± 3.2 m (Fig. 5.4), trailing the maximum plume area by three to four months (Fig. 5.2). This is because the river plume gradually mixes both horizontally and vertically, reducing its spatial extent and deepening the 35.4 psu contour.

Lastly, the annual minimum plume volume is highly variable ($0.23 \pm 0.10 \times 10^5$ km^3).

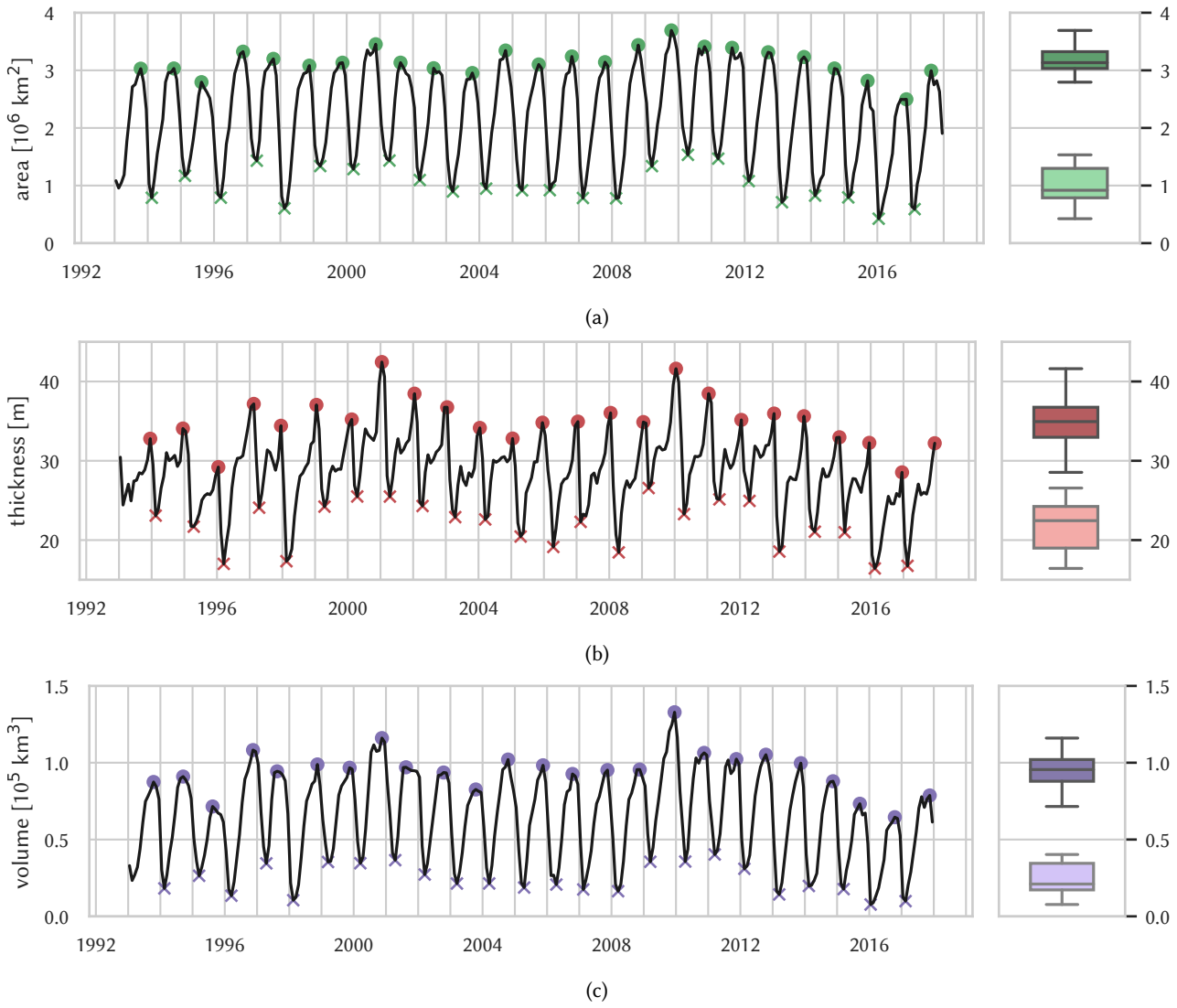

Figure 5.4: (a) Area, (b) thickness and (c) volume of the plume. Markers show minima and maxima in a plume plume cycle. Box plots show the distribution of these minima and maxima, with whiskers showing 1.5 times the interquartile range.

5.2.3. Patterns of sea-surface salinity variability

Since the seasonality, which constitutes a large fraction of the total variance, is removed from the data, the remaining variance is the result of locally varying atmospheric forcing and complex hydrodynamics. Therefore, the first five PCs of SSS together describe 51.6 % of the total variance, which is a relatively small amount. Nevertheless, the rest of the PCs are neglected because they all describe small amounts (<4 %) of variance (Fig. 5.5). Furthermore, the relevance of the leading PCs with respect to the plume variability is assessed through their correlation with the surface area of the river plume over time (Table 5.1). We assume that a strong correlation means that the PC contributes to the total plume area and thus is a river plume-specific mode of variability. PCs of higher orders than 5 do not correlate significantly with the previously calculated plume area.

The correlations of PC1 and PC5 with river plume area are weak or not significant. Therefore, we conclude that these do not relate to the river plume and can be neglected. The correlations of PC2 and 3 to the river plume area are strong, while PC4 shows a weaker, yet significant, correlation.

It should be noted that the sign of the pattern of correlation coefficients to the data set needs to be taken into account. A positive correlation of river plume area with PC2 indicates that there is a *negative* association with SSS (Fig. 5.6). In other words, if PC2 increases the size of

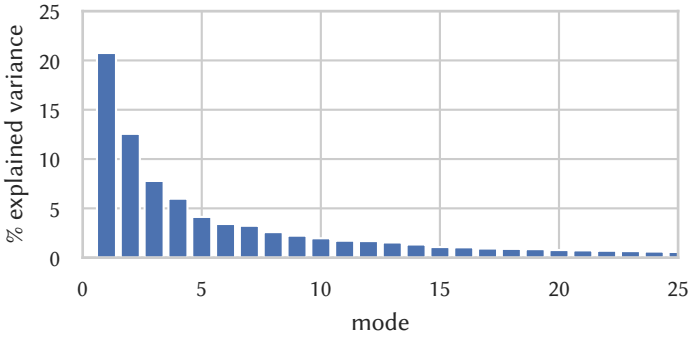

Figure 5.5: Percentage of explained variance for the first 25 PCs of SSS as anomaly from seasonality.

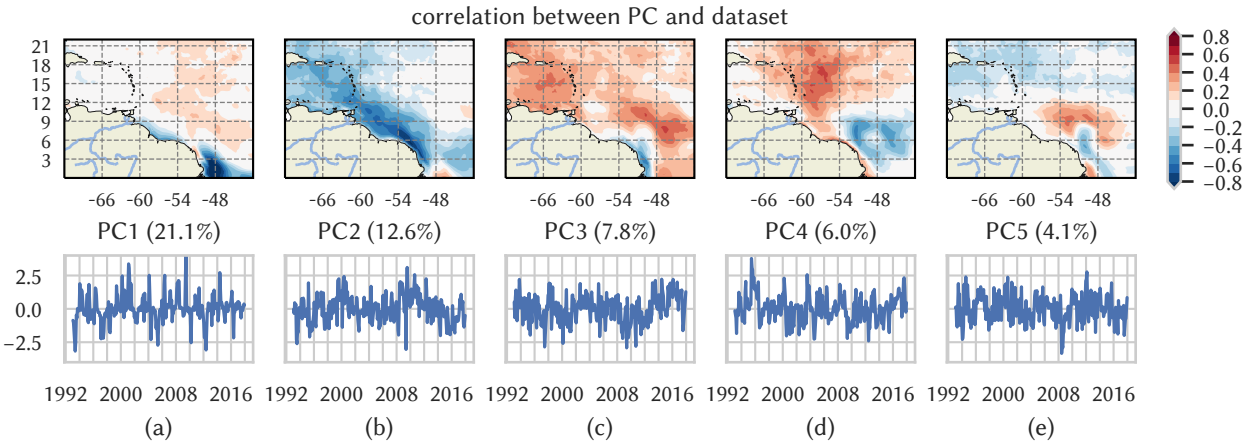

Figure 5.6: Leading 5 EOFs (top row) of sea-surface salinity with corresponding PCs, scaled to unit variance (bottom row). The percentage of explained variance of each mode is given in parentheses.

Table 5.1: Correlation coefficients of leading PCs of SSS with plume area as anomaly from seasonality. Only statistically significant ($p < 0.05$) correlations where $|r| \geq 0.25$ are shown.

	variance fraction	correlation with plume area	p
SSS PC1	21.1%	−0.11	0.063
SSS PC2	12.6%	0.46	<0.001
SSS PC3	7.8%	−0.54	<0.001
SSS PC4	6.0%	−0.25	<0.001
SSS PC5	4.1%	0.21	<0.001

the river plume, we expect a positive correlation. The opposite holds for PC3 and PC4. The correlations in Table 5.1 comply with these expectations.

Description of the first five EOFs of SSS

The first PC of SSS correlates negatively with the region just outside the Amazon River mouth (Fig. 5.6a). However, this PC does not relate strongly to Amazon river discharge ($r = 0.14$, $p = 0.016$), but rather to total precipitation anomaly in that region ($0.40 < r < 0.62$, $p < 0.001$, not shown). This indicates that PC1 describes the SSS response to precipitation in the ITCZ, which is concentrated in the 3°S–3°N band. It has little relation to the river plume.

The second PC describes 12.6 % of the total SSS variance and correlates with the northwest along-shelf pathway of the river plume. The blue region in the EOF map in Fig. 5.6b denotes

negative correlation to the corresponding PC. In other words, in a month where the value of PC2 is high, it contributes to low SSSs in this region. It should be noted that the actual SSS at a certain location is the sum of the contributions of all PCs, and that values of individual PCs only give an indication of the salinity *pattern* in the region with which they correlate.

The third PC describes 7.8 % of the total variance and correlates positively with the spatial pattern shown in red in EOF3, with concentrated regions of correlation in the Caribbean Sea and the eastward retroflection pathway of the river plume. It correlates strongly with the plume area ($r = -0.54$), so we conclude that it is related to river plume variability.

The fourth PC describes 6.0 % of the total SSS variance and is correlated with the northward pathway of the river plume that flows along the Lesser Antilles. The correlation with the plume area is −0.25, so this PC is taken into account in defining river plume variability. It is important to note that PC4 also correlates negatively with SSS in the retroflection pathway (6°N, 48°W). This should be taken into account when interpreting the results.

The fifth PC describes only 4.1 % of the total variance, the correlation map does not show distinctive plume pathways and the correlation with plume area is <0.25. Therefore, this OC is neglected

PC2 and PC3 thus describe most of the variance of the river plume at 20.4 % of the total variance in the region, with a small addition of PC4 (6.0 % of the total variance). This makes these three PCs most interesting for analysis of the river plume variability. Therefore, they will be used in Chapter 6 for analysing possible modulators of the river plume. The combined percentage of described variance for these three PCs is 26.4 %.

Reconstructed fields using these three PCs demonstrate an acceptable level of accordance with the river plume structure (see Appendix E).

5.2.4. Patterns of sea-surface temperature variability

An EOF analysis is performed on detrended SST anomalies to reveal possible plume-related modes of variability.

The first five PCs of SST jointly describe 80.7 % of the variance of the SST data (Fig. 5.7). The first PC describes SST response to large-scale atmospheric forcing in the Western Tropical North Atlantic (WTNA). The second PC correlates most with the northern part of the Caribbean and has a weak negative correlation with the eastward pathway of the plume. The third PC describes the SSTs in the along-shelf region. PC4 and 5 describe small percentages of variance (<4 %) and are not further discussed.

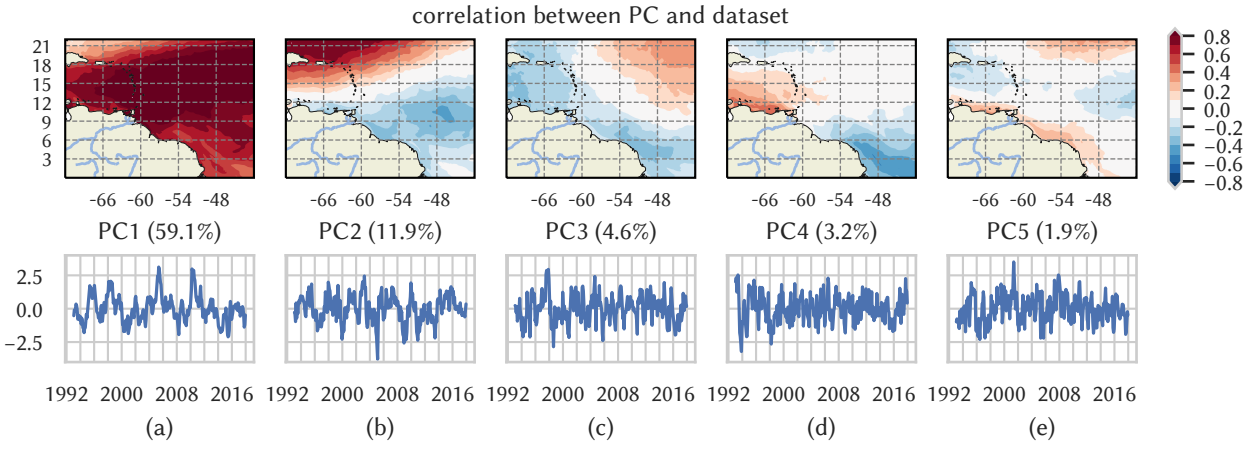

Figure 5.7: Leading 5 EOFs of sea-surface temperature (top row) with corresponding PCs, scaled to unit variance (bottom row). The percentage of explained variance of each mode is given in parentheses.

The river plume shape is not visible in any of the first three EOFs (upper row of Fig. 5.7), so no apparent temperature signature can be attributed to the river plume. However, correlation

coefficients to the river plume area shown in Table 5.2 suggest that the SST pattern described by PC2 may be related to the river plume.

Table 5.2: Correlation coefficients of leading PCs of SST with plume area as anomaly from seasonality. Only statistically significant ($p < 0.05$) correlations where $|r| \geq 0.25$ are shown.

	variance fraction	correlation with plume area	p
SST PC1	59.1%	0.08	0.148
SST PC2	11.9%	−0.31	<0.001
SST PC3	4.6%	0.11	0.055
SST PC4	3.2%	0.10	0.091
SST PC5	1.9%	0.20	<0.001

5.3. Conclusion

The purpose of this chapter was to investigate how the river plume varies interannually, thereby answering the second research subquestion.

The seasonal variability was used to determine the start and end of one plume cycle. The river plume, as bounded by the 35.4 psu isohaline, is a strongly seasonal phenomenon with its largest area found in October, which follows the annual maximum Amazon River discharge by five months. The maximum thickness is found in December–January–February (*djf*), and the plume has generally disintegrated by March. Therefore, the plume cycle was defined to range from April to March.

The large variability of the annual maximum river plume area (Fig. 5.4a) shows that its extent varies greatly throughout the years. The annual maximum of plume area is $3.15 \pm 0.25 \times 10^6$ km^2, and the annual minimum area ranges from 0.42×10^6 km^2 to 1.53×10^6 km^2. Therefore, it is likely that the extent of its influence on SSTs varies as well.

The variability of the annual minimum river plume volume indicates a large interannual variability of the mixing rate of the river plume (Fig. 5.4c). This suggests that in some plume cycles, the fresh ($S < 35.4$ psu) plume waters remain in the region for a longer period of time and may reduce the background salinity in the following year.

An EOF analysis was used to reveal the dominant modes interannual of variability of SSS in the region of interest. This analysis reveals patterns of SSS anomalies that are potentially associated with the river plume. The PCs that describe the river plume were identified through a comparison to the previously calculated river plume area. PC2, 3 and 4 were concluded to jointly describe the river plume and will be used in Chapter 6 to investigate the modulators of river plume characteristics. Reconstructed fields of SSS anomalies using only these three PCs show a good accordance with the general river plume salinity structure (see Appendix E).

Additionally, an EOF analysis was performed on SSTs. Although the correlation of river plume area with PC2 of SST indicates that this mode of variability does relate to the river plume area, its spatial pattern does not suggest that it describes a mode of variability of the river plume. Accordingly, we conclude that no river plume-related modes of variability were revealed based on the EOF analysis of SST. The effect of the river plume on SST is further investigated in Chapter 7.

6

Modulators of river plume characteristics

In the previous chapter, it was shown that the 2nd, 3rd and 4th Principal Component (PC) of sea-surface salinity (SSS) anomalies jointly describe the interannual variability of the river plume. In this chapter, the third sub-question is answered, which concerns the processes affecting the interannual variability of the Amazon-Orinoco river plume. The modulators of plume characteristics are examined by quantifying the influence of the modulator on the river plume, taking into account the possible lag of the response.

6.1. Method

The second, third and fourth Principal Component (PC) of sea-surface salinity (SSS) jointly describe the river plume. For this reason, these are used to perform bivariate analyses on in this chapter. They will be referred to as 'plume PCs'.

All seasonally-varying variables discussed in this chapter are detrended and deseasonalised to expose fluctuations on interannual timescales, by calculating the anomaly from the local 25-year monthly mean.

First, the effect of freshwater inputs, river discharge and precipitation, on the river plume are assessed (Sections 6.2.1 and 6.2.2). Then, teleconnection indices of the El Niño-Southern Oscillation (ENSO) and the Madden-Julian Oscillation (MJO) are considered (Sections 6.2.6 and 6.2.7). Lastly, the effects of changes in wind speed, -direction and -shear on the river plume are investigated (Sections 6.2.3 to 6.2.5).

6.1.1. Statistical analysis

Pearson r correlation is used as a means of bivariate analysis. To rule out whether a non-linear relationship exists between two variables, Spearman's rank correlation ρ is also calculated. This rank correlation is only featured when $\rho \gg r$. In both cases, the significance of the relationship is determined using a beta distribution to compute a two-sided p-value.

For all calculated correlations, monthly values are used over a period of 25 years, so that in all cases $n = 300$ unless stated otherwise. Based on the sample size, the correlation is statistically significant at a 99.9 % confidence interval when $|r| \geq 0.189$. Only stronger correlations, where $|r| \geq 0.25$, are shown. It follows that these are all statistically significant with $p < 0.001$.

Because there could be a delay between the modulator and the river plume response, the lag is calculated with a cross-correlation analysis. Here, the lag is defined as the shift for which the maximum absolute cross-correlation is found. We assume that responses with a computed lag of more than 12 months are coincidental, so these are not shown. The maximum absolute correlation is is called r_{lag} while the correlation at zero lag is called r_0.

6.1.2. Temporally varying variables

River discharge and the Multivariate ENSO Index (MEI) only depend on time, not on space. In these cases, the correlation coefficients between a modulator and the plume PCs are calculated to determine to what extent the modulator affects the river plume.

6.1.3. Spatio-temporally varying variables

Precipitation, wind speed, wind direction and vertical wind shear are river plume modulators that vary in time and space. Leading PCs are first calculated and subsequently compared with the SSS PCs, to determine the lag between the forcing and the response. The resulting lag is then used to produce a correlation map of correlation coefficients between the modulator and the plume PCs.

Vertical wind shear

The wind shear is defined as the absolute difference between the wind vectors ($\vec{W}$) at the 850 mbar and 200 mbar vertical levels.

$$\text{wind shear} = \left|\vec{W}_{200\,\text{mbar}} - \vec{W}_{850\,\text{mbar}}\right| \tag{6.1}$$

Wind direction

The prevailing winds in the region are the trade winds, which are persistently directed to the west throughout the year. Therefore, meridional (N-S) wind speed is used as a measure for wind direction.

6.1.4. MJO compositing

Daily anomalies from the annual cycle of SSS in the months July–September are composited by the phase of the MJO for all strong MJO events (amplitude >1). In these months, the river plume area is increasing and the greatest influence of the MJO on the plume characteristics is expected. The average of the daily anomaly in each MJO phase is then determined in order to resolve the influence of the MJO on these variables. A two-tailed t-test is used to calculate the significance using a 99 % confidence interval.

6.2. Results

6.2.1. River discharge

Previous studies have shown that interannual variations of river discharge are not an effective predictor of interannual plume variability (Fournier et al., 2017; Semyon A. Grodsky et al., 2015; Semyon A Grodsky, Reverdin, Carton & Coles, 2014). However, these studies use 5 or less years of satellite-derived SSS data to draw these conclusions, whereas the relative importance of the processes modulating the river plume may vary over much larger time scales. Therefore, it is interesting to quantify the observed response of the separate SSS modes of the river plume to anomalous river discharges, using 25 years of SSS- and discharge data.

If a high river discharge causes low salinity anomalies, a negative association to SSS is expected 3 to 6 months after Amazon discharge and up to 2 months after Orinoco discharge. A positive correlation of river discharge with PC2 of SSS would confirm this. The opposite holds for PC3 and PC4.

PC4 of SSS has the strongest correlation with Amazon river discharge at a lag of three months (Table 6.1). This negative correlation indicates that anomalously low SSSs are observed east of the Caribbean Sea three months after a high Amazon river discharge. While this correlation is weak, it indicates that anomalous discharges of the Amazon river do slightly affect the interannual variability of the river plume.

The results do not indicate that the Orinoco River discharge anomalies significantly affect the interannual variability of the river plume (Table 6.1). Correlations are calculated using 15

Table 6.1: Correlations (r_0 and r_{lag}) of plume PCs with Amazon and Orinoco discharges. Only correlations where $|r| \geq 0.25$ are shown. The lag in months for r_{lag} is given in parentheses.

	Amazon		Orinoco[a]	
	r_0	r_{lag} (lag)	r_0	r_{lag} (lag)
PC2 (along-shelf)	0.18	0.18 (0)	0.04	0.24 (-22)
PC3 (overall spreading)	−0.09	0.24 (22)	−0.10	0.27 (37)
PC4 (northward spreading)	−0.17	−0.28 (3)	0.19	−0.37 (39)

[a] $n = 180$

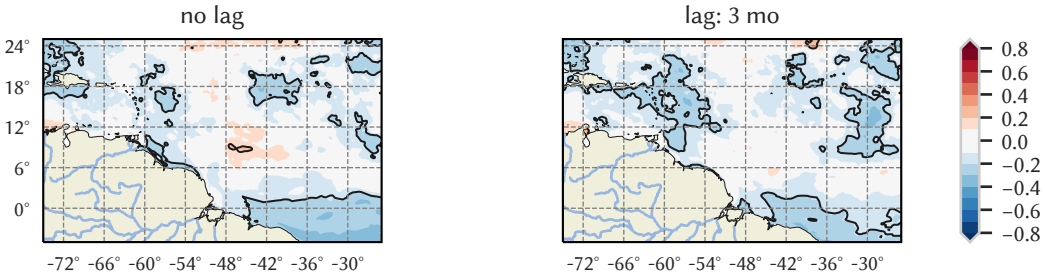

Figure 6.1: Correlation maps showing the correlation coefficient between Amazon river discharge as anomaly from seasonality and SSS anomalies from seasonality using 0 and 3 months lag. The black contour shows 99.9 % significance. Strong correlations between SSS anomaly data and the respective PCs are shown as purple dotted ($r < -0.3$) and striped ($r > 0.3$) hatching.

years (180 months) of data instead of 25 (300 months) but are all low, insignificant or strongest at a lag of more than 12 months.

In Fig. 6.1, a weak negative correlation is shown of Amazon river discharge with SSS east of the Caribbean Islands, in the region best described by PC4 of the SSS. This correlation is strongest at a lag of three months. Correlations of similar strength are found east of 48°W as well. This is possibly due to the ENSO which modulates not only the Amazon River discharge but also hydrodynamics in the Western Tropical North Atlantic (WTNA). Furthermore, the band of negative correlations south of the equator can be explained by precipitation-induced anomalous SSS in the Intertropical Convergence Zone (ITCZ), which modulates the Amazon river discharge as well.

6.2.2. Precipitation

Precipitation decreases the SSS directly, without lag. Because we define the river plume using PCs of SSS, it is likely that some of the SSS response to precipitation is still present in the plume PCs. This would be confirmed by a positive correlation of total precipitation anomaly (TPA) with PC2 of SSS and a negative correlation with PC3 and PC4.

To verify the assumption of zero lag between the two processes, results of cross-correlations between the plume PCs and TPA PCs are shown in Table 6.2. The strongest correlation coefficients are found at 0 and 1 months lag.

Correlation maps of plume PCs with TPA at one month lag (Fig. 6.2) show positive correlation coefficients between TPA and PC2 of SSS, and negative ones with PC3. These observations confirm that low SSS are found when TPA is high. The location of the weak negative correlation coefficients in Fig. 6.2c south of 12°N suggest that high precipitation in this region freshens the local retroflection region, while there is no evidence for a connection to the northwest pathway. Precipitation has previously been found to be of similar importance to the Amazon river discharge in terms of inducing SSS anomalies in the eastward plume pathway, while river discharge is far dominant in the northwest pathway (V. J. Coles et al., 2013).

Table 6.2: Correlation coefficients (r_{lag}) of plume PCs with PCs of TPA. Only correlations where $|r| \geq 0.25$ are shown. The lag in months for r_{lag} is given in parentheses.

	total precipitation				
	PC1 20.5 %	PC2 16.0 %	PC3 11.0 %	PC4 7.0 %	PC5 4.6 %
PC2 (along-shelf)	−0.29 (0)	0.26 (1)	0.23 (1)	0.10 (0)	0.10 (0)
PC3 (overall spreading)	0.33 (1)	0.15 (0)	−0.25 (0)	0.20 (0)	−0.06 (0)
PC4 (northward spreading)	−0.26 (0)	−0.18 (16)	−0.22 (13)	−0.07 (0)	0.15 (1)

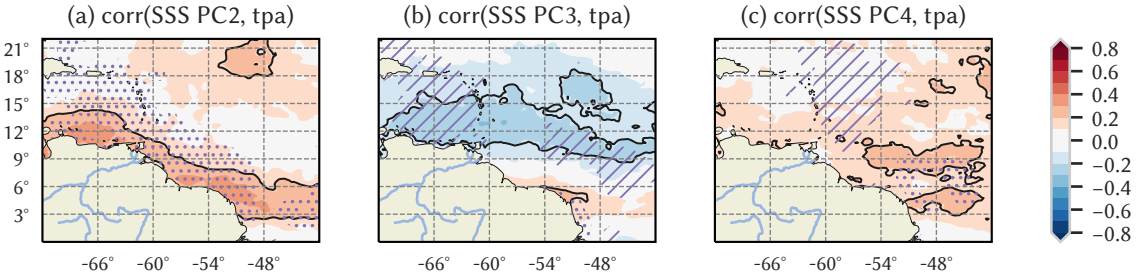

Figure 6.2: Correlation maps showing the correlation coefficient between total precipitation anomaly (TPA) and (a) PC2; (b) PC3 and (c) PC4 of SSS at zero lag. The black contour shows 99.9 % significance. Strong correlations between SSS anomaly data and the respective PCs are shown as purple dotted ($r < -0.3$) and striped ($r > 0.3$) hatching.

Table 6.3: Correlation coefficients (r_{lag}) of plume PCs with PCs of wind speed anomaly. Only correlations where $|r| \geq 0.25$ are shown. The lag in months for r_{lag} is given in parentheses.

	wind speed				
	PC1 60.1 %	PC2 13.0 %	PC3 9.8 %	PC4 3.5 %	PC5 3.0 %
PC2 (along-shelf)	0.16 (13)	−0.26 (0)	0.18 (15)	−0.17 (0)	−0.27 (4)
PC3 (overall spreading)	−0.21 (24)	0.26 (1)	−0.05 (0)	0.19 (14)	0.28 (8)
PC4 (northward spreading)	0.22 (4)	−0.35 (0)	0.00 (0)	−0.20 (1)	0.20 (10)

6.2.3. Wind speed

Strong winds increase mixing. Therefore, we expect that they correlate positively with SSS at zero to one months lag. This would be confirmed by a negative (positive) correlation coefficients of wind speed anomaly with PC2 (PC3 and PC4) of SSS. However, they also increase Ekman transport, which leads to a larger plume surface area, resulting in opposite correlation coefficients.

The first PC of wind speed anomaly describes a large amount (60.1 %) of the total variance, yet no significant correlations are found between this PC and the river plume PCs. As a result, conclusions drawn from the significant correlation coefficients in Table 6.3 are weak. The strongest correlations are found at 0 to 2 months lag.

Correlation maps showing the correlation coefficients between wind speed anomaly and PC2 and PC3 of SSS (Fig. 6.3a and b) confirm a positive association. This means that strong winds in the significant regions in those two figures are related to high salinities in the along-shelf and overall spreading pathways, indicating that these regions respond to wind-induced mixing. The field of negative correlation in Fig. 6.3c shows that strong winds in the blue region are associated with low salinities in the northward spreading region, likely caused by increased Ekman transport leading to the northward propagation of the river plume.

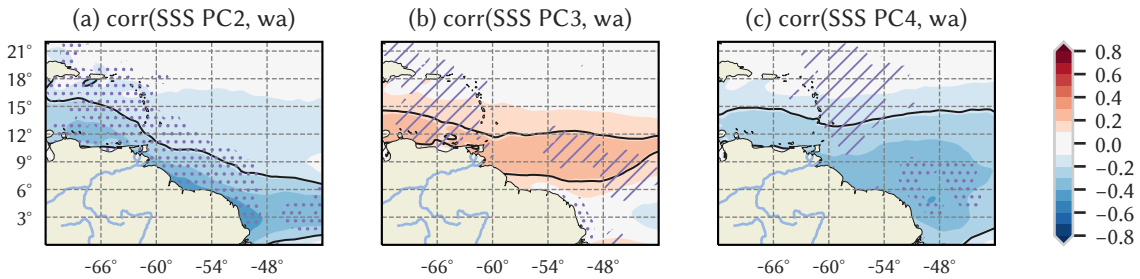

Figure 6.3: Correlation maps showing the correlation coefficient between wind speed anomaly (wa) and (a) PC2; (b) PC3 and (c) PC4 of SSS (no lag). The black contour shows 99.9 % significance. Strong correlations between SSS anomaly data and the respective PCs are shown as purple dotted ($r < -0.3$) and striped ($r > 0.3$) hatching.

6.2.4. Wind direction

The persistent westward trade winds have a seasonally varying north- or southward component. Interannual variations may affect the orientation and spreading of the river plume through the direction of the wind-induced Ekman transport. We expect a greater river plume spreading away from the South-American continent when winds are directed more northward (V. J. Coles et al., 2013; Fournier et al., 2017). This would be confirmed by a positive correlation between wind direction anomaly and PC2, which describes the along-shelf pathway of the river plume, as well as PC4, which describes northward spreading along the Leeward Islands, at a lag of 0 to 3 months. The opposite holds for PC3 of SSS.

Correlation coefficients between river plume PCs and those of wind direction anomalies are weak (Table 6.4).

Table 6.4: Correlations (r_{lag}) of plume PCs with PCs of meridional (N-S) wind speed. Only correlations where $|r| \geq 0.25$ are shown. The lag in months for r_{lag} is given in parentheses.

	meridional wind speed				
	PC1 41.5 %	PC2 29.8 %	PC3 9.7 %	PC4 4.9 %	PC5 3.6 %
PC2 (along-shelf)	0.14 (0)	0.27 (0)	−0.21 (2)	−0.20 (42)	−0.21 (2)
PC3 (overall spreading)	−0.17 (5)	−0.29 (1)	−0.22 (1)	0.03 (0)	0.19 (16)
PC4 (northward spreading)	−0.23 (6)	0.21 (0)	0.34 (0)	−0.03 (0)	0.23 (13)

Maps of the correlation coefficients between wind direction anomaly and PC2 of SSS at a lag of 1 month (Fig. 6.4a) shows almost no significant correlations. Furthermore, Fig. 6.4b shows that northward winds near the amazon river mouth are associated with low salinities in the regions best described by PC3 after 1 month. On the other hand, Fig. 6.4c shows that northward winds east of 54°W are associated with high salinities in the northward plume pathway along the Leeward Islands, the pathway described by EOF4 of SSS.

6.2.5. Vertical wind shear

A high vertical wind shear is associated with reduced genesis and intensification of tropical cyclones. Therefore, we expect that a high wind shear leads to reduced mixing of the water column and thus sustained stratification, presenting as low SSS in the river plume after a lag of 1 to 4 months. This would be confirmed by a positive correlation of vertical wind shear anomaly with PC2 of SSS, and the opposite for PC3 and PC4.

The lag between the two processes, as determined in Table 6.5, is 3 to 5 months. Figure 6.5a and b show that high wind shear south of 12°N is followed by high SSSs in the river plume after 5 months. It is important to note that Tropical Cyclone (TC) generation and intensification

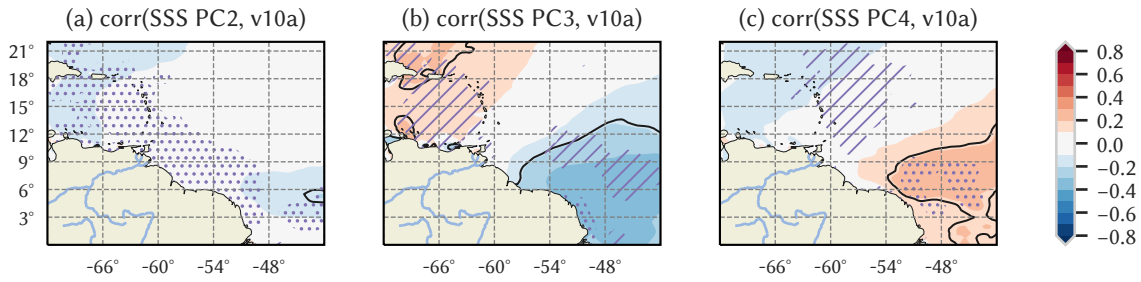

Figure 6.4: Correlation maps showing the correlation coefficient between meridional (N-S) wind speed anomaly (v10a) and (a) PC2; (b) PC3 and (c) PC4 of SSS at 1 month lag. The black contour shows 99.9 % significance. Strong correlations between SSS anomaly data and the respective PCs are shown as purple dotted ($r < -0.3$) and striped ($r > 0.3$) hatching.

Table 6.5: Correlations (r_{lag}) of plume PCs with PCs of vertical wind shear. Only correlations where $|r| \geq 0.25$ are shown. The lag in months for r_{lag} is given in parentheses.

	vertical wind shear				
	PC1	PC2	PC3	PC4	PC5
	48.9 %	28.9 %	7.2 %	4.5 %	3.0 %
PC2 (along-shelf)	0.22 (6)	−0.27 (3)	−0.15 (7)	0.03 (0)	−0.30 (1)
PC3 (overall spreading)	−0.31 (17)	0.31 (5)	0.18 (8)	−0.04 (0)	0.25 (10)
PC4 (northward spreading)	−0.22 (16)	−0.11 (0)	−0.10 (0)	0.03 (0)	0.21 (13)

takes place north of 12°N, which means that wind speed shear anomalies south of 12°N cannot be related to TCs. Figure 6.5c shows no relation between wind shear anomalies and the salinity of the northward plume pathway along the Leeward Islands after 5 months.

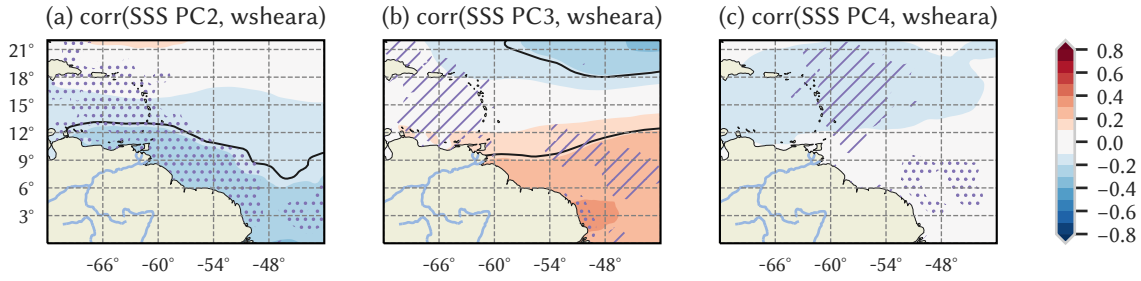

Figure 6.5: Correlation maps showing the correlation coefficient between wind shear anomaly (wsheara) and (a) PC2; (b) PC3 and (c) PC4 of SSS at a lag of 5 months. The black contour shows 99.9 % significance. Strong correlations between SSS anomaly data and the respective PCs are shown as purple dotted ($r < -0.3$) and striped ($r > 0.3$) hatching.

6.2.6. El Nino-Southern Oscillation

An El Niño event results in warm and dry conditions in the Caribbean and over the Amazon basin (Fig. 2.5). This decreases the discharge of both the Amazon and Orinoco Rivers and most likely results in a smaller river plume or higher salinities. Because a positive MEI corresponds to an El Niño event, we expect that the SSS in the river plume is *positively* associated with the MEI (see Section 3.4.1), at a lag of 3 to 6 months. A negative correlation of MEI with PC2 of SSS would confirm this, while the opposite holds for PC3 and PC4.

Conversely, El Niño events also cause high vertical wind shear, with subsequent decrease

Table 6.6: Correlations (r_0 and r_{lag}) of plume PCs with MEI. Only correlations where $|r| \geq 0.25$ are shown. The lag in months for r_{lag} is given in parentheses.

	r_0	r_{lag} (lag)
PC2 (along-shelf)	−0.37	−0.41 (1)
PC3 (overall spreading)	0.29	0.38 (9)
PC4 (northward spreading)	−0.11	0.34 (23)

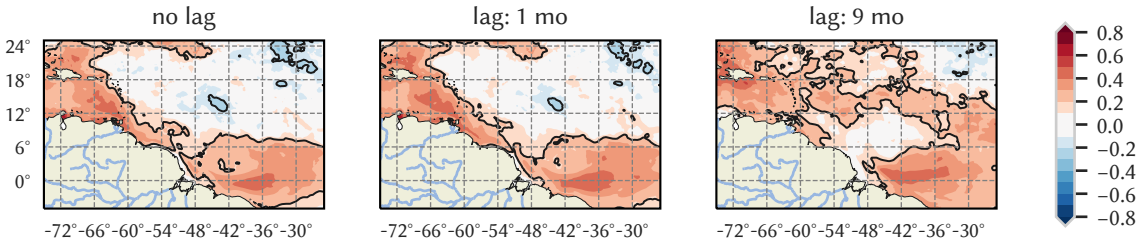

Figure 6.6: Correlation of the Multivariate ENSO Index (MEI) with monthly SSS anomalies at 0, 1 and 9 months lag. The black contour shows 99.9 % significance

in hurricane frequency and -intensity leading to a decrease in vertical mixing. This process suggests that the SSS in the river plume is *negatively* associated with the MEI at zero lag. A positive (negative) correlation of MEI with PC2 (PC3 and PC4) of SSS would confirm this.

Correlation coefficients with the plume PCs are calculated (Table 6.6). The correlation coefficients indicate a positive correlation between MEI and SSS patterns in the regions described by PC2 and PC3 of SSS, indicating that La Niña events are followed by low salinities. This demonstrates that the response to precipitation is dominant over increased TC-induced mixing associated with lower wind shear, which is in line with the results in Sections 6.2.2 and 6.2.5.

The strongest correlations are found at 1 and 9 months lag. Therefore, correlations of MEI with monthly SSS anomalies are calculated at each grid point using 0, 1 and 9 months lag (Fig. 6.6).

A strong positive correlation is found to the east of the Amazon River mouth, where the river plume is not generally found because of its persistent westward orientation. Rather, this is the ITCZ, where the North Brazil Current (NBC) flows in northwest direction along the South-American continent. This indicates that the SSS of the waters entering the area of interest from the southeast are affected by the precipitation which is modulated by the ENSO. A second region of strong correlation is observed in the Caribbean Sea in all three figures. This indicates that a low MEI is followed by negative SSS anomalies in the Caribbean Sea after 1 to 9 months.

6.2.7. Madden-Julian Oscillation

The MJO causes an increase of precipitation in phases 1 and 2, as well as easterly wind anomalies which weaken the westerly trade winds (Martin & Schumacher, 2011). Because of the increased buoyancy input and reduced mixing, lower SSS are expected in these phases. The opposite holds for phases 5 and 6.

The composited SSS anomalies from the annual cycle in July–September show that slightly fresher waters (−0.04 psu) are found in phases 2 and 3 and more saline waters (+0.07 psu) are observed in phases 6 and 7 (Fig. 6.7).

In phase 2 and 3, slightly lower SSSs are observed along the Venezuelan shelf (box 'U' in Fig. 6.8b), possibly caused by reduced upwelling as a result of the weakened trade winds. Furthermore, low salinities are seen at the Orinoco river mouth (box 'O' in Fig. 6.8b). Regions of the expected lower salinity due to an increase in precipitation and reduced mixing are also observed in the Amazon river plume, but they are sparse (box 'A' in Fig. 6.8b). The opposite is found in phase 6 and 7 (Fig. 6.8d). For composite results of each individual phase, see Fig. D.1.

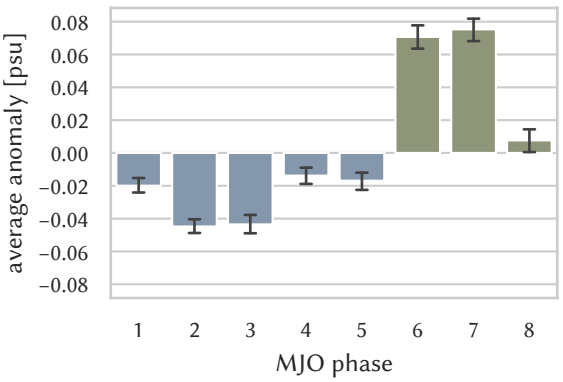

Figure 6.7: Spatial average of daily SSS anomalies from the annual cycle in July–September, composited by phases of the MJO using only strong MJO events (RMM amplitude >1). Averaged over region shown in Fig. 6.8. Error bars show the 99.9 % confidence interval.

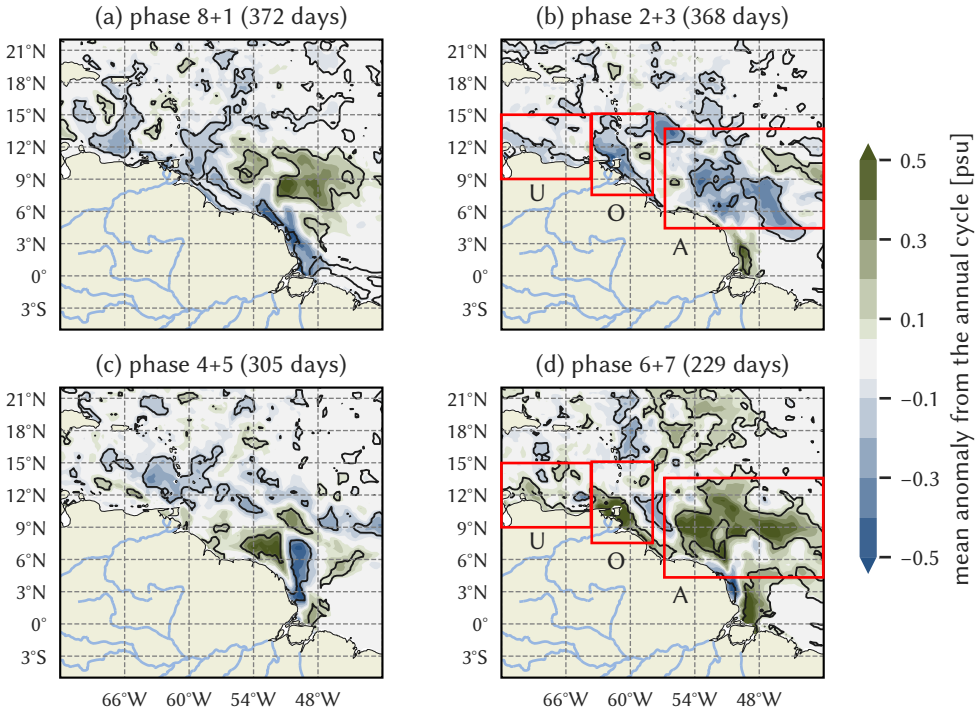

Figure 6.8: Mean of daily SSS anomalies from the annual cycle in July–September, composited by phases of the MJO using only strong MJO events (RMM amplitude >1). The black contours show 99 % significance, based on the local standard deviation determined using a two-tailed t-test. The number of days on which a strong MJO event in the respective phases was present is given in parentheses.

6.3. Conclusion

The impact of oceanic and atmospheric conditions on the river plume was examined using Empirical Orthogonal Function (EOF) analysis combined with correlations analysis. From the correlations analysis, it followed that none of the calculated Spearman rank correlation coefficients were notably higher than the Pearson correlation coefficients, leading us to believe that linear relations are most likely in all cases.

The river plume response to Amazon River discharge anomalies is weak, which is in accordance with previous research (Fournier et al., 2017; Semyon A. Grodsky et al., 2015; Masson & Delecluse, 2001). A small fraction of SSS anomalies east of the Lesser Antilles (60°W) can

Table 6.7: Influence of variables investigated in Section 6.2 on plume-related SSS patterns as determined through EOF analysis (see Fig. 5.6).

	SSS PC2	SSS PC3	SSS PC4
River discharge	○	○	−
Precipitation	−−	−	○
Wind speed	++	+	−
Meridional (N-S) wind speed ↑[+]	○	−−	+
Wind shear	○	−	○
ENSO	++	+	○
MJO phase 2+3	−	−	○
MJO phase 6+7	+	+	○

[+] positive relation to SSS
○ no significant relation to SSS
[−] negative relation to SSS

be explained by anomalous river discharges at a lag of 3 months (Fig. 6.1), but it is likely that other mechanisms are more dominant in modulating the river plume.

Precipitation anomalies correlate with all SSS PCs that were argued to describe the river plume (Table 6.2 and Fig. 6.2), which indicates that some of the variability associated with the SSS response to precipitation is present in those PCs. Therefore, correlations to the plume PCs may also describe feedback mechanisms to precipitation.

On the one hand, strong winds in the WTNA and in the Caribbean Sea are related to a SSS increase in the along-shelf and overall spreading pathways, through enhanced vertical mixing and coastal upwelling. On the other hand, the northward plume extension along the Lesser Antilles, as described by EOF4 of SSS, shows fresh anomalies as a result of increased Ekman transport.

The meridional (N-S) wind speed was used as a measure for wind direction. Strong offshore wind anomalies around the Amazon river mouth and south of 10°N are related to increased northwest spreading of the river plume. Those same wind anomalies are positively correlated to PC4 of SSS at zero lag, which indicates fresher waters in the North Equatorial Counter Current (NECC) but more saline waters in the northward spreading pathway along the Lesser Antilles. Furthermore, a relation between onshore wind anomalies and low SSS is observed in the Caribben Sea west of 60°W, which is likely related to reduced upwelling of deep salty waters along the coast of Venezuela.

Vertical wind shear has a weak positive correlation to the SSS in the river plume with a lag of 5 months. However, the region of strong correlation is located south of 12°N and does not overlap with the region where TCs are generated and intensified, which is north of 12°N. Therefore, those correlations are not related to the generation and intensification of TCs. Other consequences of wind shear variability explaining this significant correlation are outside the scope of this study.

The ENSO is strongly related to SSS anomalies in the river plume region, with low salinities found 1 to 8 months after a La Niña event. This is in part caused by high precipitation, since La Niña events are associated with cool and wet conditions in the Caribbean. La Niña events are also associated with increased tropical storm frequency and -intensity which leads to increased vertical mixing and higher SSS, but this mechanism is outweighed by the increased atmospheric moisture.

When compositing SSS anomalies by phase of the MJO, regions of MJO influence are uncovered. Locally, negative SSS anomalies of up to 0.5 psu are observed in phases 2 and 3, while positive ones are found in phases 6 and 7. In the months following a La Niña event, the combined effect of the ENSO together with a strong MJO event in phase 2 and 3 can induce significant negative anomalies of SSS in the river plume.

7

Sea surface temperatures in the river plume

The previous chapter explored the processes that affect the interannual variability of the Amazon-Orinoco river plume. In this chapter, the consequences of the interannual variability of the Amazon-Orinoco river plume on sea surface temperatures in the Caribbean are investigated. This chapter starts with a description of the research method, followed by a section on the results and, lastly, the conclusions.

7.1. Method

Locally, the presence of the river plume leads to higher sea-surface temperatures (SSTs) through cooling inhibition because of the plume-induced barrier layer. Furthermore, it leads to increased heating due to a higher concentration of coloured matter in the river plume compared to open-ocean waters (see Section 2.1).

Correlation and lag between SSS and SST anomalies

To investigate whether the interannual variability of the river plume has consequences for SSTs in the Caribbean Sea and the Western Tropical North Atlantic (WTNA), correlations between Principal Components (PCs) of SST and sea-surface salinity (SSS) are determined to resolve the lag. Maps are made of correlation coefficients between the plume PCs (defined in Chapter 5) and SST anomalies from the seasonality, which is the same method used in Chapter 6, to identify regions of potential river plume influence.

Comparison of seasonally averaged SSS and SST

To determine whether local SSS anomalies affect SSTs in the same location, seasonal averages are calculated. Correlation maps are made by calculating the correlation coefficients between SST and SSS for the September–October–November (*son*) and June–July–August (*jja*) seasons. A disadvantage of this seasonal averages comparison is that the sample size is much smaller at 25 points (25 years) instead of 300 points in the case of monthly anomalies. Therefore, a less stringent significance criterium is used (95% instead of 99.9%). The advantage of a comparison using seasonal averages is that the river plume and its effects on SSTs are mostly present in only two seasons: *jja* and *son*. The remaining half of the year is neglected. Furthermore, the effect of moving fluid parcels on the correlation is limited.

Relation between annual maximum plume area and anomalous SSTs

To examine the effects of the plume extent on anomalous SSTs, correlation maps are made using the annual maximum plume area as computed in Chapter 5 and seasonally (*jja* and *son*) averaged anomalous SSTs.

7.2. Results

7.2.1. Correlation and lag between patterns of SSS and SST anomalies

Because there is a direct negative relation between SSS and SST on seasonal time scales, we examine whether this effect extends to interannual time scales as well. This should show as a negative relation between SSS and SST at a lag of 0 to 1 months. Correlation coefficients and corresponding lag are computed between Empirical Orthogonal Function (EOF) analysis-derived patterns of anomalous SSS and SST (Table 7.1).

Table 7.1: Correlation coefficients (r_{lag}) of SST PCs with plume PCs. Only correlations where $|r| \geq 0.25$ are shown. The lag in months for r_{lag} is given in parentheses.

	PC2 (along-shelf) 12.6 %	PC3 (overall spreading) 7.8 %	PC4 (northward spreading) 6.0 %
SST PC1	0.26 (12)	−0.27 (17)	0.25 (1)
SST PC2	−0.30 (-1)	0.29 (5)	0.33 (10)
SST PC3	0.23 (-7)	−0.27 (-5)	−0.26 (15)
SST PC4	0.20 (-5)	−0.22 (51)	−0.28 (21)
SST PC5	0.22 (0)	−0.19 (9)	−0.24 (22)

The majority of the correlations in Table 7.1 is weak, or is strongest at a lag of more than 11 months and thus neglected. This provides little support for the hypothesis of a 0–1 month lagged relationship between SST and SSS. The moderately strong correlation between SSS PC4 and SST PC2 at 10 months lag could indicate that heated plume waters stay in the region north-east of the Leeward Caribbean Islands and pre-heat the sea surface, leading to higher temperatures in the following year.

Figure 7.1 shows correlation maps of SST anomalies with the plume PCs. SSS PC2 describes the salinity variability in the along-shelf pathway of the river plume, and shows a weak correlation to SST anomalies in the same region ($r < 0.4$, $p < 0.001$). This indicates that SSTs in this region are anomalously high when the river plume is relatively fresh. SSS PC3 describes the salinity variability in the Caribbean Sea and in the greater WTNA, but shows a minor region of significant correlation to anomalous temperatures. Lastly, SSS PC4 describes the northward pathway of the river plume along the Lesser Antilles. This pathway correlates positively with anomalous SSTs in the WTNA ($0.2 < r < 0.32$, $p < 0.001$), indicating that high temperatures are found in the red region shown in Fig. 7.1c when salinities east of the Lesser Antilles are low.

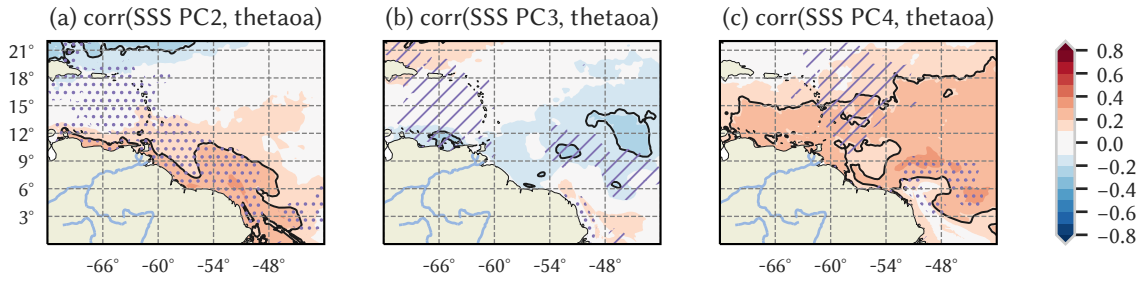

Figure 7.1: Correlation maps showing the correlation coefficient between SST anomaly and (a) PC2; (b) PC3 and (c) PC4 of SSS at zero lag. The black contour shows 99.9 % significance.

7.2.2. Comparison of seasonally averaged SSS and SST

In the correlation maps in Fig. 7.2, the expected negative association between SST and SSS is locally apparent in both the *jja* and *son* seasons. In *jja*, the regions of negative correlation follow the mean river plume shape just outside the river mouth, but not into the Caribbean Sea. However, along the northeast edge of the largest river plumes, defined as the 35.4 psu contour

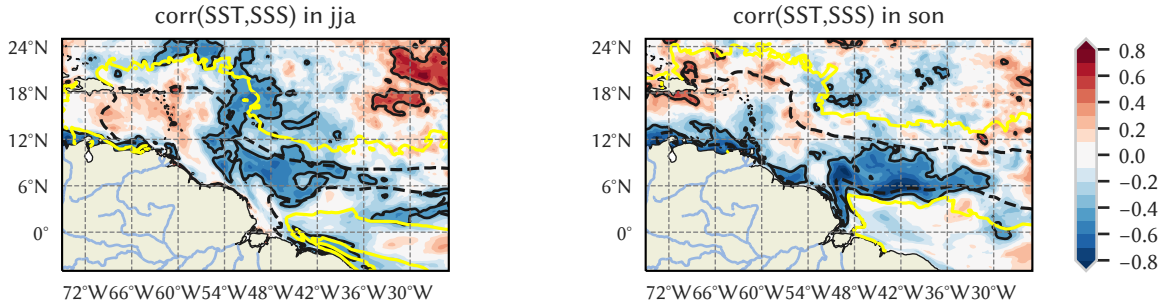

(a) (b)

Figure 7.2: Map of correlation coefficients between SST and SSS anomalies for the *jja* and *son* seasons. The black solid contours indicate the 95 % significance level. The black dashed contour gives the mean SSS = 35.4 psu in the respective seasons. The yellow contour is the 35.4 psu contour of the 1993–2017 minimum of seasonally averaged SSS.

of the minimum seasonally averaged SSS (yellow contour in Fig. 7.2), significant negative correlations are apparent. This indicates that anomalous northeast plume advection transports heat further away from the mean river plume as well. These combined results indicate that lower SSS does not directly increase SST, but rather extensive plume advection – characterised by fresh anomalies along the plume edge – are related to SST anomalies along that plume edge as well.

In *son*, the strong negative correlations around 42°W and 6°N follow the eastward retroflection pathway and can thus be attributed to the river plume. However, this negative association is not found in the westward pathway into the Caribbean Sea. Furthermore, the negative correlations along the South-American shelf around Venezuela (66°W) are more likely to be related to coastal upwelling, as upwelling transports subsurface waters to the surface and these are characterised by low temperature and high salinity which results in a negative correlation between the two.

7.2.3. Relation between annual maximum plume area and anomalous SSTs

The annual maximum plume area shows no correlation with anomalous SSTs in the Caribbean Sea in both *jja* and *son* (Fig. 7.3). This shows that there is no significant relation between the interannual variability of the plume extent and of SSTs in the Caribbean. This provides no support for the hypothesis that SST in the region are increased due to more extensive spreading of the river plume. To the contrary, the SST north of 18°N are negatively affected by a large annual maximum plume area.

Figure 7.4a shows more compelling results, with a strong positive correlation between the annual maximum plume area and anomalous SST in the WTNA and the Caribbean Sea in *jja* ($0.4 < r < 0.6$, $p < 0.05$). A much smaller region of strong positve correlation is also seen in *son* along the continental shelf (Fig. 7.4b). Additionally, a region of negative correlation is observed north of 18°N. This could indicate that high SSTs are found in the WTNA, one year after a relatively large river plume is observed. It also shows that the location of these high temperatures could be affected by the extent of the river plume.

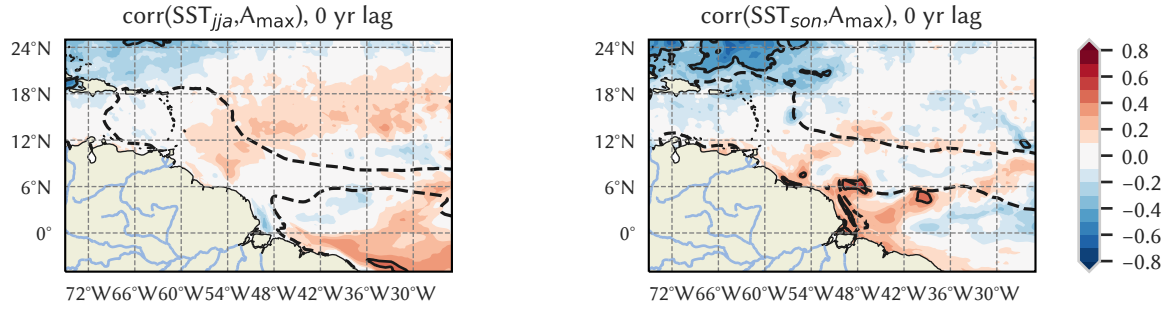

(a) (b)

Figure 7.3: Map of correlation coefficients between the annual maximum plume area and SST anomalies in the (a) *jja* and (b) *son* seasons. The black solid contour gives the 95 % significance level. The black dashed contour gives the mean SSS = 35.4 psu in the respective seasons.

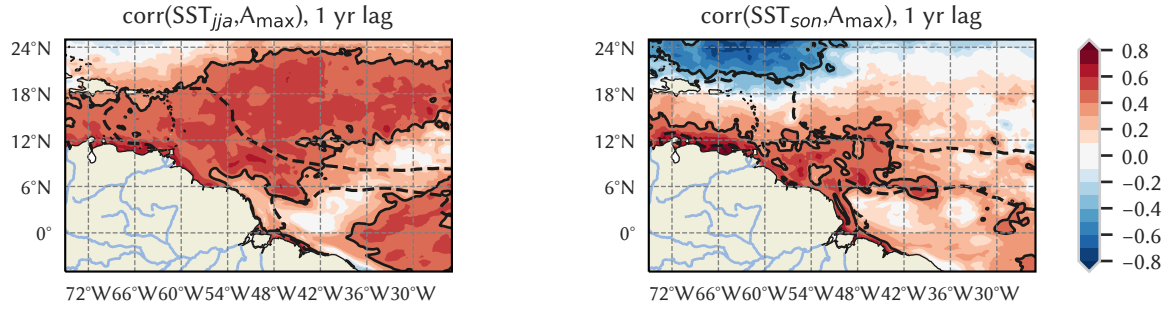

(a) (b)

Figure 7.4: Same as Fig. 7.3, but correlation coefficients calculated using maximum plume area in the previous year.

7.3. Conclusion

In this chapter, the relation between the interannual variability of the river plume and SSTs was investigated. Results do not support the hypothesis that anomalous SST in the Caribbean are higher when plume-related SSS patterns are relatively fresh. Conversely, SSSs anomalies in the northward pathway of the river plume along the Leeward Islands shows a positive correlation with anomalous SSTs in the WTNA (Fig. 7.1c). On the other hand, even significant correlations shown in Fig. 7.1c are weak (r < 0.4).

When comparing local anomalies of SSSs to those of SST by in the *jja* and *son* seasons, the expected negative correlations are present (Fig. 7.2). The negative correlation field is located where the eastward retroflection current is found, indicating that negative SSS anomalies are associated with anomalous high SST in the river plume around 42°W. However, the expected negative correlations are not found in the westward pathway of the river plume and in the Caribbean Sea. This indicates that negative SSS anomalies in the Caribbean Sea do not lead to anomalous high SSTs.

A relatively large annual maximum plume extent also shows no significant correlation with SST in *jja* and *son* (Fig. 7.3), reinforcing the conclusion that low SSS advected far from the river mouth do not lead to anomalously high SST in the same year. However, in a year following a large river plume, high salinities are observed in the entire WTNA and in the Caribbean Sea in *jja* (Fig. 7.4a). In *son*, this same relation is visible south of 18°N, while the negative correlation north of 18°N indicates that a large river plume is followed by low SST in that region after one year (Fig. 7.4b).

8

Discussion

This chapter provides a reflection on the study as a whole, including its limitations and related recommendations for further research. Therefore, this chapter is separated into three sections, of which Section 8.1 contains a general reflection on the data and methodology used. The last two sections correspond to the two main objectives of this study, which are to assess the modulators of the interannual variability of the Amazon-Orinoco river plume (Section 8.2), and to investigate its consequences on sea-surface temperatures (SSTs) in the Western Tropical North Atlantic (WTNA) and the Caribbean Sea (Section 8.3).

8.1. Data and methodology

8.1.1. Applicability of model reanalysis data

For the analyses performed in this thesis, 25 years of daily and monthly model reanalysis data from 1993 to 2017 was used. While this time range is slightly less than the 30-year climate scale, it does span more than three times the El Niño-Southern Oscillation (ENSO) time scale of 2–8 years and is therefore large enough to include the main interannual plume variability. However, atmospheric variability associated with the Atlantic Multidecadal Oscillation (AMO) is not included in this study. This oscillation affects rainfall over the Amazon and Orinoco basins, rainfall and hurricane activity over the WTNA and the meridional position of the Intertropical Convergence Zone (ITCZ) (Knight, Folland & Scaife, 2006), which all influence the river plume. Therefore, it should be included in further studies to better understand plume variability.

Although the Global Ocean Physical Reanalysis Product (GLORYS12V1) model reanalysis data is assimilated with both in-situ and satellite observations, it is still subject to model error. We assessed the temporal and spatial resemblance of the simulation to satellite measurements and concluded that the temporal and spatial temperature and salinity structure are well-represented in the model (Figs. 3.1 and 3.2). The quality of the assimilated simulation improves significantly after the deployment of Argo floats (~2002–2007), but only satellite measurements can map the large-scale horizontal sea-surface salinity (SSS) and SST structures associated with the river plume. However, satellite observations of SSS are only available from 2010 onwards, leaving 18 years unaccounted for. Still, this model reanalysis allows to analyse the interannual variability of the river plume at a far larger time scale than has been done in previous studies using only satellite observations (Fournier et al., 2017; Semyon A. Grodsky et al., 2015; Semyon A Grodsky et al., 2014).

8.1.2. Definition of the river plume

Two methods were used to describe the river plume. First, a simple SSS threshold was used to compute the surface area, volume and thickness of the river plume. Second, an Empirical Orthogonal Function (EOF) analysis was performed to uncover dominant modes of SSS variability. Here, we comment on their applicability.

SSS threshold

The river plume surface area was used to assess the variability of the plume extent as bound by the 35.4 psu isohaline, the same threshold as Ffield (2007) and similar to the threshold used in other studies investigating the river plume at large spatial scales (V. J. Coles et al., 2013; Fournier et al., 2017; Lentz & Limeburner, 1995; Zeng et al., 2008). While this is a widely used approach, it is important to note that the choice of the SSS threshold affects the size, thickness, volume and of the river plume. In other words, choosing a threshold of 34 psu would lead to a smaller maximum plume volume, occurring earlier in the year. Furthermore, the SSS threshold approach comes with a major disadvantage: it does not distinguish between the responses to riverine freshwater input and precipitation. Although riverine influence on SSS is dominant over precipitation in the northwest plume pathway, especially from March to August when the plume is increasing in size (V. J. Coles et al., 2013), the effects of precipitation variability related to the meridional position of the ITCZ on SSSs are non-negligible. That said, a SSS threshold does allow to assess the modulators and consequences of the buoyant freshwater lens resulting from the combined effect of both river runoff and precipitation. Since colored dissolved organic matter (CDOM) dominates the water colour in the river plume rather than Chlorophyll, it performs well in distinguishing the plume waters from open-ocean waters up to thousands of kilometres from the river mouths (Hu et al., 2004; Molleri et al., 2010). It is recommended that the plume be differentiated using a defining characteristic which includes CDOM in addition to SSS in future research.

EOF analysis

The second, third and fourth Principal Component (PC) of SSS as anomaly from the seasonality were used as a measure for river plume variability. These PCs combined with their corresponding EOFs describe spatio-temporal patterns of SSS variability, but one should be careful not to interpret them as physical modes of variability. Nevertheless, we assume that these three PCs describe distinct elements of the westward pathway of the river plume, based on their correlation with the river plume surface area and the resemblance of their spatial patterns to previously found main pathways and dispersion patterns of the river plume (V. J. Coles et al., 2013; Molleri et al., 2010). It is important to note the three main limitations of this assumption.

First of all, the river plume is subject to a wide range of processes modifying local SSSs, including eddy-driven transport (Fournier et al., 2017) and Tropical Cyclone (TC)-induced vertical mixing (i.e. Semyon A Grodsky et al., 2012), making dominant modes of interannual variability difficult to describe using EOF analysis. As a result, the three selected plume PCs describe only 26.4 % of the total SSS variance in the 0°–22°N, 72°W–42°W region. Because of the large interannual variability of freshwater deposited in the WTNA by the Amazon River as well as atmospheric and hydrodynamic processes modulating the river plume, it is likely that the river plume accounts for a larger percentage of the total SSS variance than can be captured in just these three PCs. However, since the selected PCs do capture the main structure of the river plume (see Appendix E), results give an indication of its dependence on the investigated mechanisms.

Second, all months of the year are included in the EOF analysis, while the river plume is distinctly present in half of the year (June–November) but almost negligible in March–May. SSS anomalies in those months are much less likely to be related to the river plume, and can affect correlation coefficients. Then again, using all months of the year allowed us to estimate the most probable lag between a modulator and the river plume response. Using this knowledge, the next step is to assess the river plume variability using seasonal averages.

Lastly, the combination of EOFs are informative in relation to the river plume shape, but their assessment is complex and, as they do not necessarily correspond to physical modes of variability, they cannot stand on their own. Therefore, it is recommended to include a river plume shape parameter in further analyses, as has previously been done by Molleri et al. (2010) who make use of a Plume Shape Index based on the outer contour of the river plume in identifying mechanisms which modulate the seasonal variability of the river plume. However, it should first be assessed whether such a metric is suitable for distinguishing the far more subtle interannual differences.

8.1.3. Cross-correlations with principal components

The approach used in this study to quantify the effects of atmospheric processes on river plume variability was to calculate cross correlations between the principal component time series of SSS and the relevant atmospheric process. This provided insight into spatial influence patterns as well as the lag of the response. Computed correlation coefficients were all moderately weak, which is common for this approach: Murtugudde, Ballabrera-Poy, Beauchamp and Busalacchi (2001) presents both similar and slightly stronger results, while using data filtered through a 3-month running mean. A more widely used approach is to utilize multivariate EOF analysis to uncover co-variability of multiple phenomena (e.g. Semyon A. Grodsky, Reul, Chapron, Carton & Bryan, 2017; Murtugudde et al., 2001). Using this approach did not lead to more coherent results in this study (not shown), but may be looked into in future studies.

8.2. Variability of the river plume

8.2.1. Variability of river plume extent

The large interannual variability of the annual minimum plume area and -volume (Fig. 5.4) indicates a considerable interannual variability of both the horizontal and vertical entrainment rate of saline waters. This implies that in a year following a large annual minimum river plume, the background salinity in the mixed layer may be reduced. V. J. Coles et al. (2013) found that the river plume contains both recent Amazon discharge and discharge from the previous year, supporting this theory.

Because the SSS threshold does not allow to distinguish the origin of fresh waters, it is possible that the high annual minima of plume extent are caused by extreme precipitation in February–March. The ITCZ is located between 4°S–4°N in these months, its southernmost position (Chiang, Kushnir & Giannini, 2002). Since the plume area in this thesis is computed using the 0°–22°N latitudinal range, it is possible that computed plume area anomalies are caused by local precipitation. However, inspection of the plume shape at times of minimum plume area reveal that this is not the case.

8.2.2. Modulators of interannual river plume variability

River discharge

The influence of interannual Amazon River discharge variations on the dispersion and characteristics of the river plume is debated. Zeng et al. (2008) show a strong interannual anomaly correlation (r = 0.58) with the plume extent, as bound by the 34.7 psu isohaline, in 1997-2004. Conversely, other studies suggest that there is no significant relation at all, instead arguing that atmospheric forcing is far dominant (Fournier et al., 2017; Semyon A. Grodsky et al., 2015; Masson & Delecluse, 2001). Our results show weak evidence of a local modulation of SSS due to Amazon River discharge anomalies east of the Lesser Antilles (Fig. 6.1; $0.20 < r < 0.32$, $p < 0.001$). Since local precipitation anomalies do not show significant correlation in this same region (Fig. 6.2c), the correlation is likely the result of riverine fresh waters advected northward over the course of three months rather than local freshening of surface waters due to precipitation.

The results did not indicate any influence of the interannual variability of the Orinoco River discharge on the plume salinity patterns. It is likely that the magnitude of its variability is simply too small (see Fig. 2.2) to significantly affect plume characteristics. However, it should be noted that the area of interest is cut off at 72°W, while the combined Amazon-Orinoco river plume affects the region west of that boundary as well. Since the Orinoco River mouth is located relatively close to that boundary, it is possible that plume characteristics west of the region of interest are affected by the interannual variability of the Orinoco River.

Precipitation

Part of the moderately strong correlations of precipitation with interannual SSS variability (Table 6.2 and Fig. 6.2) can be explained by local precipitation-induced freshening of the ocean surface. However, it is likely that other atmospheric processes that are associated with anom-

alous precipitation also influence plume dynamics. The meridional migration of the ITCZ, which is characterized by a zonal band of high precipitation, influences wind direction and -strength, which affects wind-driven plume advection as well (V. J. Coles et al., 2013). The computed lag of 0–1 months associated with the correlations is reasonable for both response mechanisms, such that the lag can not be used to argue which is dominant. In further research, the direct freshening due to local precipitation can be minimized by using the previously recommended method of plume differentiation which includes CDOM in addition to SSS.

Wind forcing

Weak onshore winds along the South-American continent south of 10°N are associated with enhanced off-shore spreading of the river plume after 0–1 months (Fig. 6.3c and Fig. 6.4b), which is in line with previous studies (V. J. Coles et al., 2013; Fournier et al., 2017). However, results also show that strong winds over the plume region are related to higher SSS along the shelf (Fig. 6.3a), likely caused by a combination of coastal upwelling of deep saline waters and wind stress-induced vertical mixing.

Wind shear was used as an indicator for TC generation and intensification. Although wind shear south of 12°N does correlate significantly with the plume salinity patterns, this is not related to TCs as these are generated and intensified north of that latitude. The possible relation between SSS- and wind shear anomalies south of 12°N is outside the scope of this thesis.

Teleconnections

ENSO A La Niña event is associated with a cool, wet atmosphere over the Caribbean Sea and the Amazon basin and strong winds over the entire WTNA (Klotzbach, 2011; Malmgren et al., 1998; Marengo & Espinoza, 2016; NOAA National Weather Services, 2016) Results show a positive correlation between the Multivariate ENSO Index (MEI) and SSS in the Caribbean Sea after 1–9 months (Fig. 6.6), which implies that low salinities are found in that region some months after a La Niña event. The correlation is strongest along the South American shelf, in the Caribbean Sea and in the ITCZ. It is possible that this strong correlation is caused by a combination of high precipitation, as results showed that this is associated with low SSS, and strong onshore winds, pinning the river plume against the coastal shelf. On the other hand, this is inconsistent with other results showing that strong winds over the plume region are related to high SSS along the shelf and to low SSS in the northward spreading region. Because of the complexity of the ENSO impacts, no concrete conclusions can be drawn from the results presented in this thesis alone. More research is necessary to determine what ENSO-dependent mechanisms cause this positive correlation.

MJO Resulting from the increased precipitation in phases 1 and 2 of the Madden-Julian Oscillation (MJO) (Martin & Schumacher, 2011), slightly lower than usual SSS was found in phases 2 and 3 (Fig. 6.7) with local anomalies of up to 0.5 psu (Fig. 6.8). Regions in which these strong anomalies were found were sparsely spread over the region of interest, so further research is needed to investigate the particular mechanisms causing this scattered response.

The precipitation anomalies were associated with decreased strength of the trade winds, so it is possible that wind-driven vertical mixing is reduced in phases 1 and 2, which helps to maintain the fresh water lens and enhances the fresh SSS anomalies. However, this mechanism cannot be concluded from the results in this thesis alone and should be assessed in further research.

8.3. Consequences of river plume variability on SST

The Amazon-Orinoco river plume has far-reaching effects on the entire Caribbean region, one of which is its association with temperatures that are up to 1.5 °C higher than in open-ocean waters (Hu et al., 2004). While prior research has been conducted on the variations of river plume dynamics on seasonal timescales (e.g. V. J. Coles et al., 2013), this study focused on the relationship between the interannual river plume variability and abnormally high sea surface temperatures in the Caribbean Sea.

The results shown in Fig. 4.4 are consistent with previous studies in that sea surface temperatures in the river plume are significantly higher than in the open-ocean in boreal summer months (Ffield, 2007; Hu et al., 2004). However, the interannual variability of SSS are only slightly related to the magnitude of extreme SSTs in the northwest pathway of the river plume (Fig. 7.2). A significant negative correlation is found along the northeast edge of the largest river plumes (Fig. 7.2), indicating that anomalous northeast-directed plume advection is related to anomalous high SST in that region. These results are in line with conclusions of (Fournier et al., 2017), who note the lack of a strong statistical relation between interannual SST and SSS variability, but show a strong similarity in the location of horizontal SST and SSS gradients.

The lack of significant positive correlation between annual maximum plume surface area and seasonally averaged SST anomalies (Fig. 7.3) further show that an extensive river plume is not necessarily related to high SST. Rather, this reinforces the notion that not the size of the plume but the direction in which the plume spreads is governing in explaining SST anomalies.

Additionally, significant negative correlations are found in the retroflection region (48°W, 8°N) and the North Equatorial Counter Current (NECC) in the June–July–August (*jja*) season, which is even stronger in September–October–November (*son*). As the focus of this thesis is on the northwest pathway of the river plume, reasons for this negative correlations are not investigated and may be a topic for further research.

Since computed lagged correlations presented evidence of a 10-month delayed relation between SST- and SSS anomalies (Table 7.1), correlation maps were made of seasonally averaged anomalous SST and maximum plume surface area in the preceding year. The results show a strong positive correlation ($0.4 < r < 0.6$, $n = 24$, $p < 0.05$) in the entire WTNA and the Caribbean Sea in *jja* (Fig. 7.4a), indicating that SST are high in the summer following a year with a larger-than-usual river plume. Since the river plume is a mixture of recent and up to 1-year aged riverine waters (V. J. Coles et al., 2013), so it is possible that riverine waters remain in the region for a long period of time, together with its contained heat and CDOM, pre-heating the WTNA mixed layer in the following year. This would be in line with the large variability of annual minimum plume area and -volume Figs. 5.4a and 5.4c. It is recommended that the origins of the spring WTNA waters are further investigated using backward Lagrangian parcel tracking.

In *son*, the region of strong positive correlations along the South American shelf west of 48°W is less extensive than that in *jja*. Furthermore, significant negative correlations are found north of 18°N and west of 48°W, which indicate that SSTs in that region are low in a year following a large river plume. Since TCs are intensified by warmer plume temperatures (Ffield, 2007) and the *son* season follows the height of the hurricane season which ranges from July–October, it is possible that these negative anomalies are caused by the cool wakes of intense TCs crossing the northern part of the river plume. In support of this theory are results of Androulidakis et al. (2016), who find that the plume area (defined as SSS <35.6 psu) reduces significantly due to hurricane-induced vertical mixing of cool waters. More in-depth assessment of the cause of these negative anomalies may be an interesting topic for future research.

9

Conclusions and recommendations

The study aims to provide a better understanding of the interannual variability of the Amazon-Orinoco river plume, to help explain why sea-surface temperatures (SSTs) in the Caribbean rise to destructive levels resulting in coral bleaching and -mortality in some years. To this end, an extensive account of the results and their implications was given in the discussion chapter. Here, we concisely present the main takeaways of this thesis, including answers to the research questions, main limitations and recommendations for further research.

9.1. Conclusions

The conclusions of this study are presented by first answering the research subquestions and subsequently stating the overall conclusion by answering the main research question.

1. *What are the defining characteristics of the Amazon-Orinoco river plume?*

   The river plume was defined using a salinity threshold of 35.4 psu. While this approach does not distinguish between river discharge- and precipitation-induced fresh water, it does allow to assess the modulators and consequences of the buoyant freshwater lens resulting from their combined influence.

2. *How does the Amazon-Orinoco river plume vary interannually?*

   Large interannual variations of plume area, -volume and -thickness were found, reinforcing that the interannual variability of the river plume may impact hydrodynamic processes in the Western Tropical North Atlantic (WTNA) and the Caribbean Sea. The variability of annual minimum plume area is especially noteworthy, with a range of $0.4 \times 10^6\,\mathrm{km}^2$ to $1.5 \times 10^6\,\mathrm{km}^2$ in the years of highest contrast, demonstrating the immense variability of the freshwater volume remaining in the region at the end of a plume cycle.

   An Empirical Orthogonal Function (EOF) analysis was performed to uncover the dominant patterns of sea-surface salinity (SSS) variability, followed by a correlations analysis assessing their relation to the river plume. Three Principal Components (PCs) were found descriptive of main plume patterns of interannual variability, and were subsequently used to assess river plume modulators.

3. *What processes affect the interannual variability of the Amazon-Orinoco river plume?*

   Plume behaviour is modulated by a complex range of processes, with spatial variations in the hydrodynamic response to forcing as a result of the immense plume surface area. It is dominated by wind-induced advective transport and -mixing. Results suggest a relation between north-directed wind anomalies and extensive spreading of the low-salinity plume waters. Furthermore, strong winds over the along-shelf plume region are related to locally increased SSS, likely due to a combination of coastal upwelling of deep saline waters and wind-induced vertical mixing.

Furthermore, local precipitation highs may play an important role in modulating interannual SSS variations.

Additionally, while prior research has indicated no modulation of plume characteristics, we found weak evidence suggesting local influence of interannual Amazon River discharge variability on SSS east of the Lesser Antilles after a lag of three months.

Through its modulation of the above-mentioned atmospheric processes, there is a strong indication that the El Niño-Southern Oscillation (ENSO) affects SSS variability in the main along-shelf northwest plume pathway, with low SSS found 1–9 months after a La Niña event. However, the relation to the northward spreading pathway of the river plume is much weaker.

Lastly, SSS are slightly affected by the Madden-Julian Oscillation (MJO), with fresh anomalies of up to 0.5 psu found on days with strong phase 2 and 3 MJO events, following previously found high precipitation anomalies in phases 1 and 2. The opposite is found for phase 6 and 7.

Finally, we can answer the main research question:

> *What are the consequences of the interannual variability of the Amazon-Orinoco river plume on sea surface temperatures in the Caribbean Sea and the WTNA?*

Results show evidence of a slight direct effect of the river plume on anomalous SSTs in case of extensive northeast plume advection, with higher-than-usual temperatures found in the case of anomalously low SSS. In this, we show that not the size of the plume, but rather the direction in which it spreads is governing in explaining SST anomalies.

Moreover, evidence is presented of a relation between high summer SST and a large annual maximum plume area in the preceding year, which may indicate that large river plumes have the ability to pre-heat the mixed layer in the WTNA. However, this mechanism cannot directly be concluded from the findings in this thesis, and should be addressed in further studies.

All in all, this study further builds onto the understanding of the interannual variability of the Amazon-Orinoco river plume, by utilizing a 25-year model reanalysis record of daily and monthly atmospheric and oceanic parameters. Firstly, it shows that the ENSO plays an important role in modulating plume characteristics, which emphasises the importance of long time scales in understanding river plume behaviour. Secondly, although it is not dominant, interannual variability of the Amazon River discharge may be more important than has previously been assumed based on satellite SSS records, which necessarily span far shorter time scales. Lastly, we propose a one-year lagged influence of the most extensive river plumes on SST anomalies in the WTNA, which may help in the prediction of coral bleaching events.

9.2. Recommendations

In the discussion in Chapter 8, limitations of this study are presented together with some recommendations. The most important recommendations for further research are given here.

Plume definition The characteristics and interannual variability of the river plume were determined using its SSS signature only. Since this method does not allow to distinguish between river discharge- and precipitation-induced SSS anomalies, it is recommended to use a defining characteristic which includes colored dissolved organic matter (CDOM) in addition to SSS in future research.

Delayed relation between river plume extent and anomalous SSS This study clearly demonstrates a significant lagged correlation between plume area and increased SSS, but further research is necessary to determine whether this is indeed caused by lingering plume waters. Using Lagrangian parcel back-tracking is recommended to determine whether warm anomalies in June–July–August (*jja*) result from lingering plume waters discharged in the preceding year.

Effects of the Madden-Julian Oscillation on river plume variability Preliminary results were presented indicating a modulation of SSSs by the MJO. It is possible that this is merely the SSS response to precipitation. However, it could also be the response to reduced wind-driven vertical mixing, which helps to maintain the fresh water lens and enhances fresh SSS anomalies. The mechanism causing the fresh anomalies cannot be concluded from the results in this thesis alone and should be assessed in further research.

Persistence of SST anomalies Since corals reefs are especially sensitive persistent high SST, the duration of their exposure to heated waters is an important factor to consider. The influence of the river plume on the persistence of high SST should be investigated to better predict coral bleaching events.

Bibliography

Androulidakis, Y., Kourafalou, V., Halliwell, G., Le Hénaff, M., Kang, H., Mehari, M. & Atlas, R. (2016). Hurricane interaction with the upper ocean in the Amazon-Orinoco plume region. *Ocean Dynamics*, *66*(12), 1559–1588. doi:10.1007/s10236-016-0997-0

Baird, A. & Marshall, P. (2002). Mortality, growth and reproduction in scleractinian corals following bleaching on the great barrier reef. *Marine Ecology Progress Series*, *237*, 133–141.

Balaguru, K., Chang, P., Saravanan, R., Leung, L. R., Xu, Z., Li, M. & Hsieh, J.-S. (2012). Ocean barrier layers' effect on tropical cyclone intensification. *Proceedings of the National Academy of Sciences*, *109*(36), 14343–14347.

Baumgartner, A. & Reichel, E. (1975). *The world water balance: Mean annual global, continental and maritime precipitation and run-off*. Elsevier.

Bender, M. A. & Ginis, I. (2000). Real-Case Simulations of Hurricane–Ocean Interaction Using A High-Resolution Coupled Model: Effects on Hurricane Intensity. *Monthly Weather Review*, *128*(4), 917–946. doi:10.1175/1520-0493(2000)128<0917:RCSOHO>2.0.CO;2

Boutin, J., Martin, N., Reverdin, G., Yin, X. & Gaillard, F. (2013). Sea surface freshening inferred from smos and argo salinity: Impact of rain. *Ocean Science*, *9*(1).

Boutin, J., Vergely, J.-L. & Khvorostyanov, D. (2018). *SMOS SSS L3 maps generated by CATDS CEC LOCEAN* [Debias v4.0]. doi:10.17882/52804

Chérubin, L. & Richardson, P. L. (2007). Caribbean current variability and the influence of the Amazon and Orinoco freshwater plumes. *Deep Sea Research Part I: Oceanographic Research Papers*, *54*(9), 1451–1473.

Chiang, J. C. H., Kushnir, Y. & Giannini, A. (2002). Deconstructing Atlantic Intertropical Convergence Zone variability: Influence of the local cross-equatorial sea surface temperature gradient and remote forcing from the eastern equatorial Pacific. *Journal of Geophysical Research: Atmospheres*, *107*(D1), ACL 3-1-ACL 3–19. doi:10.1029/2000JD000307

Coles, S. L. & Jokiel, P. L. (1978). Synergistic effects of temperature, salinity and light on the hermatypic coral montipora verrucosa. *Marine Biology*, *49*(3), 187–195.

Coles, V. J., Brooks, M. T., Hopkins, J., Stukel, M. R., Yager, P. L. & Hood, R. R. (2013). The pathways and properties of the Amazon River Plume in the tropical North Atlantic Ocean. *Journal of Geophysical Research: Oceans*, *118*(12), 6894–6913.

Copernicus Climate Change Service (C3S). (2017). ERA5: Fifth generation of ECMWF atmospheric reanalyses of the global climate. Copernicus Climate Change Service Climate Data Store (CDS). Retrieved January 13, 2020, from https://cds.climate.copernicus.eu/cdsapp#!/home

Curtin, T. B. & Legeckis, R. V. (1986). Physical observations in the plume region of the Amazon River during peak discharge — I. Surface variability. *Continental Shelf Research*, *6*(1-2), 31–51.

Dai, A. (2017). *Dai and Trenberth Global River Flow and Continental Discharge Dataset*. Boulder CO: Research Data Archive at the National Center for Atmospheric Research, Computational and Information Systems Laboratory. Retrieved November 5, 2018, from https://doi.org/10.5065/D6V69H1T

Dai, A., Trenberth, K. E. & Karl, T. R. (1998). Global variations in droughts and wet spells: 1900–1995. *Geophysical Research Letters*, *25*(17), 3367–3370.

Dawson, A. (2016). Eofs: A library for eof analysis of meteorological, oceanographic, and climate data. *Journal of Open Research Software*, *4*(1).

de Boyer Montégut, C., Mignot, J., Lazar, A. & Cravatte, S. (2007). Control of salinity on the mixed layer depth in the world ocean: 1. general description. *Journal of Geophysical Research: Oceans*, *112*(C6). doi:10.1029/2006JC003953

E. U. Copernicus Marine Environment Monitoring Service. (2018). GLORYS12V1 product. Retrieved January 14, 2020, from http://marine.copernicus.eu/services-portfolio/access-to-products/?option=com_csw&view=details&product_id=GLOBAL_REANALYSIS_PHY_001_030

Ferreira, R. N., Schubert, W. H. & Hack, J. J. (1996). Dynamical aspects of twin tropical cyclones associated with the madden–julian oscillation. *Journal of the atmospheric sciences*, *53*(7), 929–945.

Ffield, A. (2005). North brazil current rings viewed by trmm microwave imager sst and the influence of the amazon plume. *Deep Sea Research Part I: Oceanographic Research Papers*, *52*(1), 137–160.

Ffield, A. (2007). Amazon and orinoco river plumes and nbc rings: Bystanders or participants in hurricane events? *Journal of climate*, *20*(2), 316–333.

Fitt, W. & Warner, M. (1995). Bleaching patterns of four species of caribbean reef corals. *The Biological Bulletin*, *189*(3), 298–307.

Flagg, C. N., Gordon, R. L. & McDowell, S. (1986). Hydrographic and current observations on the continental slope and shelf of the western equatorial atlantic. *Journal of physical oceanography*, *16*(8), 1412–1429.

Foltz, G. R. & McPhaden, M. J. (2004). The 30–70 day oscillations in the tropical Atlantic. *Geophysical research letters*, *31*(15).

Foltz, G. R. & McPhaden, M. J. (2009). Impact of barrier layer thickness on sst in the central tropical north atlantic. *Journal of Climate*, *22*(2), 285–299.

Fournier, S., Vandemark, D., Gaultier, L., Lee, T., Jonsson, B. & Gierach, M. M. (2017). Interannual Variation in Offshore Advection of Amazon-Orinoco Plume Waters: Observations, Forcing Mechanisms, and Impacts. *Journal of Geophysical Research: Oceans*, *122*(11), 8966–8982. doi:10.1002/2017JC013103

Geyer, W. R., Beardsley, R. C., Candela, J., Castro, B. M., Legeckis, R. V., Lentz, S. J., … Trowbridge, J. H. (1991). The physical oceanography of the amazon outflow. *Oceanography*, *4*(1), 8–14.

Gibbs, R. J. (1982). Currents on the shelf of north-eastern South America. *Estuarine, Coastal and Shelf Science*, *14*(3), 283–299.

Godfrey, J. S. & Lindstrom, E. J. (1989). The heat budget of the equatorial western pacific surface mixed layer. *Journal of Geophysical Research: Oceans*, *94*(C6), 8007–8017. doi:10.1029/JC094iC06p08007

Gray, W. M. (1968). GLOBAL VIEW OF THE ORIGIN OF TROPICAL DISTURBANCES AND STORMS. *Monthly Weather Review*, *96*(10), 669–700. doi:10.1175/1520-0493(1968)096<0669:GVOTOO>2.0.CO;2

Grodsky, S. A. [Semyon A.], Johnson, B. K., Carton, J. A. & Bryan, F. O. (2015). Interannual caribbean salinity in satellite data and model simulations. *Journal of Geophysical Research: Oceans*, *120*(2), 1375–1387. doi:10.1002/2014JC010625

Grodsky, S. A. [Semyon A.], Reul, N., Chapron, B., Carton, J. A. & Bryan, F. O. (2017). Interannual surface salinity on northwest atlantic shelf. *Journal of Geophysical Research: Oceans*, *122*(5), 3638–3659. doi:10.1002/2016JC012580

Grodsky, S. A. [Semyon A], Reul, N., Lagerloef, G., Reverdin, G., Carton, J. A., Chapron, B., … Kao, H.-Y. (2012). Haline hurricane wake in the amazon/orinoco plume: Aquarius/sacd and smos observations. *Geophysical Research Letters*, *39*(20).

Grodsky, S. A. [Semyon A], Reverdin, G., Carton, J. A. & Coles, V. J. (2014). Year-to-year salinity changes in the amazon plume: Contrasting 2011 and 2012 aquarius/sacd and smos satellite data. *Remote Sensing of Environment*, *140*, 14–22.

Hellerman, S. (1980). Charts of the variability of the wind stress over the tropical atlantic. In *Oceanography and surface layer meteorology in the b/c scale* (pp. 63–75). Elsevier.

Hernandez, O., Jouanno, J. & Durand, F. (2016). Do the amazon and orinoco freshwater plumes really matter for hurricane-induced ocean surface cooling? *Journal of Geophysical Research: Oceans*, *121*(4), 2119–2141.

Hoegh-Guldberg, O. & Salvat, B. (1995). Periodic mass-bleaching and elevated sea temperatures: Bleaching of outer reef slope communities in moorea, french polynesia. *Marine ecology progress series*, *121*, 181–190.

Hu, C., Montgomery, E. T., Schmitt, R. W. & Muller-Karger, F. E. (2004). The dispersal of the amazon and orinoco river water in the tropical atlantic and caribbean sea: Observation from space and s-palace floats. *Deep Sea Research Part II: Topical Studies in Oceanography*, *51*(10-11), 1151–1171.

SO-HYBAM. (2019). *discharge estimates of Ciudad Bolivar gauging station*. Retrieved June 5, 2020, from https://hybam.obs-mip.fr/

Johns, E. M., Lumpkin, R., Putman, N. F. [Nathan F], Smith, R. H., Muller-Karger, F. E., Rueda-Roa, D. T., … Gramer, L. J. et al. (2020). The establishment of a pelagic *Sargassum* pop-

ulation in the tropical Atlantic: Biological consequences of a basin-scale long distance dispersal event. *Progress in Oceanography*, *182*, 102269.

Kennedy, J., Dunn, R., McCarthy, M., Titchner, H. & Morice, C. (2017). Global and regional climate in 2016. *Weather*, *72*(8), 219–225.

Klotzbach, P. J. (2011). The influence of El Niño–Southern Oscillation and the Atlantic multidecadal oscillation on Caribbean tropical cyclone activity. *Journal of climate*, *24*(3), 721–731.

Knight, J. R., Folland, C. K. & Scaife, A. A. (2006). Climate impacts of the atlantic multidecadal oscillation. *Geophysical Research Letters*, *33*(17). doi:10.1029/2006GL026242

Lentz, S. J. (1995). Seasonal variations in the horizontal structure of the Amazon Plume inferred from historical hydrographic data. *Journal of Geophysical Research: Oceans*, *100*(C2), 2391–2400. doi:10.1029/94JC01847

Lentz, S. J. & Limeburner, R. (1995). The Amazon River Plume during AMASSEDS: Spatial characteristics and salinity variability. *Journal of Geophysical Research: Oceans*, *100*(C2), 2355–2375.

Liebmann, B., Vera, C. S., Carvalho, L. M., Camilloni, I. A., Hoerling, M. P., Allured, D., … Bidegain, M. (2004). An observed trend in central south american precipitation. *Journal of Climate*, *17*(22), 4357–4367.

Liu, G., Strong, A. E. & Skirving, W. (2003). Remote sensing of sea surface temperatures during 2002 barrier reef coral bleaching. *Eos, Transactions American Geophysical Union*, *84*(15), 137–141.

Lukas, R. & Lindstrom, E. (1991). The mixed layer of the western equatorial Pacific Ocean. *Journal of Geophysical Research: Oceans*, *96*(S01), 3343–3357. doi:10.1029/90JC01951. eprint: https://agupubs.onlinelibrary.wiley.com/doi/pdf/10.1029/90JC01951

Malmgren, B. A., Winter, A. & Chen, D. (1998). El nino–southern oscillation and north atlantic oscillation control of climate in puerto rico. *Journal of Climate*, *11*(10), 2713–2717.

Maloney, E. D. & Hartmann, D. L. (2000). Modulation of hurricane activity in the gulf of mexico by the madden-julian oscillation. *Science*, *287*(5460), 2002–2004.

Marengo, J. A. & Espinoza, J. (2016). Extreme seasonal droughts and floods in Amazonia: Causes, trends and impacts. *International Journal of Climatology*, *36*(3), 1033–1050.

Martin, E. R. & Schumacher, C. (2011). Modulation of caribbean precipitation by the madden–julian oscillation. *Journal of Climate*, *24*(3), 813–824.

Masson, S. & Delecluse, P. (2001). Influence of the Amazon River runoff on the tropical Atlantic. *Physics and Chemistry of the Earth, Part B: Hydrology, Oceans and Atmosphere*, *26*(2), 137–142. doi:https://doi.org/10.1016/S1464-1909(00)00230-6

McWilliams, J. P., Côté, I. M., Gill, J. A., Sutherland, W. J. & Watkinson, A. R. (2005). Accelerating impacts of temperature-induced coral bleaching in the caribbean. *Ecology*, *86*(8), 2055–2060.

Molleri, G. S., Novo, E. M. d. M. & Kampel, M. (2010). Space-time variability of the amazon river plume based on satellite ocean color. *Continental Shelf Research*, *30*(3-4), 342–352.

Muller-Karger, F. E., McClain, C. R. & Richardson, P. L. (1988). The dispersal of the Amazon's water. *Nature*, *333*(6168), 56. doi:10.1038/333056a0

Mumby, P. J., Chisholm, J. R., Clark, C. D., Hedley, J. D. & Jaubert, J. (2001). A bird's-eye view of the health of coral reefs. *Nature*, *413*(6851), 36–36.

Murtugudde, R. G., Ballabrera-Poy, J., Beauchamp, J. & Busalacchi, A. J. (2001). Relationship between zonal and meridional modes in the tropical atlantic. *Geophysical Research Letters*, *28*(23), 4463–4466. doi:10.1029/2001GL013407

Muthiga, N. A. & Szmant, A. M. (1987). The effects of salinity stress on the rates of aerobic respiration and photosynthesis in the hermatypic coral siderastrea siderea. *The Biological Bulletin*, *173*(3), 539–551.

Newinger, C. & Toumi, R. (2015). Potential impact of the colored Amazon and Orinoco plume on tropical cyclone intensity. *Journal of Geophysical Research: Oceans*, *120*(2), 1296–1317.

Nikiema, O., Devenon, J.-L. & Baklouti, M. (2007). Numerical modeling of the amazon river plume. *Continental Shelf Research*, *27*(7), 873–899.

NOAA Coral Reef Watch. (2018). NOAA Coral Reef Watch Version 3.1 Daily Global 5-km Satellite Coral Bleaching Degree Heating Week Product. Updated daily. College Park, Maryland, USA.

NOAA Coral Reef Watch. (2019). Global coral bleaching 2014-2017: Status and an appeal for observations. Retrieved from https://coralreefwatch.noaa.gov/satellite/analyses_guidance/global_coral_bleaching_2014-17_status.php

NOAA National Weather Services. (2016). ENSO effects across the northeastern Caribbean. Retrieved May 7, 2019, from https://www.weather.gov/sju/climo_enso

NOAA Physical Sciences Laboratory. (2019). Multivariate enso index version 2 (mei.v2). Retrieved August 2, 2019, from https://www.esrl.noaa.gov/psd/enso/mei/

Paegle, J. N., Byerle, L. A. & Mo, K. C. (2000). Intraseasonal modulation of south american summer precipitation. *Monthly Weather Review*, *128*(3), 837–850.

Pailler, K., Bourlès, B. & Gouriou, Y. (1999). The barrier layer in the western tropical atlantic ocean. *Geophysical Research Letters*, *26*(14), 2069–2072.

Porter, J. W., Fitt, W. K., Spero, H. J., Rogers, C. S. & White, M. W. (1989). Bleaching in reef corals: Physiological and stable isotopic responses. *Proceedings of the National Academy of Sciences*, *86*(23), 9342–9346.

Putman, N. F. [Nathan F.], Goni, G. J., Gramer, L. J., Hu, C., Johns, E. M., Trinanes, J. & Wang, M. (2018). Simulating transport pathways of pelagic *Sargassum* from the Equatorial Atlantic into the Caribbean Sea. *Progress in Oceanography*, *165*, 205–214. doi:https://doi.org/10.1016/j.pocean.2018.06.009

Richardson, P. L. & McKee, T. K. (1984). Average seasonal variation of the atlantic equatorial currents from historical ship drifts. *Journal of Physical Oceanography*, *14*(7), 1226–1238.

Roquet, F., Madec, G., McDougall, T. & Barker, P. (2015). Accurate polynomial expressions for the density and specific volume of seawater using the teos-10 standard. *Ocean Modelling*. doi:10.1016/j.ocemod.2015.04.002

Scott, D. W. (2015). *Multivariate Density Estimation: Theory, Practice, and Visualization*. John Wiley & Sons.

Skirving, W., Strong, A. E., Liu, G., Arzayus, F., Liu, C. & Sapper, J. (2006). Extreme events and perturbations of coastal ecosystems. In L. L. Richardson & E. F. LeDrew (Eds.), *Remote sensing of aquatic coastal ecosystem processes* (Chap. 2, Vol. 9, pp. 11–25). Springer.

Smith, S. V. & Buddemeier, R. (1992). Global change and coral reef ecosystems. *Annual Review of Ecology and Systematics*, *23*(1), 89–118.

Wang, M. & Hu, C. (2017). Predicting *Sargassum* blooms in the Caribbean Sea from MODIS observations. *Geophysical Research Letters*, *44*(7), 3265–3273.

Wellington, G. M., Glynn, P. W., Strong, A. E., Navarrete, S. A., Wieters, E. & Hubbard, D. (2001). Crisis on coral reefs linked to climate change. *Eos, Transactions American Geophysical Union*, *82*(1), 1–5.

Wheeler, M. C. & Hendon, H. H. (2004). An all-season real-time multivariate mjo index: Development of an index for monitoring and prediction. *Monthly weather review*, *132*(8), 1917–1932.

Wilkinson, C. & Souter, D. (2008). *Status of Caribbean coral reefs after bleaching and hurricanes in 2005*. Global Coral Reef Monitoring Network, Reef and Rainforest Research Centre. Townsville.

Wiseman Jr, W. J., Rabalais, N. N., Dagg, M. J. & Whitledge, T. E. (1999). (Chap. Nutrient enhanced coastal ocean productivity in the northern Gulf of Mexico: understanding the effects of nutrients on a coastal ecosystem). NOAA Coastal Ocean Program decision analysis series; no. 14. Professional Paper. U.S. Dept. of Commerce, National Oceanic. Retrieved from https://repository.library.noaa.gov/view/noaa/1698

Zeng, N., Yoon, J.-H., Marengo, J. A., Subramaniam, A., Nobre, C. A., Mariotti, A. & Neelin, J. D. (2008). Causes and impacts of the 2005 Amazon drought. *Environmental Research Letters*, *3*(1), 014002. doi:10.1088/1748-9326/3/1/014002

Zhang, C. (2005). Madden-Julian Oscillation. *Reviews of Geophysics*, *43*(2).

Glossary

El Niño phenomenon associated with anomalously warm waters in the central and eastern Pacific near the Equator

HotSpot HotSpot values are sea-surface temperature (SST) deviations from the Maximum Monthly Mean (MMM). Values greater than 1 suggest SSTs that can cause bleaching in corals.

La Niña phenomenon associated with anomalously cool waters in the central and eastern Pacific near the Equator

List of abbreviations and acronyms

djf December–January–February
jja June–July–August
mam March–April–May
son September–October–November

AMO Atlantic Multidecadal Oscillation

BL barrier layer
BLT barrier layer thickness

CDOM colored dissolved organic matter
CMEMS Copernicus Marine Environment Monitoring Service

DHW degree heating week
DOM dissolved organic matter

ECMWF European Centre for Medium-Range Weather Forecasts
ENSO El Niño-Southern Oscillation
EOF Empirical Orthogonal Function

GLORYS12V1 Global Ocean Physical Reanalysis Product

ILD isothermal layer depth
ITCZ Intertropical Convergence Zone

KDE kernel density estimate

MEI Multivariate ENSO Index
MJO Madden-Julian Oscillation
ML mixed layer
MLD mixed layer depth
MMM Maximum Monthly Mean

NBC North Brazil Current
NCAR National Center for Atmospheric Research
NECC North Equatorial Counter Current
NOAA CRW NOAA Coral Reef Watch

OHC oceanic heat content

PC Principal Component
pdf probability density function

RMM series Real-time Multivariate MJO series
RMSD root mean square difference

SLP sea level pressure
SMOS Soil Moisture and Ocean Salinity
SSHR sea-surface heating rate
SSS sea-surface salinity
SST sea-surface temperature

TC Tropical Cyclone
TEOS-10 Thermodynamic Equation Of Seawater - 2010
TPA total precipitation anomaly

WTNA Western Tropical North Atlantic

A

Comparison of GLORYS and NOAA-CRW HotSpot and DHW

To verify whether the Global Ocean Physical Reanalysis Product (GLORYS12V1) dataset is suitable for predicting coral bleaching events, the data is compared with NOAA Coral Reef Watch (NOAA CRW) data. In order to do so, the NOAA CRW HotSpot and degree heating week (DHW) products are calculated from the GLORYS12V1 data and compared to those data given by NOAA CRW

The NOAA data were obtained from https://coralreefwatch.noaa.gov/satellite/bleaching5km/. As this data is on a 5 km grid, it was regridded to match the GLORYS12V1 grid and subsequently visualised using the same colour map.

The GLORYS12V1 sea-surface temperatures (SSTs) were used to calculate the DHW product according to the methodology described on https://coralreefwatch.noaa.gov/satellite/methodology/methodology.php. NOAA uses the 1985-2012 climatology to calculate their anomalies, which is regridded and used here as well.

As a first step, NOAA's Maximum Monthly Mean (MMM) SST is subtracted from the GLORYS12V1 SST to obtain HotSpot values, see Eq. (A.1).

$$\mathrm{HotSpot}_{x,y,t} = \mathrm{SST}_{x,y,t} - \mathrm{MMM}_{x,y,t} \tag{A.1}$$

The next step is to calculate DHW values from these HotSpot values for each grid cell. DHWs are defined as the cumulative HotSpots of the last 12 weeks (84 days) for HotSpot values greater than 1.

$$\mathrm{DHW}_{x,y,t} = \sum_{i=t-84}^{t} \mathrm{HotSpot}_{x,y,t} \quad \text{for } \mathrm{HotSpot}_{x,y,t} > 1 \tag{A.2}$$

Since the HotSpots are daily values, the resulting value is divided by 7 in order to obtain the unit °C × week.

As an example of what these data look like, the following results are generated for 12 October of three bleaching years 1998, 2005 and 2010.

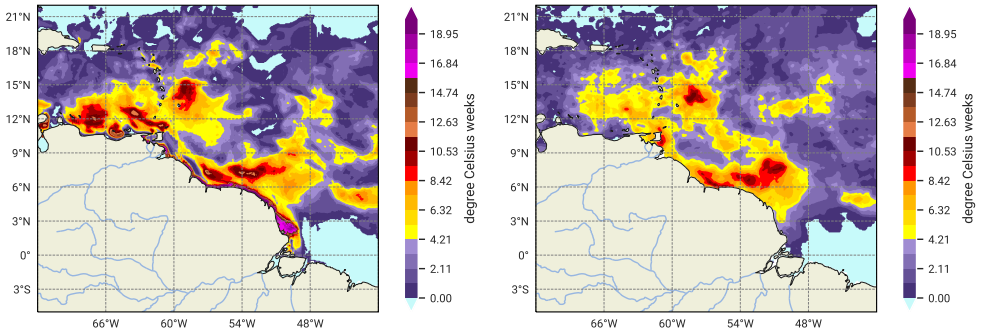

(a) (b)

Figure A.1: Comparison of DHW pattern on 12 October 1998 (a) calculated from GLORYS12V1 data and (b) presented using data retrieved from (NOAA Coral Reef Watch, 2018).

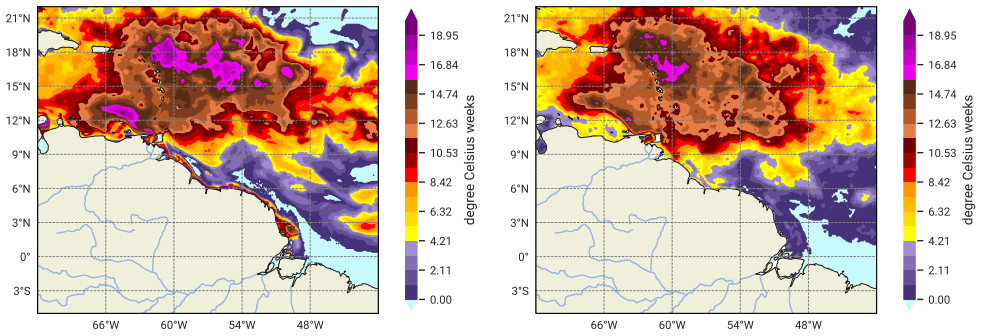

(a) (b)

Figure A.2: Comparison of DHW pattern on 12 October 2005 (a) calculated from GLORYS12V1 data and (b) presented using data retrieved from (NOAA Coral Reef Watch, 2018).

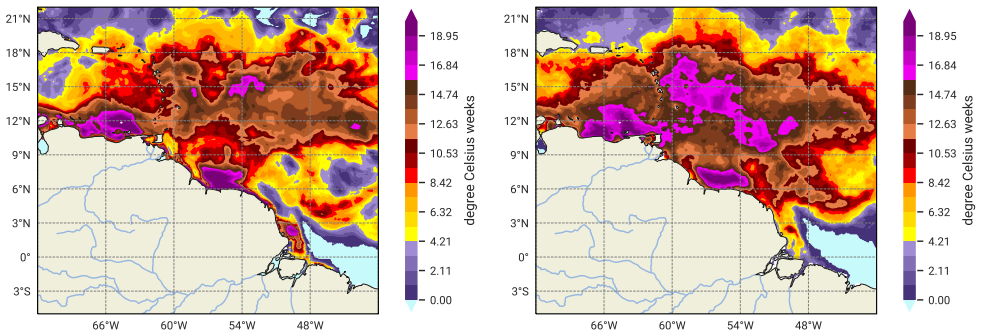

(a) (b)

Figure A.3: Comparison of DHW pattern on 12 October 2010 (a) calculated from GLORYS12V1 data and (b) presented using data retrieved from (NOAA Coral Reef Watch, 2018).

B

Sea surface heating rate

The sea-surface heating rate (SSHR) is approximated using daily sea-surface temperature (SST) in the surface layer (0.49 m depth) of the Global Ocean Physical Reanalysis Product (GLORYS12V1) model. These daily values are first low-passed filtered using a rolling mean with a 7-day window. Hereafter, the differential is calculated using forward differences:

$$\mathrm{SSHR}_i = \frac{\mathrm{SST}_{i+1} - \mathrm{SST}_i}{t_{i+1} - t_i} \tag{B.1}$$

A high SSHR is expected when the river plume is present, resulting in negative correlation coefficients with sea-surface salinity (SSS) anomalies. However, this is only valid when the SST in plume- and open-ocean waters is similar. When SST in the river plume is much higher than open-ocean SST, it loses more heat to the atmosphere and is expected to cool down faster.

In Fig. B.1a, which shows correlations between SSS and SSHR anomalies in June–July–August (*jja*), sparse regions of significant negative correlations are observed near the Amazon river mouth. However, regions of positive correlation are also seen further away from the river mouth. Additionally, no significant correlations are found in September–October–November (*son*).

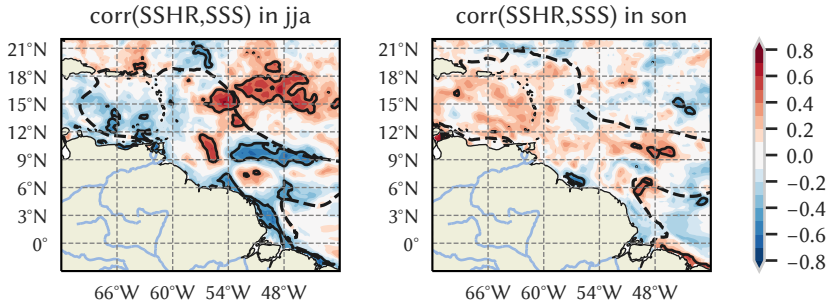

Figure B.1: Correlation between SSHR and SSS anomalies for the *jja* and *son* seasons. The black solid contour gives the 95 % significance level. The black dashed contour gives the mean SSS = 35.4 psu in the respective seasons.

Using the sample region shown in Fig. 4.2, a kernel density estimate (KDE) is constructed of the average daily SSHR in the river plume compared to that in open-ocean waters. Since the SST was found to be on average 0.93 °C higher in the river plume than in open-ocean waters in this region, it is expected that the SSHR is lower in the plume than in the surrounding waters in this region.

The upper right (lower left) quadrant in Fig. B.2 represents the region in which an overall temperature increase (decrease) is found in the area. When a point is found in the green

(yellow) shaded area, the temperature change in the low-salinity waters is more (less) extreme than the temperature change in the high-salinity waters on a given day.

On days when there is a temperature increase in the area (upper right quadrant in Fig. B.2), the probability that plume waters heat up faster than the open-ocean waters is 46.9 %. When there is an overall decrease in water temperature in the area (lower left quadrant in Fig. B.2), the probability that plume waters cool down faster than the open-ocean waters is 54.1 %. In other words, the plume waters heat up more slowly and cool down faster in these months.

Results:

- in general, the heating rate of plume waters is lower than that of open-ocean waters: $dT_{\text{plume}} - dT_{\text{open-ocean}} = -0.0026\ ^{\circ}\text{C/d}$ ($p < 0.001$)
- on a day where overall *heating* takes place, plume waters warm up *slower* than open-ocean waters: $dT_{\text{plume}} - dT_{\text{open-ocean}} = -0.0017$ ($p < 0.001$)
- on a day where overall *cooling* takes place, plume waters cool down *faster* than open-ocean waters: $dT_{\text{plume}} - dT_{\text{open-ocean}} = -0.0020$ ($p < 0.05$)

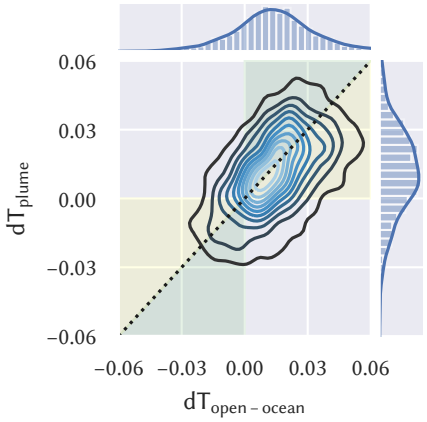

Figure B.2: KDE of daily $dSST/dt$ from July to September in plume- and open-ocean waters, given in °C/d. Spatial range is from 14N to 16N, and 70W to 42W. The dotted line shows the line of equality.

C

EOFs and corresponding PCs

Computed leading Empirical Orthogonal Functions (EOFs) and corresponding Principal Components (PCs) are presented here. Data sets are first detrended and anomalies from the seasonality are computed for each grid cell.

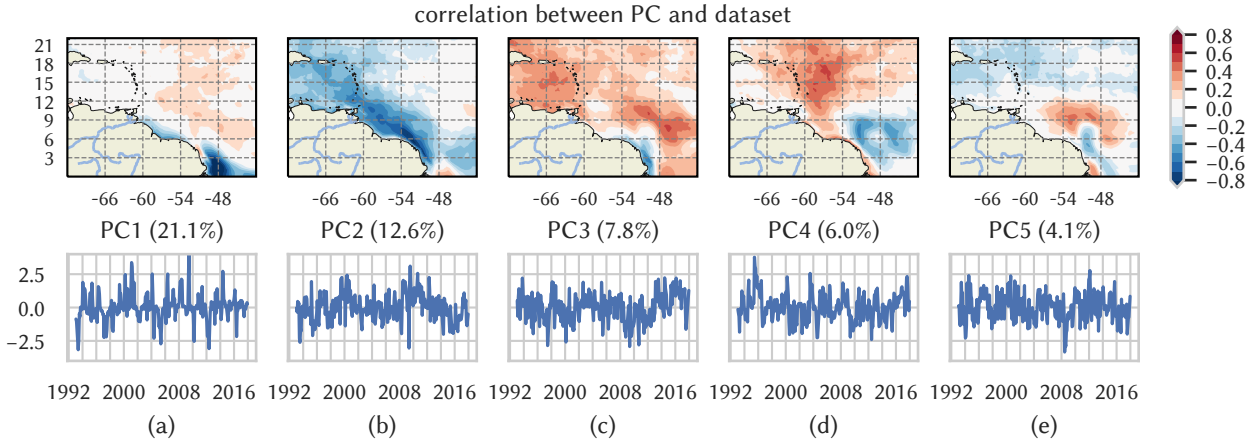

Figure C.1: Leading 5 EOFs of sea-surface salinity (SSS) (top row) with corresponding PCs time series, scaled to unit variance (bottom row). The percentage of explained variance of each mode is given in parentheses.

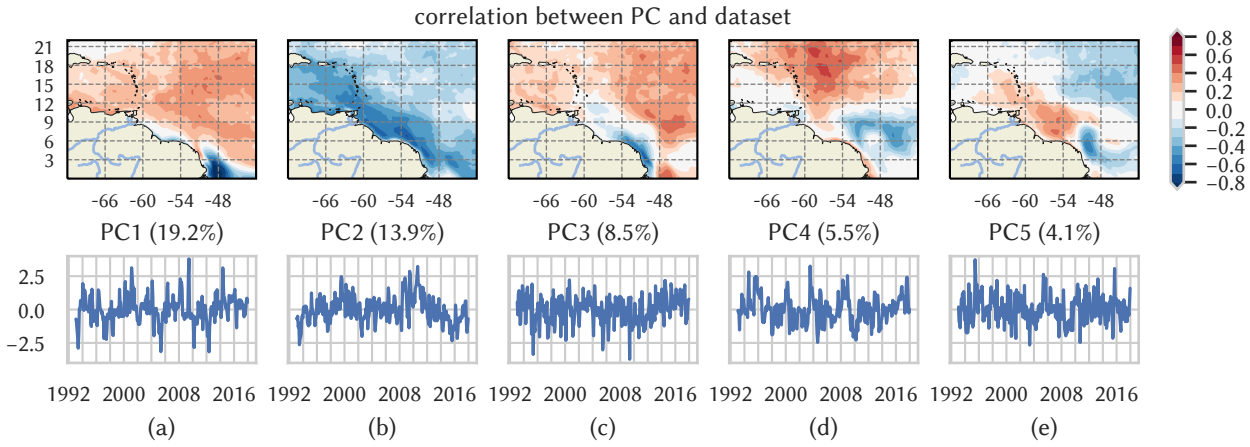

Figure C.2: Same as Fig. C.1, but for density.

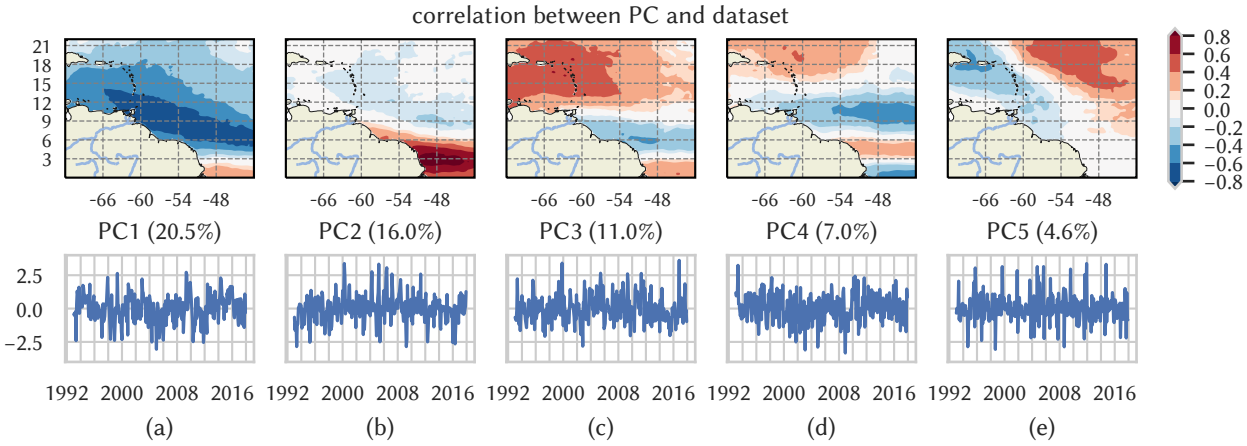

Figure C.3: Same as Fig. C.1, but for total precipitation.

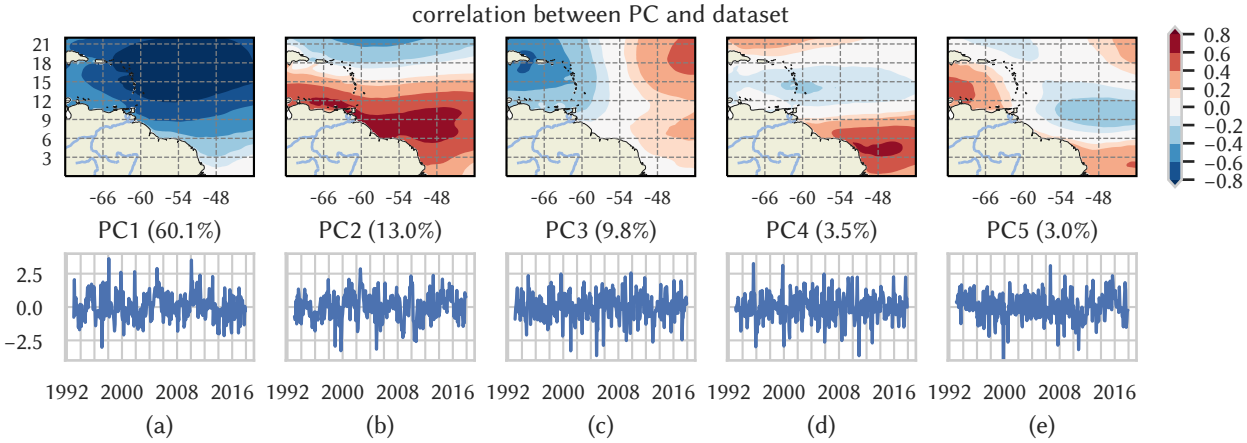

Figure C.4: Same as Fig. C.1, but for wind speed.

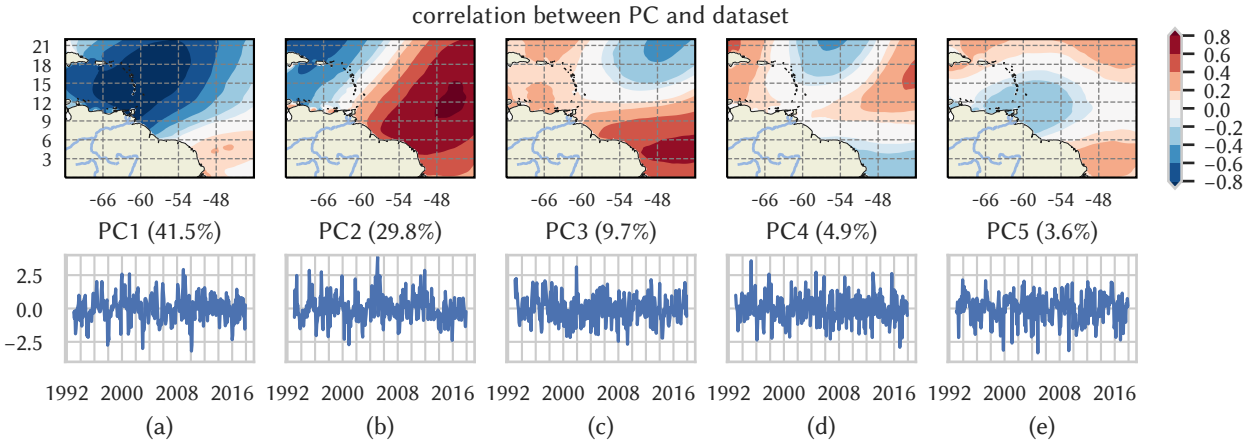

Figure C.5: Same as Fig. C.1, but for meridional (N-S) wind speed.

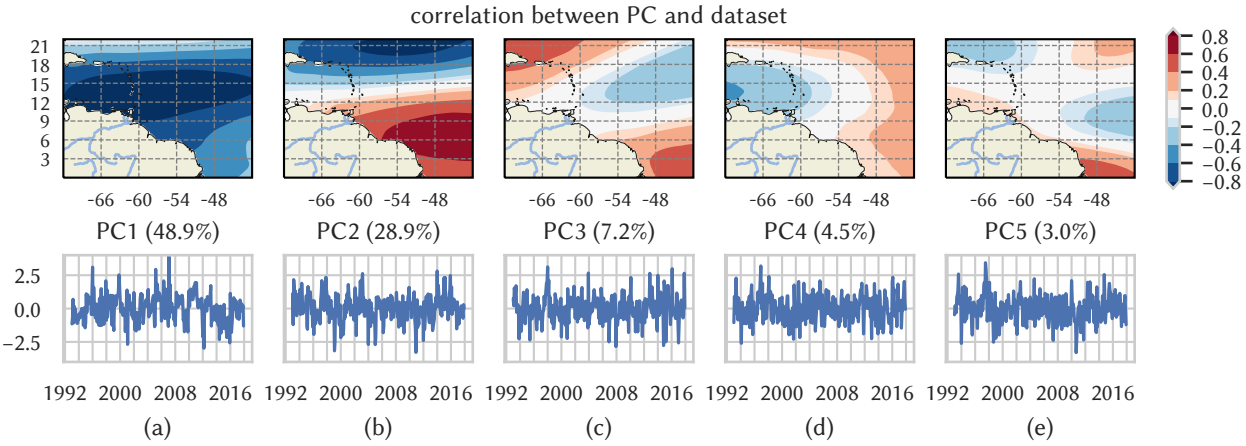

Figure C.6: Same as Fig. C.1, but for vertical wind shear.

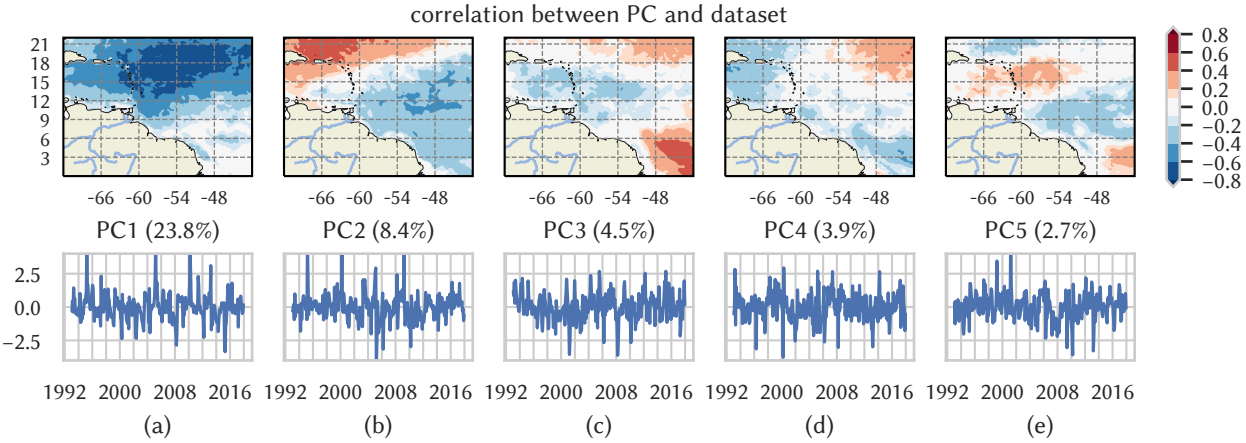

Figure C.7: Same as Fig. C.1, but for isothermal layer depth (ILD).

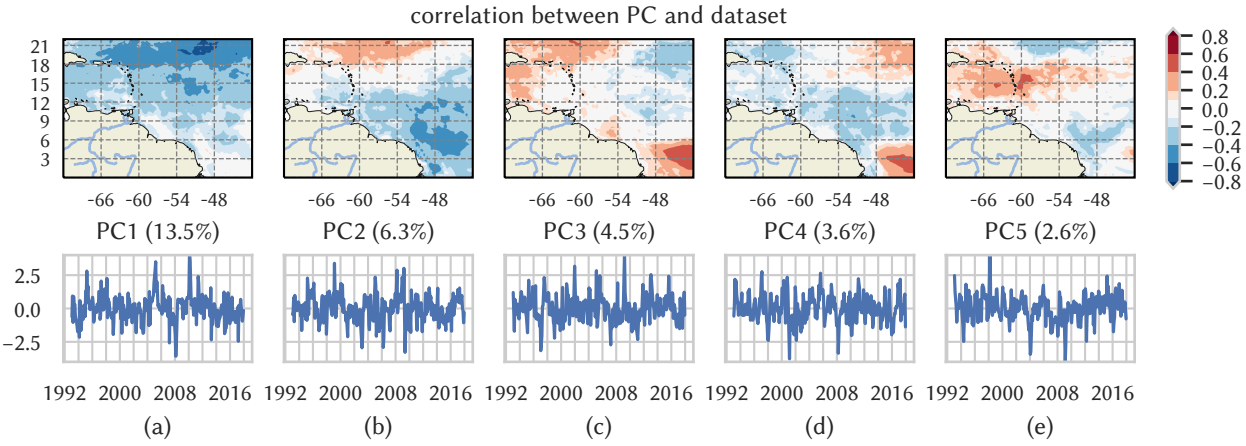

Figure C.8: Same as Fig. C.1, but for mixed layer depth (MLD),

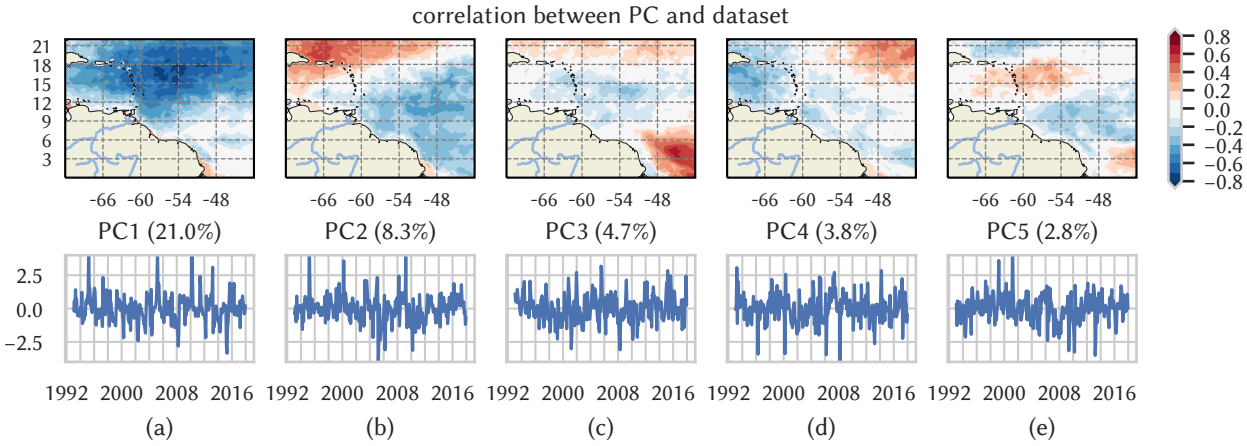

Figure C.9: Same as Fig. C.1, but for oceanic heat content (OHC)

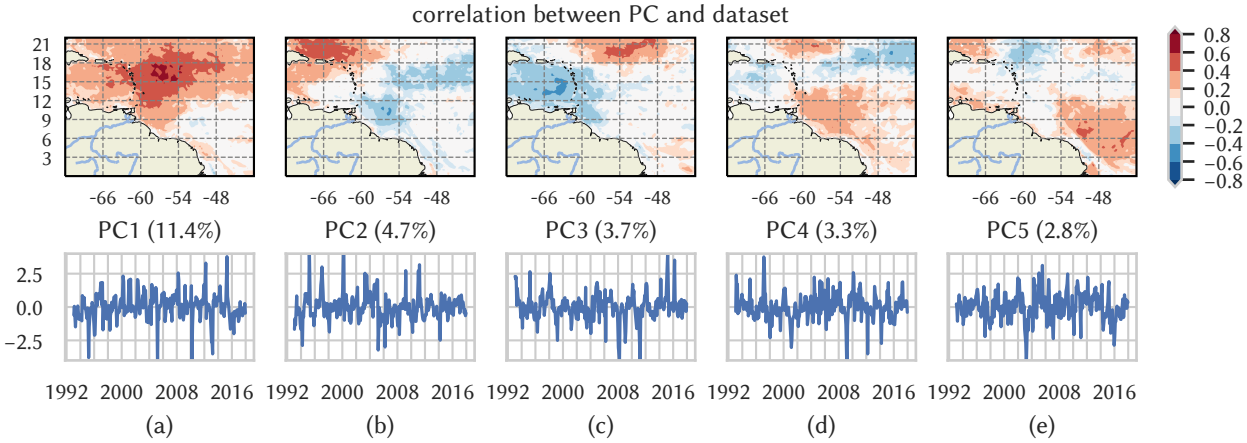

Figure C.10: Same as Fig. C.1, but for barrier layer thickness (BLT)

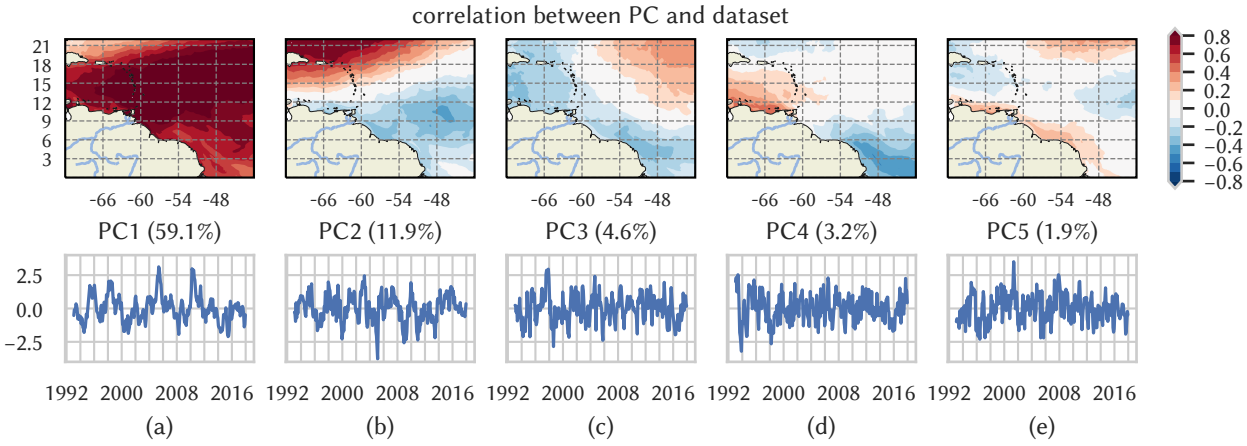

Figure C.11: Same as Fig. C.1, but for sea-surface temperature (SST).

D

Composition by phase of the Madden-Julian Oscillation

Here, results of Madden-Julian Oscillation (MJO) composition of sea-surface salinity (SSS), sea-surface temperature (SST) and sea-surface heating rate (SSHR) are presented. Daily anomalies from the seasonality are composited by phase of the MJO, after which the mean anomaly from the seasonal cycle is calculated. Significance is determined using a two-tailed t-test. For more information on MJO composition, see Section 6.1.4. For more information on the MJO, see Section 2.2.6.

– figures shown on following page –

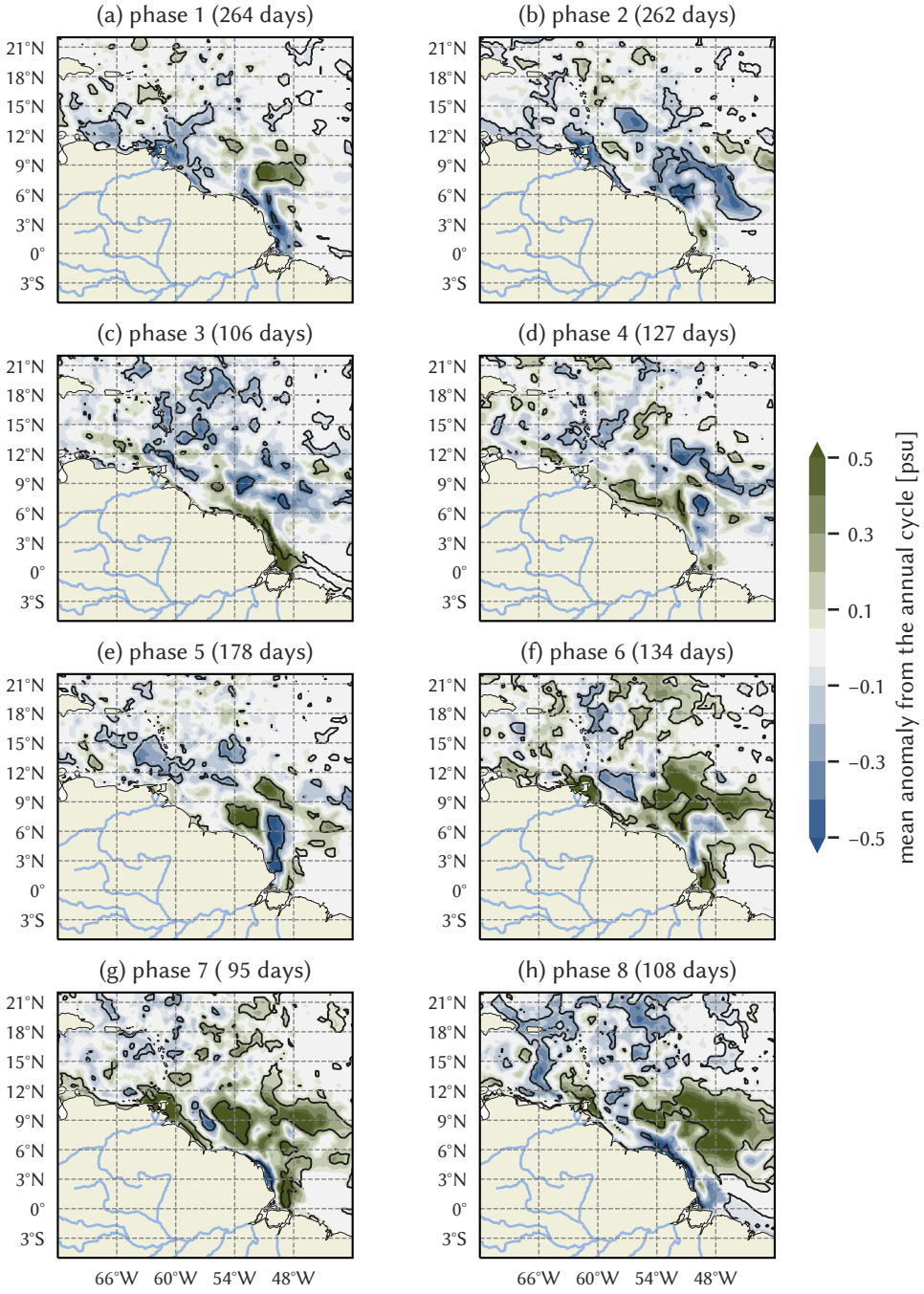

Figure D.1: Mean of daily SSS anomalies from the annual cycle in July–September, aggregated by phases of the MJO using only strong MJO events (RMM amplitude >1). The black contours show 99 % significance, based on the local standard deviation determined using a two-tailed t-test. The number of days on which a strong MJO event in the respective phases was present is given in parentheses.

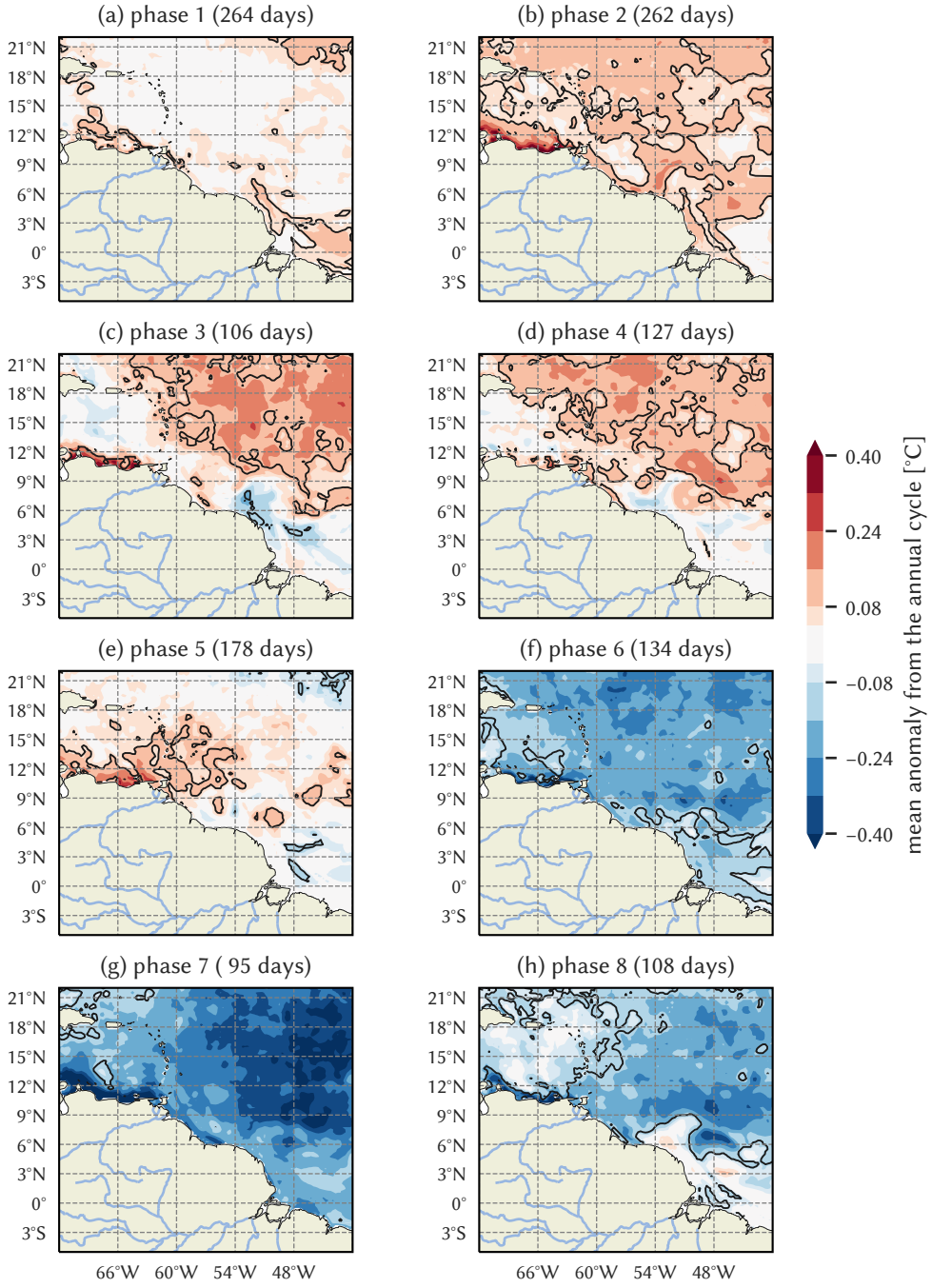

Figure D.2: Mean of daily SST anomalies from the annual cycle in July–September, aggregated by phases of the MJO using only strong MJO events (RMM amplitude >1). The black contours show 99 % significance, based on the local standard deviation determined using a two-tailed t-test. The number of days on which a strong MJO event in the respective phases was present is given in parentheses.

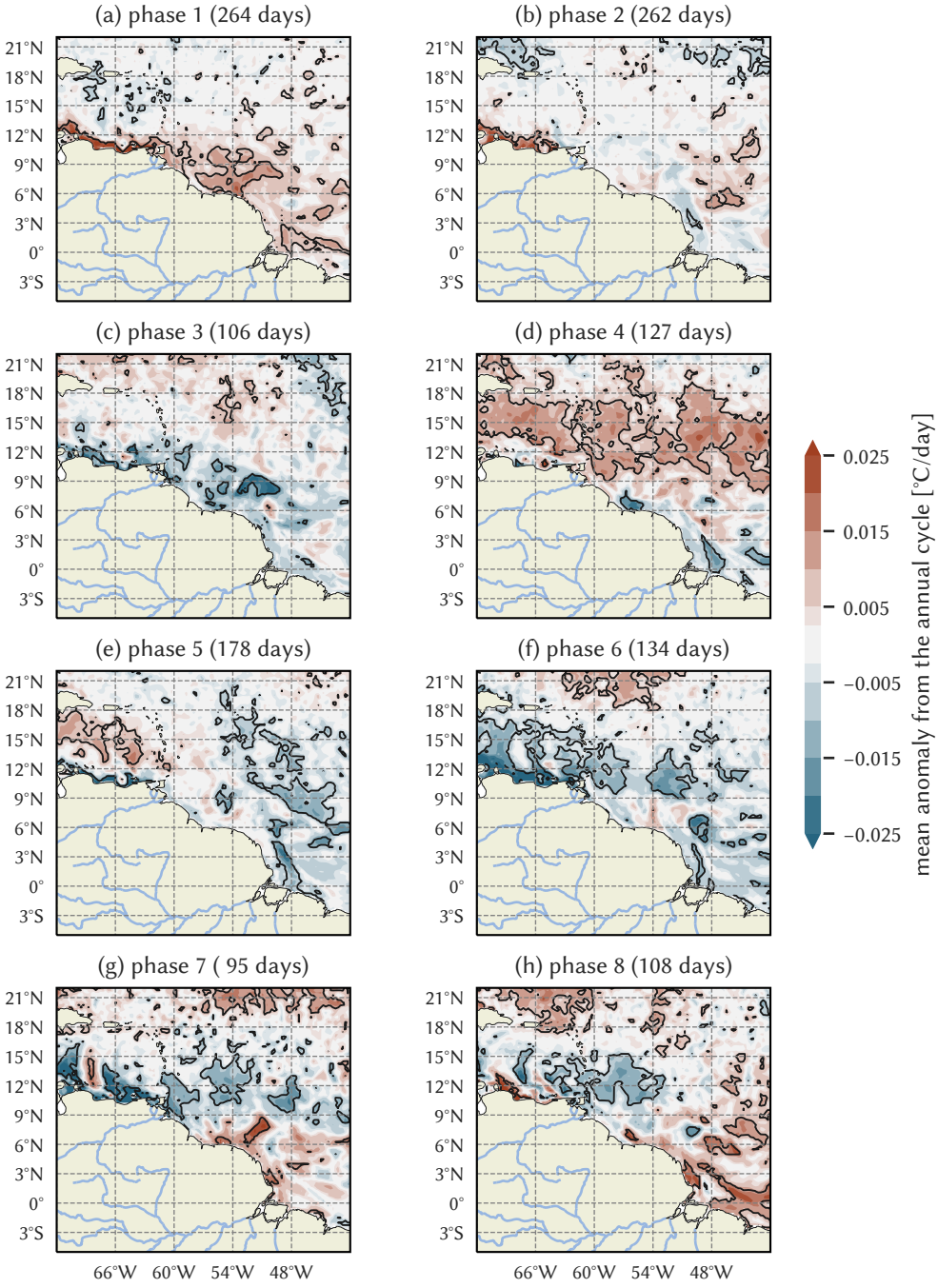

Figure D.3: Mean of daily SSHR anomalies from the annual cycle in July–September, aggregated by phases of the MJO using only strong MJO events (RMM amplitude >1). The black contours show 99 % significance, based on the local standard deviation determined using a two-tailed t-test. The number of days on which a strong MJO event in the respective phases was present is given in parentheses.

E

Reconstructed fields of SSS

To determine the descriptive quality of PC2, 3 and 4 of sea-surface salinity (SSS) (see Section 5.2.3) with respect to the interannual variability of the river plume, fields are reconstructed using these three Principal Components (PCs) only and compared to the original data set. For illustrative purposes, only September SSS fields are shown. Since the PCs are computed using SSS anomalies from the 1993–2018 seasonality, the reconstructed fields are added to the 1993–2018 September mean SSS at each grid point. Reconstruction and original SSS fields on the same date are shown side-by-side.

– figures begin on following page –

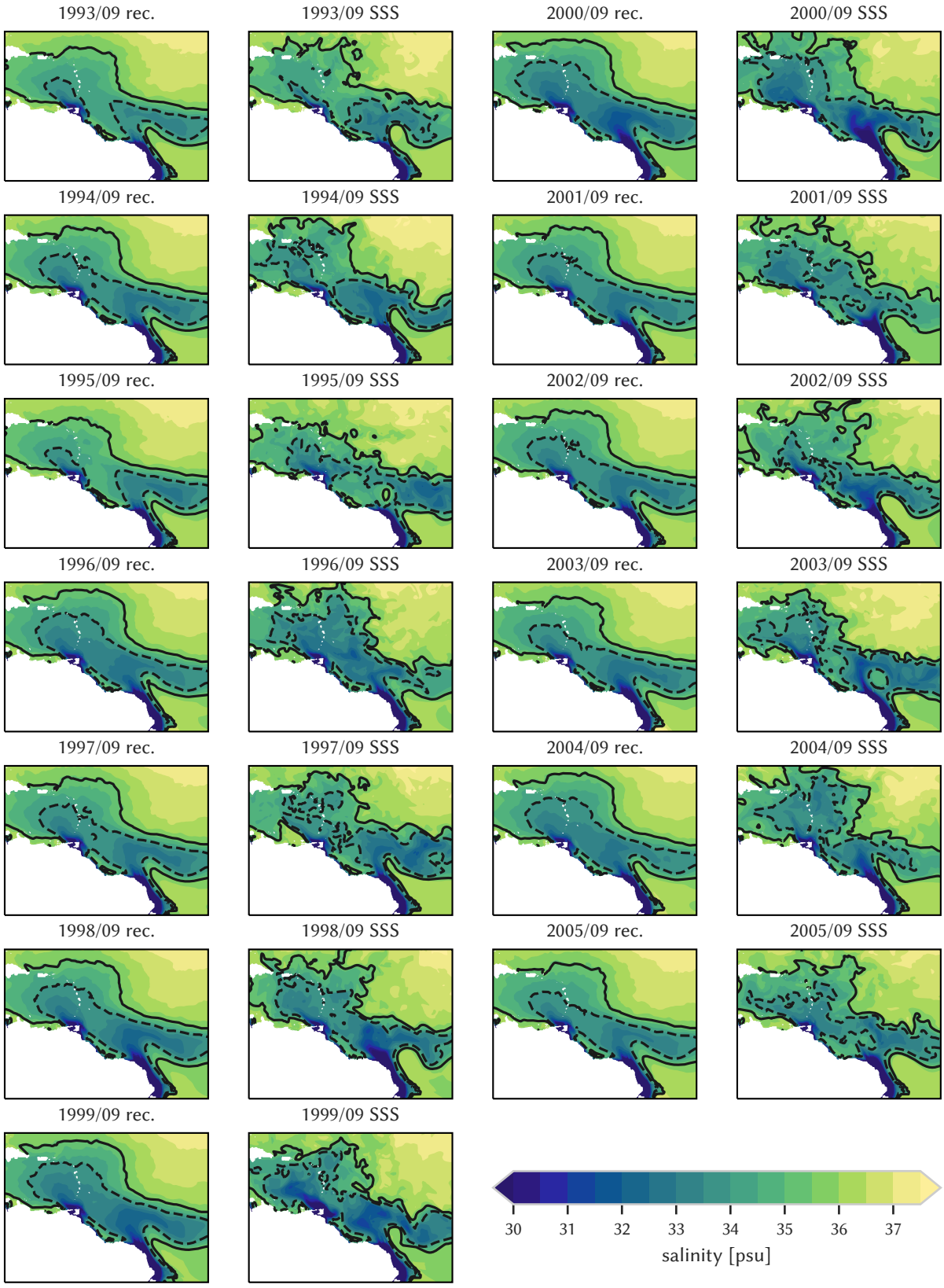

Figure E.1: Reconstructed fields ('rec.') of September SSS of each year in the 1993–2005 range (first and third column), compared to the original values in the data set ('SSS') (second and fourth column).

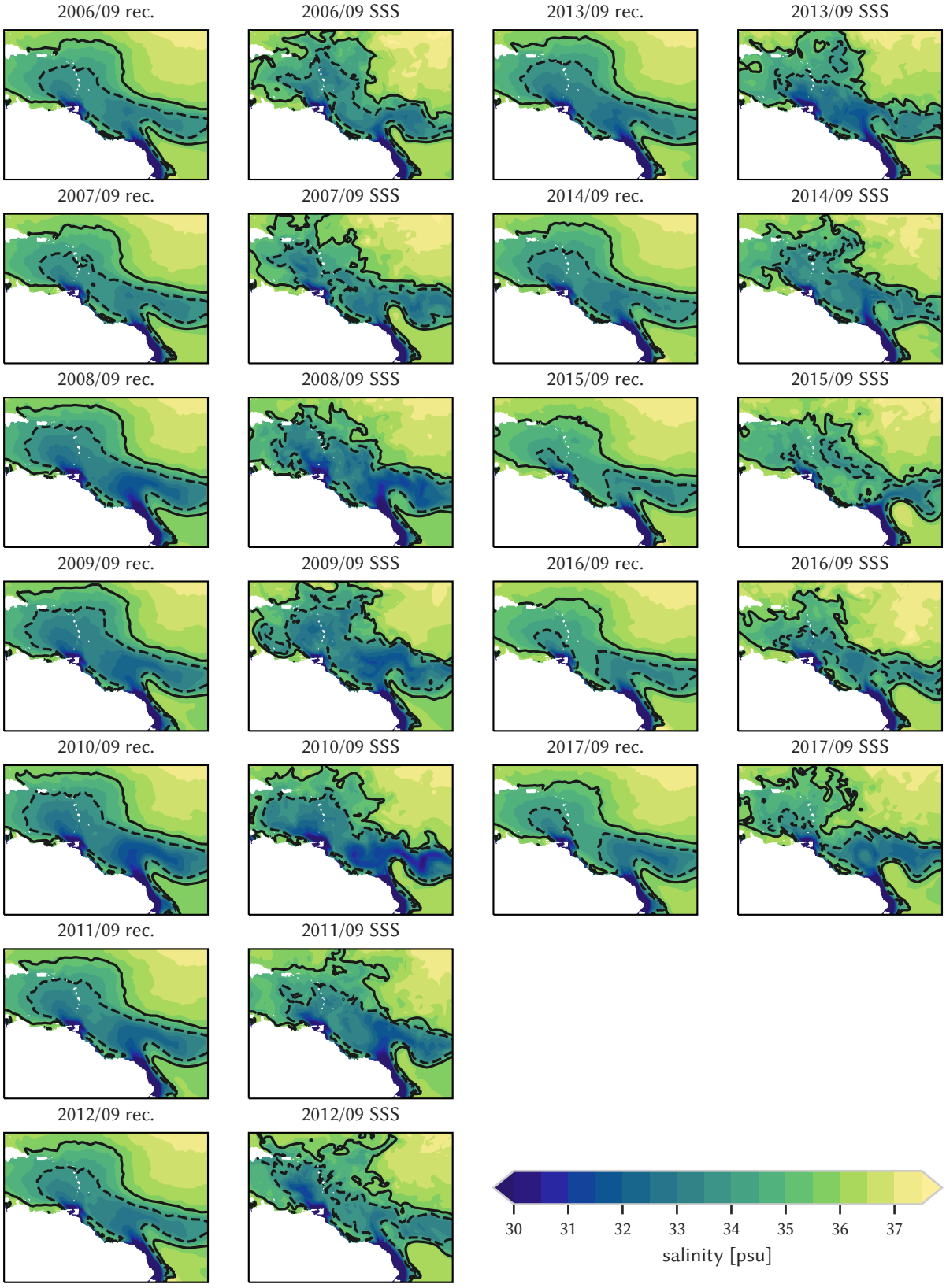

Figure E.2: Reconstructed fields of September SSS of each year in the 2006–2017 range (first and third column), compared to the original values in the data set (second and fourth column).